ASSESSMENT OF TAPERED PLASTIC FIBER SENSORS IN THE APPLICATIONS OF STRUCTURAL HEALTH MONITORING

LUO DONG

THESIS SUBMITTED IN FULFILMENT OF THE REQUIREMENTS FOR THE DEGREE OF DOCTOR OF PHILOSOPHY OF ENGINEERING

FACULTY OF ENGINEERING
UNIVERSITY OF MALAYA
KUALA LUMPUR

2013

ABSTRACT

In this thesis, the performances of tapered plastic fiber sensors (TPFSs) were assessed in the application of structural health monitoring—e.g., the monitoring of the early-age hydration process of cement pastes and the detection of vibration and crack in a concrete beam. A mathematical model based on ray-tracing theory was constructed to optimize the geometries of the proposed TPFSs, theoretically. Numerical simulation on the TPFS was carried out, as well as the effects of the geometries, including taper ratio, taper length, and launch angle of the initial ray. The surrounding temperature on the performance of the proposed sensor was also studied numerically. Two sets of sensor configurations were carried out to study the performances of TPFSs, which included different stripped lengths and different diameters. Theoretical and experimental results agreed with each other, and it was found that higher temperature sensitivity of the TPFS can be achieved by combining a longer taper length and lower taper ratio.

In the monitoring of the early-age hydration process of cement paste, the TPFSs were used to study the host specimen with different sizes—various cement/water ratios, as well as different ambient temperatures. The sensor characteristics were determined and calibrated by an embedded thermocouple. From the experimental results, the curing temperature and setting time were determined by monitoring the curing temperature as the curing progressed. The curing temperature rose with increasing mould size, decreasing w/c ratio, and increasing ambient temperature. The setting time could be shortened by a smaller specimen size, lower w/c ratio, and higher ambient temperature.

The TPFSs also showed the ability for vibration and crack detection in a concrete beam (CB). The natural frequencies' shift can be precisely determined by TPFSs and accelerometers, which indicate that the CB is damaged. The experimental results also demonstrated that the small diameter of the TPFS achieves a good sensitivity for vibration detection. The experiments for crack detection study were employed in small-scale CBs and full-scale reinforced CBs. The results showed that the TPFSs are capable of detecting the axial strain and the crack initiation in scale-model CBs, as well as the deflection and crack on full-scale reinforced CBs. These findings demonstrated that TPFSs are an ideal solution for the application of structural health monitoring in civil engineering.

ABSTRAK

Dalam tesis ini, persembahan Pergesan Gentian Plastik Tirus (TPFSs) telah dinilai dalam aplikasi pemantauan kesihatan struktur, contohnya pemantauan di awal penghidratan proses lepa simen dan mengesan getaran dan retak dalam rasuk konkrit. Satu model matematik yang berdasarkan teori-ray tracing telah dibina untuk mengoptimumkan geometri daripada TPFSs yang dicadangkan, secara teorinya. Simulasi berangka pada TPFS telah dijalankan dan kesan geometri termasuk nisbah tirus, panjang tirus, sudut sinar awal, dan suhu sekitar pada prestasi sensor yang dicadangkan telah dikaji secara berangka. Dua set konfigurasi sensor telah dijalankan untuk mengkaji prestasi TPFSs, yang termasuk panjang yang berbeza dilucutkan dan diameter yang berbeza. Keputusan teori dan eksperimen bersetuju dengan satu sama lain dan ia telah mendapati bahawa sensitiviti suhu yang lebih tinggi daripada TPFS boleh dicapai dengan menggabungkan penambahan panjang tirus dan nisbah tirus yang rendah.

Dalam pemantauan awal proses penghidratan simen tampal, TPFSs digunakan untuk mengkaji spesimen dengan saiz yang berbeza, pelbagai nisbah simen / air, serta berbeza suhu ambien. Ciri-ciri sensor telah ditentukan dan ditentukur oleh termogandingan terbenam. Daripada keputusan ujikaji, masa pengawetan suhu dan persekitaran telah ditentukan dengan memantau suhu pengawetan seperti kemajuan pengawetan. Suhu pengawetan meningkat dengan saiz acuan yang semakin meningkat, pengurangan

nisbah w/c, dan meningkatkan suhu ambien. Masa tetapan boleh dipendekkan oleh saiz spesimen yang lebih kecil, lebih rendah Nisbah w/c, dan suhu ambien yang lebih tinggi.

The TPFSs juga menunjukkan keupayaannya untuk pengesanan getaran dan retak dalam Rasuk Konkrit (CB). Anjakan frekuensi tabii boleh ditentukan lebih tepat oleh TPFSs dan pecutan, yang menunjukkan CB rosak. Keputusan eksperimen juga menunjukkan bahawa diameter TPFS yang kecil mencapai sensitiviti yang baik untuk mengesan getaran. Eksperimen untuk kajian pengesanan retak telah dijalankan untuk CBs ber skala kecil dan CBs ber skala penuh bertetulang. Keputusan menunjukkan bahawa TPFSs mampu untuk mengesan terikan paksi dan permulaan retak dalam skala model CBs dan pesongan dan retak pada skala penuh bertetulang CB. Penemuan ini menunjukkan bahawa TPFSs adalah cara yang sesuai untuk aplikasi pemantauan kesihatan struktur dalam kejuruteraan awam.

ACKNOWLEDGEMENTS

The successful completion of this postgraduate study would not have been possible without the help of several individuals and organizations. Especially, I am thankful to my supervisor, Dr. Zainah Ibrahim**,** for her advice, encouragement, and support while I pursued this research, and my co-supervisor, Assoc. Prof. Dr. Zubaidah Ismail, who provided me much of my initial motivation for pursuing this investigation and provided invaluable feedback, which has improved this work in nearly every respect.

Furthermore, the author would like to thank the staff of the Civil Engineering Department and the Concrete Laboratory for their help in this work.

My full-hearted thanks goes to my parents and my husband, without them I would not have finished this work. They always encourage me when I feel like giving up. From their love I draw my strong passion to continue this work until I finish it.

Luo Dong

Department of Civil Engineering, Faculty of Engineering,

University of Malaya,

February 2013

LIST OF ABBREVIATIONS

The abbreviations used in this thesis are listed as follow:

ASE	Amplified Spontaneous Emission
ASR	Alkali-silica reaction
BOTDR	Brillouin Optical Time Domain Deflectometry
CB	Concrete Beam
C-S-H	C=CaO, H=H_2O, S=SiO_2
CE	Continuous Wave
D-PMMA	Deuterated Polymethylmethacrylate
DFB	Distributed feedback
EMI	Electrical or Magnetic Interference
ETPFSs	Embedded Tapered Plastic Fiber Sensors
EW	Evanescent wave
FFT	Fast Fourier Transform
FBG	Fiber Bragg Grating
FP	Fabry-Perot
GI POF	Graded-index Plastic Optical Fiber
HSC	High-strength concrete
IMC	Integrated Measurement Control Instrumentation
LDSs	Laser displacement sensors

LED	Light-Emitting Diode
LVDT	Linear Variable Differential Transformer
MEMS	Microelectromechanical systems
NA	Numerical Aperture
NDT	Non-destructive testing
OSA	Optical Spectrum Analyzer
OTDR	Optical Time Domain Reflectometry
PMMA	Polymethylmethacrylate
POFs	Plastic Optical Fibers
PS	Polystyrene
PTFE	Polytetrafluoroethylene
SDOF	Single-degree-freedom
SHM	Structural Health Monitoring
SI	Step-index
SMA	Shape memory alloys
SMTPFSs	Surface Mounted TPFSs
TPFSs	Tapered Plastic Fiber Sensors
UE-FBG	Ultrasonic excitation-fiber Bragg gratings

LIST OF FIGURES

LIST OF TABLES

CONTENTS

CHAPTER 2: LITERATURES REVIEW

CHAPTER 3: DEVELOPMENT AND OPTIMIZATION OF THE TAPERED PLASTIC FIBER SENSORS FOR TEMPERATURE SENSING

CHAPTER 5: VIBRATION AND CRACK DETECTION USING TAPERED PLASTIC SENSORS

CHAPTER 1

INTRODUCTION

1.1 Background

1.1.1 Structural health monitoring

Structural health monitoring (SHM) is vital in concrete structure and has received much attention in both research and development in recent years. Housner (1997) defined SHM as the use of in situ, continuous, or regular measurement and analyses of key structural and environmental parameters under operating conditions for the purpose of warning impending abnormal states or accidents at an early stage in order to avoid any casualties as well as give maintenance and rehabilitation advice. In general, a typical SHM system is composed of the integration of sensor techniques (Bocca, 2011; Li, 2011; Park, 2006;), smart materials, data interrogation and transmission (Chen, 2010), computational power (Adeli, 2006), and processing ability inside the structures (Jiang, 2005). Among these components in an SHM system, sensor techniques play an important role on monitoring, not only on the structural status, such as stress, displacement, acceleration, and vibration, but also on the influential environment parameters—for instance, wind speed, temperature, and the quality of its foundation (Lothenbach, 2007) .

1.1.2 Sensor techniques

Conventionally, the use of sensors is mostly based on the transmission of an electric signal, which creates many disadvantages—for example, as the sensor heads are too big or not durable enough to measure interior properties when embedded into a structure. These conventional sensors are point-sensing for only one parameter at one location and cannot be easily multiplexed. The transmission signal is easily perturbed by electrical or magnetic interference (EMI), and the different demodulation techniques are required for different sensors (Escalante-Garcıa, 2001). Compared to the conventional sensors, however, fiber optic sensors provide promising sensing in a civil SHM system. Fiber optic sensors are easily embedded into the host specimen, easily multiplexed and distributed. They have a long life cycle and are EMI-free (Price, 1951). In recent years, the use of fiber Bragg grating (FBG) sensors for temperature and strain measurements has been attracting significant attention. The FBG as a sensing element inherits many advantages, such as easy multiplexing of many sensors at one transmitted fiber line, availability of the required equipment in the market, high sensitivity, being EM-free, etc. However, it also has some disadvantages, which are not easy to overcome, such as being too fragile to handle, high cost, etc. In addition to the FBG-based sensor systems, to recovery the reflected signals normally need more complicated demodulation techniques, such as an optical spectrum analyser. However, these disadvantages can be overcome by using plastic-fiber-based sensors.

1.1.3 Plastic-fiber-based sensors

Plastic-fiber-based sensors have been investigated intensively in the past years for

many applications—e.g., crack detection in a concrete beam (Kuang et al., 2003a), the curing process of a cement paste (Ferreira et al., 2012). Conventionally, the intensity modulation technique is employed to demodulate the detected sensing signals. It is different from the FBG modulation techniques. With intensity-modulation-based fiber sensor systems, it is easier to recover the detected sensing signals. An optical multimode plastic fiber is chosen in this study due to its typical properties, such as low cost, better signal coupling, larger core radius, higher numerical aperture, and larger thermal-optic coefficient, which indicates a higher temperature sensitivity in comparison to that of an optical glass fiber. On the other hand, the tapered fiber shows more potential in sensing elements, which in turn enable the ability to generate a fluorescent signal by using evanescent waves (EWs) associated with the propagating mode in optic fibers. The changing magnitude of the EW field detection can be measured by changing the output power in a tapered-fiber-based sensor (Sun and Kapoor, 2007).

1.2 The application fields of SHM in civil engineering structures

The applications of TPFS in the SHM are described in this work. The monitoring of the hydration process during the curing of concrete, the vibration of the concrete beam, and crack detection are studied in this work, which are typically and frequently encountered issues in civil engineering.

1.2.1 Hydration process monitoring of cement paste

The early-age monitoring in the performance of cement paste is one of the most important issues in the field application of an SHM system in building a concrete

structure. The curing of concrete is defined as maintaining a satisfactory moisture content and temperature in concrete during its early stages so that desired properties may develop (Escalante-Garcia, 1998). In the properties of cement paste curing, early-age cracking is a significant problem in the preparation of concrete. Cracks are initiated when the tensile stress in concrete due to the volume changes exceeds its tensile strength, which is generally only 10% of the compressive strength. Generally, the early-age volume change is related to chemical shrinkage, autogenous shrinkage, creep, swelling, and thermal expansion. Current studies show that thermal effect and autogenous shrinkage are the two major factors of early-age cracking in cement and concrete. Thus, detecting the properties of cement paste curing has been explored by many sensor techniques—e.g., thermocouple for temperature detection and FBG sensor for temperature and strain monitoring.

1.2.2 Vibration and cracks detection

In civil engineering, the formation and propagation of crack induces the degradation of concrete structures. Crack width beyond 0.2 to 0.4 mm (depending on environmental exposure) may lead to durability problems associated with steel reinforcement corrosion. When the crack enlarges beyond 1 to 2 mm, it may be caused by overloading when a natural disaster occurred, such as flood, strong vibration, etc. It is a sign of severe damage, which requires immediate closing of a facility. Thus, today crack detection is becoming a specific field of study in SHM, which is fast growing and gaining popularity and acceptance in engineering application. This method is a nondestructive evaluation and quantification of parameters in evaluating a structural

system; early detection of changes in its load-resisting properties can avoid any deterioration during its design life.

1.3 Objectives of the thesis

The general objective of this research is to assess the performances of the TPFSs in the application fields of SHM—for instance, to characterize the early-age hydration process of cement paste and to detect the vibration and crack in a concrete beam. For this research, the specific objectives are as follows:

1) To setup the TPFS systems for monitoring the hydration process of the cement paste and detecting the cracks and vibration in a concrete beam. To valid its performances by comparing it with the thermocouple and accelerometers.
2) To develop an embedded TPFS for monitoring the early-age hydration process of cement paste and to optimize the geometries of TPFS using a mathematical theoretical model for achieving the high-temperature sensitivity.
3) To determine the setting time of cement paste by using the FBG, TPFS, and thermocouple. To clarify the advantages and disadvantages of TPFS and FBG in the application of curing temperature sensing on the cement paste specimen.
4) To investigate the applicability and effectiveness of implementing TPFSs for monitoring the hydration process of cement paste specimen with different sizes, variant water/cement ratio, and different ambient temperatures.
5) To assess the ability of TPFSs in the detection of the vibration and crack in a concrete beam.

1.4 Research methodology

Based on the researched objectives, the methodology is divided into the following parts:

1) A plastic optical fiber possesses a higher sensitivity in sensing temperature compared to a normal glass optic fiber. Because of this significant feature, an operation in tapering the plastic optical fiber was performed, which can perturb the transmission modes along the fiber.
2) The research is mainly focused on the study of the cross-sensing of temperature and strain, especially when embedding sensing elements inside the cement paste, which may operate at harsh environments. A model is set up to distinguish the cross-sensing issues mathematically. Then, the MATLAB program is employed to simulate the theoretical model for the purpose of verifying the correctness of the theoretical analysis. Based on the theoretical model, a series of experiments will be carried out to verify the theoretical analysis—for example, the TPFS has the same taper length but has different tapered ratios, or has the same taper ratios in conjunction with different taper lengths.
3) During the experiment, the embedded TPFSs were used to study the hydration process and to determine early-age setting time of cement paste. The hydration processes of cement paste, which affected the specimen at a different size, various water/cement ratios, and different ambient temperatures, have been carried out.
4) The TPFSs were used to monitor the vibration and crack on a cured concrete beam, experimentally.

5) Experimental data were collected and analysed to fit the theoretical model. Some suggestions are drawn for future works.

1.5 Significance of the study

Due to the importance of the SHM application in civil engineering application, a system that has lower cost, high performance, multipurpose use, and long life span and that is easy to use and durable is highly desired. The achievement of the TPFS system can be used to monitor the early-age properties of cement paste and detect the vibration and crack in a concrete beam. The installation of the TPFSs is easy and flexible, either embedded or surface-mounted. Based on the related literature reviews, there are not much research works to apply TPFSs in SHM. The performance of the TPFS system had highly satisfied the requirement of the modern SHM system.

1.6 Outline of the thesis

The research presented in this thesis is organised into six chapters. An overview of this thesis is introduced in Chapter 1. Background knowledge on plastic optical fiber (POF), the hydration process of cement paste, current early-age curing temperature monitoring techniques, and vibration and crack detection techniques is described in Chapter 2. In Chapter 3, a mathematical model is developed to optimize the TPFS to achieve a higher sensitivity, theoretically. The effects of the geometries of TPFS, including taper ratio, taper length, and launch angle of the initial ray, and the surrounding temperature on the performance of TPFS are studied numerically. A set of experiments is carried out, and the results agree well with the results of the theoretical

results. Chapter 4 demonstrates two optical-fiber-based hydration process monitoring techniques—namely, FBG and TPFS. The setting time is determined from monitored curing temperature. The advantages and disadvantages of these measurement techniques are discussed. By employing the TPFS, the hydration processes of cement paste were studied from the specimen with different sizes, various water/cement ratios, and different ambient temperatures. In Chapter 5, vibration and crack detection in a concrete beam is assessed using the TPFSs. Conclusions and future works are given in Chapter 6.

CHAPTER 2

LITERATURE REVIEW

2.1 Overview of plastic optical fiber

2.1.1 Historical background of plastic optical fiber

Over the past 10 years, plastic optical fibers (POFs) have received a lot of attention particularly in the improvement of its transparency and bandwidth for high-speed data telecommunication. It was first discovered by Pilot Chemical of Boston in 1960. Compared to the conventional data transmission media such as copper cable and glass fiber, POFs offer many advantages such as low cost, weight, electromagnetic immunity, and large bandwidth over short distances (up to 1000m). Additionally, POFs are not brittle but ductile. It will stretch rather than break under increased tension; even a thick bundle of POFs is more flexible than a bundle of glass fiber (Cook, 1979; Rastogi et al., 1997). These advantages make the POF technology very suitable for many new applications in data communication, industrial sensing, and etc. The fiber core and cladding are generally made from polymethyl methacrylate (PMMA) as core and perfluorinated PMMA as cladding (Bayle, 1996). The first PMMA POFs were first commercially developed by DuPont in the United States and Mitsubishi Rayon in Japan in 1970. In a POF, the refractive index difference between core and cladding is about 0.1, which results in a high value of 0.5 in numerical aperture (NA). The high NA of POF offers a high acceptance angle as compared to glass fiber with an acceptance angle

of 16° corresponding to an NA of 0.14. These properties of POF allow the plastic connectors to be used to reduce the cost of the system and improve the light coupling efficiency from the light source to fiber.

The step-index (SI) POF with a bandwidth of 50 Mbps over 100 meters using 650 nm light was developed by Mitsubishi Rayon in 1980. At the same time, Kaino and Pollock (1995) pioneered the study of the loss mechanisms in a multimode POF. The series of peaks in the loss spectra are reported, which originated from harmonic oscillations of hydrogen atoms in the plastic chain. The most common modes are called C-H stretch modes, which are associated with carbon. While those modes are following in the infrared portion of the spectrum, the overtones continue throughout the visible. The hydrogen stretch modes become more intense in the infrared, and the Rayleigh scattering decreases as the inverse of the fourth power of the wavelength. The minimum loss in most POFs is found in the visible wavelength. Fig. 2.1 shows the loss characteristic in two types of multimode POFs: polystyrene (PS) and PMMA. As shown in the figure, the lowest loss is observed in the wavelength range of nearly 650 nm, which is considered "transparency window."

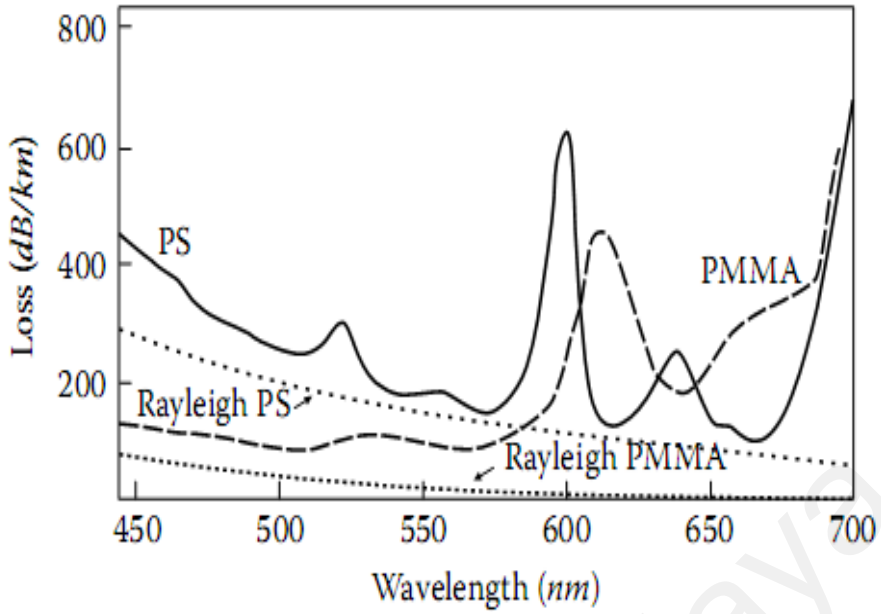

Fig. 2.1: Measured loss and contribution of Rayleigh scattering loss for PMMA and polystyrene (Zubia, 2001).

Single-mode POFs were first developed by Kuzyk et al. (1991) in the early 1990s. The core and cladding diameters of the single-mode POFs are about 8μm and 125μm, respectively. These fibers had used the Disperse Red 1 azo dye, Squarylium dyes, and Pthalocyanine dyes doped cores that were responsible for the elevated refractive index as well as for potentially having a large-intensity-dependent refractive index. However, single-mode POFs have much larger attenuation than single-mode glass fibers; therefore, POFs remain less competitive for telecommunication applications. Fig. 2.2 shows the lost spectra for various POFs, which are also compared to a silica-based fiber (Zubia, 2001). As shown in Fig. 2.2, the PMMA POF has the highest attenuation loss in the wavelength range of 300 nm to 1500 nm, and therefore, only very limited research is focused on this range. The important landmarks in the development of the POF are summarized in Table 2.1 (Zubia, 2001).

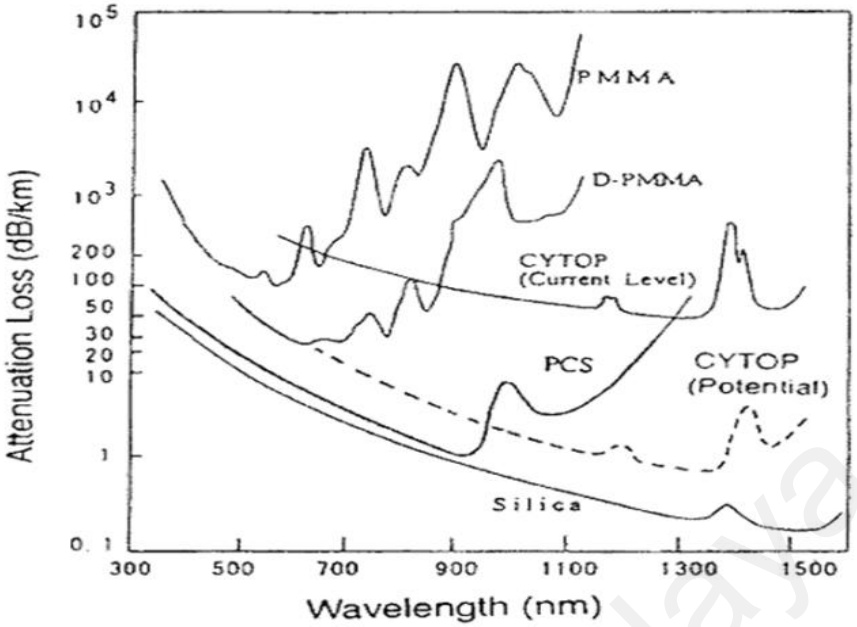

Fig. 2.2: Transmission loss spectra for various fibers: PMMA, D-PMMA, CYTOP (which is an amorphous fluorinated polymer), PCS, and silica (Zubia, 2001).

Table 2.1: The important landmarks in the development of the POF (during the past 40 years) (Zubia, 2001)

Year	Organization	Landmarks
1968	DuPont	First SI POF with PMMA core
1972	Toray	First SI POF with PS core
1982	Keio Univ.	First GI POF (1070dB/km at 670 nm)
1990	Keio Univ.	First high-speed transmission with a PMMA core GI POF (300MHz*km at 670 nm)
1994	NEC	Transmission at 2.5Gb/s over 100m by means of a GI POF at 650 nm
1995	Mitsubishi Rayon	Transmission at 156Mb/s over 100m by means of a low NA SI POF and a fast red LED

1996	Keio Univ.	First perfluorinated GI POF (50dB/km at 1300 nm)
	KAST	Theoretical estimation of the transmission speed in a GI POF optical link (PMMA:4Gb/s over 100m; PF:10Gb/s over 1 km)
1997	Keio Univ.	Transmission at 2.5Gb/s over 200m by means of a PF-coreGI POF at1300 nm
1998	COBRA, Eindhoven-Univ., COBRA,	Transmission at 2.5Gb/s over 300m by means of a PF-core GI POF at 645 nm
1999	Eindhoven Univ., Asahi Glass	Transmission at 2.5Gb/s over 500m by means of a PF-coreGI POF at 840 nm and 1310 nm
2000	Nuremberg IEEE	GI POF (Lucina) with an attenuation of 16dB at 1300 nm and 569 MHz*km
2001	Fuji film	First "POF application centre" is established
2002	Chromis Fiber optics	IEEE 1394B standard ratified, IDB-1394 for automobiles completed Announces that GI-POF is available
2005		First commercial PF GI-POF available

Note: SI, step-index; GI, graded-index; PS, polystyrene; PF, perfluorinated fiber

2.1.2 Optical characteristic of the POF

2.1.2.1 Optical loss of the POF

Normally, the bending losses are categorized as macrobending loss and

microbending loss. The macrobending of fibers means that the radius of curvature is larger compared to the radius of POFs. In contrast, microbending means that the scale of refractive index variations is comparable to or smaller than the size of the fiber region. The microbending loss is very important in the design of an optical fiber system; however, it is too complex to analyse because microgeometry is not always easy to quantify. The plastic jacket placed on the fiber induces a stress, which results in microsized variations in the refractive index or radius of the fiber. These fluctuations cause the scatter of light while the larger fluctuation can be imprinted at the interface of the core and cladding due to impurities, imperfections in the material, or fluctuations due to processing, such as differential cooling (Guerrero et al., 1993).

The bending loss of POF can be determined by the geometrical optics where the power loss at turning or reflection points is described by the leaky ray paths within the core of the bent waveguide based on an appropriate power transmission coefficient (Snyder et al., 1974). The total loss is the sum of these losses along each leaky ray path (Love, 1978; Winkler, 1979). Additionally, the bending losses can be ignored from the bend radius as it is generally enormous compared to the core dimensions. A bend fiber can be thought of as a segment of a ring, or torus, and the leaky ray paths are shown in Fig. 2.3. The meridional rays are either tunnelling rays or refracting rays, and skew rays lose power at successive reflections or turning points either by tunnelling or by refraction. The generalized Fresnel transmission coefficient T can be used to measure the transmitted power within a curved interface between two dielectric media. T is given by Snyder et al. (1974),

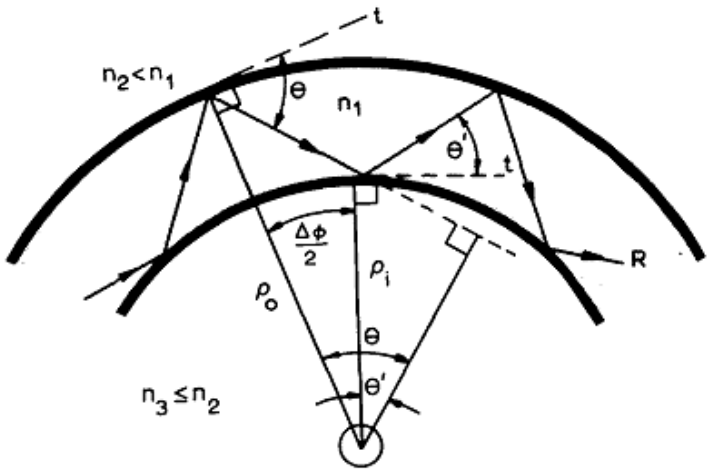

Fig. 2.3: A segment of a ring, or torus, and the leaky ray paths when the fiber is bent.

$$T(\theta) \approx 4\left(1-(\frac{\theta}{\theta_c})^2\right)^{\frac{1}{2}} \exp\left(-\frac{2}{3}k\rho\left(\theta_c^2-\theta^2\right)^{\frac{3}{2}}\right) \tag{2.1}$$

where $\theta = (\pi/2) - \theta_N$, θ_N is the inclination angle to the normal, θ_c is the critical angle of the fiber, ρ is the radius of curvature in the plane of incidence, $k = 2\pi n_1/\lambda$, λ is the wavelength in vacuum, and n_1 and n_2 are the refractive indices of the fiber core and cladding, respectively. The transmission loss in Eq. (2.1) is a ray propagating along a bend at one reflection. To determine the attenuation of a ray, the transmission loss T should be summed at each reflection. The dimensionless attenuation coefficient α equals to the number of reflections in an interval multiplied by the power loss T at each reflection (Snyder et al., 1974).

$$\alpha(\theta) = \frac{T(\theta)}{\Delta\phi} \tag{2.2}$$

where T is given by Eq. (2.1) and $\Delta\phi$ is the angle subtended between two successive reflections and given by (Snyder et al., 1974)

$$\Delta\phi = 2\theta - 2\sqrt{2\left(1-\frac{\rho_o}{\rho_i}\left(1-\frac{1}{2}\theta^2\right)\right)}. \tag{2.3}$$

The dimensionless attenuation coefficient α is given (Winkler, 1979)

$$\alpha = \frac{\eta(\theta)\rho_o\theta^2}{\rho_o - \rho_i}\left(\frac{T}{2\theta}\right)_{\rho=\rho_o} \tag{2.4}$$

Only rays' angle that is near the critical angle suffers from the significant bending loss. Then $\eta(\theta) \approx \frac{1}{2}k(\rho_o - \rho_i)(\theta_c^2 - \theta^2)^{1/2}$, so that α can be derived from Eq. (2.2) and (2.4) as (Snyder et al., 1974)

$$\alpha = k\rho_o\sqrt{\theta_c^2 - \theta^2}\exp\left(-\frac{2}{3}k\rho_o(\theta_c^2 - \theta^2)^{3/2}\right) \tag{2.5}$$

According to Eq. (2.5), a different amount of light is lost at each reflection because *T* is a function of the radius of curvature ρ in the plane of incidence, and ρ is the function of position. The attenuation decreases as either the radius of the fiber or the bending radius increases (Snyder, 1974).

In general, the optical losses of POF can be divided into two major categories: intrinsic and extrinsic losses. Intrinsic losses originate from the material and are independent from the manufacturing process, while extrinsic loss arises from impurities during materials processing. Intrinsic losses can be treated as the ultimate transmission loss limit, which cannot be eliminated by improving fabrication technologies. Basically, they are caused by the molecular vibrational absorption of the groups C-H, N-H, and O-H; by the absorption due to electronic transitions between different energy levels within molecular bonds; and by the scattering arising from composition, orientation, and density fluctuations (Kaino, 1985). As mentioned above, the hydrogen atoms in a plastic act like masses on a spring and, hence, absorb light at the characteristic frequency of the "spring" and its harmonics. As such, this type of loss can be lowered by replacing the hydrogen atoms with heavier ones such as deuterons to push the absorption resonance farther into the infrared (Kaino, 1992). However, this technique has several

disadvantages—for example, the deuterons diffuse to the surface of the material by exchanges between sites where they are replaced with hydrogen nuclei, which would cause humidity absorption, which in turn increases the attenuation significantly as a result of the strong vibrational absorption of the groups O-H, especially in the near infrared region. On the other hand, hydrogen can also be replaced by fluorine atoms to form a fluorinated plastic, which is less susceptible to diffusion because of the greater mass of the fluorine atom as well as the fact that fluorine is not an isotope of hydrogen, making it impossible for the two nuclei to exchange while conserving energy (Mark, 2007). However, fluorinated plastics have a more severe problem of being brittle compared to hydrogenated plastic. All materials absorb light at wavelengths corresponding to electronic or nuclear resonances in the molecules. As such, aside from meticulously choosing molecules with the desired windows of transparency when they are used in manufacturing a material, these losses cannot be affected by processing (Mark, 2007).

Additionally, there is another type of intrinsic loss: Rayleigh scattering which is caused by the fluctuation in the density, orientation, and composition of the material. Orientation fluctuations are caused by the anisotropy of the monomer, the crystallinity of the plastic links, and the addition of substances to achieve the desired refractive index profiles. These can also increase the composition fluctuations. Therefore, the minimum transmission losses are contributed by the absorption loss and Rayleigh scattering loss (Bløtekjær, 199; Love, 1978; Winkler, 1979). The various loss factors and the theoretical attenuation limits for PMMA, PS, and CYTOP POFs are summarized in

Table 2.2 (Liu, 1983; Guerrero, 1993; Daum, 1994). As shown in the table, PMMA has low loss characteristics at a visible wavelength.

Table 2.2: Loss factors and theoretical attenuation limits for POF (with different cores) (Zubia, 2001)

Loss factors (dB/km)	**PMMA (568 nm)**	**PS (672 nm)**	**CYTOP (1300 nm)**
Total loss	55	114	16
Absorption	17	26	10
Rayleigh dispersion	18	43	2
Structural imperfections	20	45	4
Theoretical attenuation	35	69	12

Extrinsic losses are caused by the impurities in the fiber core, fundamentally composed of transition metal ions and the hydroxyl group. However, in addition to these impurities, the most important extrinsic losses are induced by the structural imperfections of POF, which are originated from the manufacturing process (Winkler, 1979).

2.1.2.2 Dispersion

Dispersion in POFs may be separated into two main types: chromatic dispersion and modal dispersion. Chromatic dispersion is related to the dependence of the index of refraction on the wavelength. Due to various wavelengths in the waveguide, the variant spectral components of each mode are propagating at a different velocity in the fiber. This different propagating velocity causes a pulse broadening or dispersion. The modal dispersion is related to the spreading of the pulses as a result of the difference in

propagation delays among the modes as well as the dispersion from intermodal effects such as power mixing between modes and mode-dependent loss. Besides, the modal dispersion is dependent on how the modes are excited (the launching condition), the spectral characteristics of the light source, the effects of microbending, among others.

2.1.2.3 Chemical resistance properties

The polyethylene jacket serves to protect POF when it is in contact with chemical liquids. Without the jacket protection, the polycarbonate POFs can only last for 5 minutes when they are immersed in 85-octane petrol, whereas with the jacket protection, they are able to withstand it for a much longer time. The polyethylene jacket of PMMA POFs can resist liquids such as water, NaOH, sulfuric acid (34.6%), and oil. Furthermore, fluorinated POFs do not show any sign of change in attenuation within a week immersed into chemical solutions, such as 50% HF, 44% NaOH, and 98% H_2SO_4 or organic solvents such as benzene and hexane.

2.1.2.4 Thermal properties

Without the protection of a jacket, POFs can operate at temperatures up to 80 ℃–100 ℃. However, POFs lose their rigidity and transparency above the limit. If POFs are protected by a jacket made of cross-linked polyethylene or polyolefin elastomeric, its temperature limit can be increased to 125 ℃ and possibly up to 135 ℃. On the contrary, the resistance to temperature of POFs is strongly influenced by the degree of moisture in the surrounding environment. A relative humidity level around 90% results in the attenuation increase of more than 0.03dB/m (Sato et al., 2000). This can be

explained from the strong OH^- absorption band in the visible range. Fluorinated fibers have the ability to resist water absorption. Therefore, fluorinated fibers are a better choice in the applications than when they are used in humid environments (Blyler, 1999). In comparison to the conventional optical materials, the thermo-optic coefficient of silica glass material is an order of magnitude lower than that of plastic materials, and the refractive index of plastics decreases rapidly with temperature at a rate of $10^{-4}(^{\circ}C)^{-1}$. The value of the thermo-optic coefficient for variants classes of plastics ranges from -1.5×10^{-4} to $-5\times10^{-4}(^{\circ}C)^{-1}$.

2.1.2.5 Mechanical properties

Most studies on the mechanical properties of POFs mainly focus on the attenuation induced by bends and tensile or torsion stresses (Zubia et al., 1997). The Young's modulus of POFs is nearly two orders of magnitude lower than that of a silica fiber. Even a 1 mm diameter POF has a greater bending flexibility than a silica fiber with a smaller diameter due to the ductility of plastic. The bending radius of POF can be made smaller than that of silica fiber (Guerrero et al., 1998).

2.2 Hydration process of cement paste

2.2.1 The hydration process of cement

The hydration process of cement can be roughly categorised into two steps. The first step is called dissolution, which means the cement material dissolved and released the ions into the mixed water. The concentration of ion species in the pore solution increased rapidly as soon as the cement and water were combined. Finally, the

concentration increasing to the saturation point means that it is energetically favourable for some of the ions to combine and form a new solid phase rather than remain dissolved. The second step is the precipitation of the hydration process. Of course, a key point is that this new precipitation of solid phase, known as the hydration products, is different from the beginning of the cement minerals. Precipitation to reduce the oversaturation of the pore solution and allow to continue the dissolution of cement minerals. Therefore, the cement hydration of cement minerals are replaced by new hydration products as a necessary transition zone between the two programs, and holes solid state is a continuous process. The reaction between Portland cement and water over a hundred years and the dissolution of the precipitation process of hydration was first described by the famous chemist Le Chatelier.

The hydration products are different from cement minerals; the following describe the two main reasons. First, there is a new reactant in the hydration system: water. Water not only facilitates the hydration process by dissolving the cement minerals but also contributes ions to the hydration products, in the form of hydroxyl groups (OH-). Second, hydration includes the tendency for all processes to approach thermodynamic equilibrium. The stability of a phase is defined by a parameter called the free energy, which can be roughly defined as the amount of chemical and thermal energy contained in the phase. The lower the free energy, the more stable the phase. As we know, the cementation minerals are formed at temperatures exceeding 1,400 ℃ because they have the lowest free energy under this extremely high temperature. At much lower temperatures during cement hydration, the cement minerals are actually quite unstable, meaning that many other solid phases will form preferentially in their place once they

dissolve. When one phase is converted into another phase with a lower free energy, there is a release of excess energy in the form of heat. Such a reaction is termed exothermic, and the exothermic heat associated with cement hydration has already been defined as the heat of hydration.

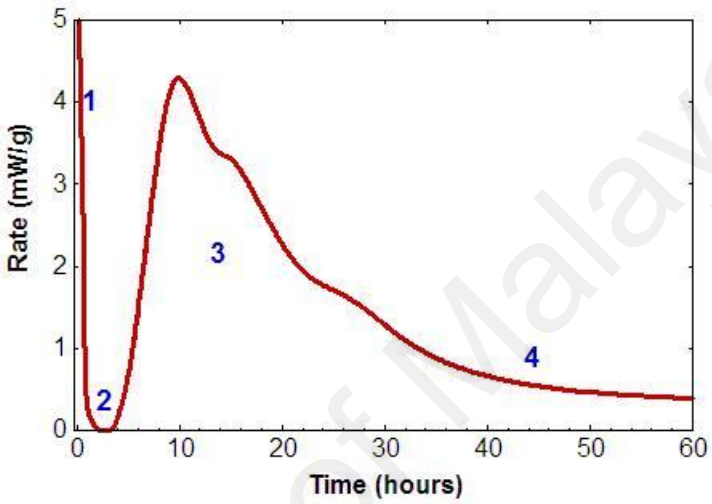

Fig. 2.4: Schematic of the rate of hydration or heat evolution as a function of time (Thomas, 2008).

Fig. 2.4 shows the rate of cement hydration over time; it can be found that the hydration process is divided into four stages. When cement and water are mixed together, they are reacted immediately and release heat as the cement dissolves. The chemical reaction lasts for less than one minute (see stage 1). The time of stage 1 is short because of the rapid formation of an amorphous layer of hydration product around the cement particles, which separates them from the pore solution and prevents further rapid dissolution. In stage 2, an induction period, there is almost no reaction that occurs. The precise nature of the induction period is not fully known. At stage 3, the rate of reaction increases rapidly, reaching a maximum value usually less than 24 hours after casting, and then decreases sharply again to less than half of its maximum value. Both the maximum

reaction rate and the time strongly depend on the temperature and the average particle size of the cement.

Stage 3 is characterized by a continuous and relatively rapid deposition of hydration products (primarily C-S-H gel and CH) into the capillary porosity, which is the space originally occupied by the mixed water. It causes a large decrease in the total pore volume and a concurrent increase in strength. The microstructure of the paste at this point consists of unreacted cores of the cement particles surrounded by a continuous layer of hydration products. The final period (Stage 4) is called the diffusion-limited reaction period. In this stage, the dissolved ions diffuse out and precipitate into the capillary pores, and water diffuses inward to reach the unreacted cement cores. These diffusion processes become slower as the layer of hydration products becomes thinner.

2.2.2 The degree of hydration

The degree of hydration can be measured in a few different ways, including x-ray measurement to determine how much of the minerals remained and the loss-on-ignition measurements to determine how much bound water is contained. Another common method is to sum the amount of heat released by the paste (as measured by thermal calorimetric) and divide this value by the total amount of heat liberated for complete hydration. The latter value will depend on the mineral composition of the cement. Another parameter that can be used to monitor the progress of hydration is the compressive strength. This is not a precise measure since the strength depends on many factors other than the progress of the chemical reactions, but it is very practical since the

development of strength is the primary reason for using cement and concrete in the first place.

Fig. 2.5 shows the degree of hydration and the strength of a Type I OPC paste plotted as a function of time on the same figure. In Fig. 2.5, it can be seen that the degree of hydration and the strength agree with each other, particularly at a later stage. This is because the strength of cement paste primarily depends on the amount of capillary porosity, and the amount of capillary porosity decreases in proportion to the amount of hydration that has taken place. This decrease occurs because the C-S-H gel phase (including its internal gel pores) significantly occupies more volume than the cement minerals.

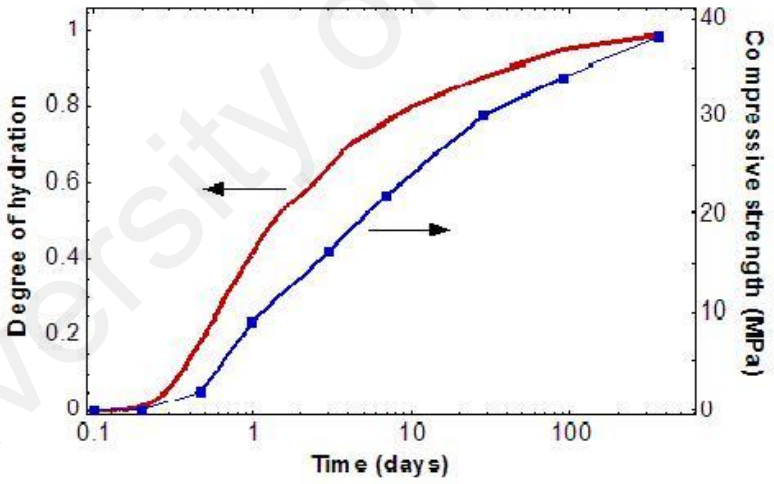

Fig. 2.5: Typical development of the degree of hydration and compressive strength of Type I Portland cement over time (Thomas, 2008).

2.2.3 Major Influencing Factors of Hydration

The cement hydration process is a combined series of complicated chemical reactions and numerous influencing factors. The following major factors predominantly determine the whole exothermic hydration process of cement.

- The chemical composition of cement
- The fineness of cement
- The water/cement ratio of concrete mixture
- The temperature of hydration reaction especially at the initial concrete mixture and casting stage

2.2.4 Models for hydration process

Carleson (1937) was perhaps the first one who pointed out that the heat of hydration generated by cement would be influenced by the actual temperature of reaction. Rubinsky (1954) might be the first one who actually took the temperature dependence of hydration reaction consideration explicitly. Another distinct characteristic of Rubinsky's approach was that the evolution of the degree of hydration is focused on. The degree of hydration acts as a predominant parameter in modern numerical models for the evaluation of thermal problems, continuously varying material properties, and the risk of thermal cracking of concrete mixture at an early age. After Rubinsky's initial work, several authors like Linvill (1990), Springenschmid (1995), and Van Breugel (1980) have worked in a similar direction that the temperature dependence of hydration reaction of cement was explicitly taken into consideration when simulating the temperature history of concrete mixture.

During the past decades, continuous research has been conducted in this field, and numerous papers presented original methods and models to simulate the exothermic hydration process and the associated temperature history. Especially in recent years, with the extensive application of high-performance computers and the emergence of

more advanced finite-element analysis software, more and more research interest has been focused on adopting a numerical simulation technique to predict the exothermic hydration process of cement-associated temperature history of concrete mixture (Thurston, 1980; Tsukayama, 1974; Wang, 1994). Upon considering the complexity of the research subject involving so many interdependent processes and mechanisms, the choice of numerical simulation seems inevitable.

Numerical simulation techniques possess considerable advantage over the past empirical methods when simulating the exothermic hydration process and the associated temperature history. According to Yamazaki (1994), as a versatile and quantitative tool, an ideal and complete numerical model should be able to predict a series of variables such as the heat of hydration, the temperature history, strength development, thermal stress development, and the risk of thermal cracking. Generally, numerical simulation models for predicting the exothermic hydration process of cement and the associated temperature history of concrete mixture can be classified into two groups—i.e., microlevel models and macrolevel models (Van Breugel, 1995). Microlevel models are exploited in the field of material science, focusing on physicochemical processes and mechanism on the microlevel scale, aiming to describe the exothermic hydration process from fundamental material science perspectives. Some microlevel models have been elaborated by Van Breugel (1995) and Garboczi (1992) of the heat of hydration and the associated temperature distribution on engineering level, which directly focuses on macro-level performance of thermal properties of concrete at early ages. These models are adopted in the engineering practice to decide on the time of formwork stripping, application of simulation, or precooling of concrete.

No matter which kind of model is employed, considerable attention should be paid to the way in which the model allows for the simulation of the exothermic hydration process and the continuous change of the thermal properties of cement. More and more attempts are made to bridge the gap between the microlevel and the macrolevel models by introducing general-acknowledge concepts of material science into the marcolevel models.

Emborg (1994) carried out an experimental investigation on the effect of temperature variation in concrete. Finite element model was adopted to evaluate the temperature history of concrete mixture and the associated thermal stress distribution in concrete structure. This model took both the influence of creep in early-age concrete and the temperature dependence of the hydration of cement into consideration. Tam (1993) indicated that the concreting of thick sections involves large-volume placements, described the typical case histories of such placements *n* the tropics including the mixtures used and the overall dimensions of the members, and finally discussed the requirements of concrete mix design and precautions to be considered in relation to the planning and execution of large placements as well as the use of insulation to control temperature differentials. Loo (1995) proposed a layering method to cool large volumes of concrete in which only the central portion of concrete is cooled for the reduction of temperature differences within the concrete mass. Meanwhile, the associated computer simulation involving the application of this layering method was presented. Lu (2000) estimated the maximum temperature rise and temperature differential in concrete elements at an early age using the profile of adiabatic temperature. This study looked at how concrete mixtures, concrete element dimensions, and types of formwork affected

the maximum temperature rise and temperature differential. Ballim (2004) developed a numerical model to predict the temperature distribution of early-age concrete. A two-dimensional finite element thermal analysis was employed to simulate the transient heat transfer between the concrete and the surrounding environment by taking into account the type and content of concrete, boundary, and environmental conditions (such as solar radiation and artificial heating.

On the basis of the independent hydration concept, Van Breugel (1995) proposed independent hydration for mineral compounds in cement and disregarded any mutual influence among them. Such a conclusion made it possible to simplify the complicated hydration process of the entire cement by subdividing it into the individual hydration reaction of each process of each mineral compound in cement. Similarly, Kishi (1995) developed a numerical model for simulating the exothermic hydration process of cement. It described the entire hydration process as a combination of hydration reaction of individual mineral compounds in cement. Meanwhile, differences between various cements were attributed to their chemical composition. The rate of the heat of hydration for each mineral compound was expressed with two material functions: the reference rate of the heat of hydration (i.e., the rate of the heat of hydration per unit mass of mineral compound in cement under specified hydration conditions) and the thermal activity. Taking into account the temperature dependence of hydration reaction of an individual mineral compound, the exothermic hydration process of the entire cement could be quantified for any given temperature history.

2.3 Hydration process monitoring techniques

The heat of cement hydration causing thermal stresses and associated thermal cracking in mass concrete structure at early ages was a well-known observed phenomenon. Cement hydration is an exothermic process, while the amount of heat released is the main consideration especially in mass concrete structures. The relatively low thermal conductivity of concrete prevents the heat generated by the hydration of the concrete structure core from dissipating to the surrounding environment. Meanwhile, considerable thermal energy may exchange between the external surface of the concrete structures and the surrounding environment. Therefore, great temperature gradient arises across the mass concrete section, which results in unequally volumetric changes. Thermal stresses appear while restrained by external and internal restraints, and when thermal stress exceeds the ultimate strength of concrete, thermal cracking occurs.

In the past decades, cracks formed in many medium-sized concrete structures such as foundations, bridge piers, tunnel linings, and pavements have also attracted increasing attention. In many cases, drying shrinkage appears to be of minor importance, while the heat of hydration and the associated temperature gradient have been proved to be the primary cause of restraint stresses and cracking formation (Springenschmid, 1998). In order to enhance the performance and durability of concrete structures, essential measures must be taken to control temperature rise, thermal stresses, and thermal cracking caused by the heat of hydration generated in concrete structures. Actually, various methods of avoiding thermal cracking have already been employed mainly for the construction of mass concrete dams and other hydraulic structures. For example, in order to reduce the heat generated by the hydration of cement, various

mineral admixtures have been adopted extensively. Further progress to lower the maximum temperature rise has been made by using concrete with lower unit content of cement, precooling the concrete materials, limiting the thickness of the casting layer of concrete pours, and pipe cooling. However, the effectiveness of these measures can only be evaluated on the basis of qualitative analysis, and it is still difficult to quantify the effectiveness of these measures accurately.

To overcome this difficulty, temperature-related criteria—i.e., to stipulate the maximum permissible temperature rise or the maximum permissive temperature gradient across the concrete section of the concrete pours specified by many codes and standards—are commonly adopted in situ worldwide. However, these criteria often oversimplify the complex problem and focus only on ultimate temperature rise or temperature difference and neglect some essential properties of a particular concrete pour such as its temperature data, its tensile strength, and its coefficient of thermal expansion. Meanwhile, practical experience often shows that temperature-related criteria are not so reliable as ever expected (Mangold, 1994).

To determine the heat of hydration of cementitious materials, conventionally, the calorimetry test is employed heavily because it measures the heat of hydration with time. Conventionally, there are two types of calorimetry tests: isothermal calorimetry and adiabatic calorimetry. The isothermal calorimetry test measures the liberated heat of a specimen when the specimen and ambient maintains at the same temperature. The adiabatic calorimetry test monitors the liberated heat of a specimen for the specimen without heat loss. However, the pure isothermal calorimetry test and adiabatic calorimetry test are impossible to implement without expensive equipment; thus, a

semiadiabatic calorimetry test is more frequently used. In all of these calorimetry tests, the temperature sensor plays a vital role in the whole system.

2.3.1 Conventional curing temperature monitoring techniques

Conventionally, a thermocouple embedded into the cement paste is used as a temperature sensor for concrete structures (Bushnell-Watson, 1990; Bushnell-Watson, 1990b; Glišić, 2000). Generally speaking, a thermocouple can provide temperature measurement with an acceptable accuracy; however, it is a typical local sensor, which only provides the temperature measurement at a certain location. Norris et al. (2008) have monitored the temperature and moisture in concrete structure using embedded microelectromechanical systems (MEMS) sensors. The MEMS sensor with the size of 2 mm × 2 mm was fabricated by using a combination of standard and customized semiconductor processing steps. The MEMS sensor was then calibrated at a relative humidity range between 26% and 100% and to a temperature range between -20 ℃ and 47 ℃. The calibrated sensor was used to detect the curing temperature and humidity of cement paste from 24 hours to 230 days.

William et al. (2011) demonstrated a concrete curing monitoring employing an embedded wireless sensor. Wireless sensors with temperature and relative humidity measurement capabilities were designed with onboard communication using the 433 MHz ISM band and embedded into concrete. An EMI method was used to allow the wireless sensor to be used in an embedded system incorporating the AD5933 impedance chip. Analysis of the data from the sensor showed that while temperature readings were reliable, the method of measuring relative humidity, using a shielded humidity sensor,

may not be suitable for use over the full lifetime of the structure.

2.3.2 Optical-fiber-based curing temperature monitoring techniques

In recent decades, optical fiber sensors have been commonly utilized in the composite material field due to their predominant advantages, such as small size, low cost, and capability to avoid electromagnetic influence (Slowik, 2004; Wong, 2007). Okabe (2002) presented a fiber-optic Fresnel reflection technique for supervising the curing process. In the late 1980s, FBG sensors attracted considerable attention and were employed in aerospace and structural engineering. FBG sensors are small and compatible with common polymeric materials and are therefore easily embedded close to the internal sensing site in a composite structure without introducing significant defects. In 1990, FBG sensors were embedded into composite materials to monitor the curing process, to monitor the epoxy curing, and to find the glass transition temperature with intensity changes (Giordano, 2004; Ren, 2007; Wang, 2007). To make FBG sensors less susceptible to local damage, such as cracks, which widely exist in existing civil infrastructures, the gauge length of a FBG sensor can be extended from several millimetres to centimetres or even metres for macrostrain measurements (Ansari, 2003; Gu, 2000; Moaveni, 2008; Ni, 2011; Xu, 2007).

Laboratory equipment have been designed to investigate curing and other properties of cement and concrete using the above instrumentation by Wilson (2004). Xie (2002) demonstrated a novel system to investigate the Bragg wavelengths shift of an array of in-FBGs through a digitizing method. A grating scale was employed to read out the output of the system. The FBG sensor was utilized to assist in describing the

process of drying and evaporation of cement pastes. A fluid mechanics approach for water evaporation based on the boundary layer theory, mass transfer, diffusion, and convection was described by Bakhshi (2012). A parametric study was conducted on the effect of boundary layer temperature, wind speed, and relative humidity; and evaporation characteristic length on the calculated evaporation rates was conducted. Results show that given appropriate environmental parameters, evaporation rates can be predicted with a good degree of accuracy. Discrete modelling of plastic cement paste subjected to drying was also conducted by Slowik (2011).

A sensor embedded in a composite laminate can act as a temperature transducer during the composite cure mechanism. Once the composite is cured, the same sensor can be used to provide information on the mechanical changes that influence the performance of the material. Murukeshan (2000) used the FBG sensor for monitoring the composite curing process. Results were obtained with an associated FBG sensor system for the cure monitoring of smart composites. The performance of the embedded FBG sensor smart composite specimens under three- and four-point bending conditions was also investigated.

Zou (2012) used the Fabry-Perot (FP) fiber optic temperature sensor to investigate the effects of the concrete hydration process. The FP temperature sensor was fabricated by controllable chemical etching and adjustable fusion splicing. Detailed optical properties of the sensor were theoretically analysed and temperature calibration experiments were performed. A sensor with a 90 μm cavity length was demonstrated to have a temperature sensitivity of 0.01 nm/℃ and a linearity coefficient of 0.99. The FP sensor was embedded in the concrete structure for sensing the temperature change

during the early age of hydration. The final setting times of 13.52 h (w/c = 0.4), 14.16 h (w/c = 0.5), and 15.2 h (w/c = 0.6) after concrete casting were found.

The interior shrinkage deformation and temperature change of high-strength concrete (HSC) at a very early age—i.e., the first 24 hours from casting and up to an age of 72 hours—was investigated experimentally using optic fiber sensors and thermally sensitive resistors. The initial and final setting times of HSC were also investigated. Results show that two turning points (I and II) on the development curve of deformation—both represent the onsets of the variation of rigidity in fresh HSC—can be recognized as the initial and final setting times, which are evaluated around 4.5 hours to 5.7 hours and 9.0 hours to 11.8 hours, respectively. Also, the higher the fly ash or silica fume replacement ratio, the longer the setting times. The setting times of HSC evaluated from the curve of temperature development are quite close to those measured from the deformation curve. In addition, the HSC setting times determined by penetration resistance method (ASTM C403) demonstrate unusually large values. This method is therefore not advised to be used to measure the setting times of HSC (Liu, 2002).

Currently, one of the most practical approaches for distributed strain and temperature monitoring is the optic fiber sensing technique based on the optical time-domain reflectometry (OTDR) technique, which was originally developed for telecommunication systems. Gu et al. (2000) developed a distributed optical fiber sensor based on the intensity of the optical power. Compared to the traditional OTDR, a more attractive optical fiber sensing technique is based on the Brillouin optical time-domain reflectometry (BOTDR). The spatial resolution of a BOTDR optic fiber

sensing system is determined by its light pulse width. Because damage in a concrete structure is usually local, it is crucial to study the possibility of the BOTDR technique for local damage detection of engineering structures. Some investigations on the application of BOTDR techniques for SHM have been carried out in the last few years, and significant progress has been made by researchers like Mufti (2003) and Wu (2006, 2008).

Fiber sensors employing plastic optical fiber normally inherit many advantages, such as low cost and easy installation, compared to the FBG and BOTDR techniques. Afromowitz (1990) proposed that polymer fiber be embedded into composite materials to monitor the refractive index changes in the composite materials during the curing process (Mufti, 2003). The application of optical fiber to monitor the cement curing process has been conducted by Ferreira (2012). A method was proposed which is based on the scattering of the propagated optical signal in grooves imposed to the fiber. By monitoring the intensity of the transmitted light signal with time, the cement setting rate along all the curing period was determined. The system had enough sensitivity to analyse a curing period of 28 days, where the received optical power was 5% of the initial value. Curing monitoring of composite material was also conducted by Chiang (2011).

2.4 Vibration and crack detection techniques

An assessment of cracks in a concrete beam is crucial for the safety and cost-effectiveness of concrete structures. A concrete structure can be degraded through the formation and propagation of cracks. Cracking comes in a number of varieties

according to the visual appearance and structure of the cracking and the causes. Map cracking is commonly associated with the alkali-silica reaction (ASR) in poorly reinforced structures (Fan, 1998; Fournier et al., 2000); D-cracking is due to freezing of an aggregate that has reached a threshold level of moisture saturation (Childs, 2008; Hanna, 2003). Other forms of cracking can be caused by sulfate attack (Neville, 1995; Tian, 2000). Cracking of fresh concrete is also a common experience (Ravina, 1968), being more readily found on large slabs due to the larger distances that the concrete moves due to its drying shrinkage. The occurrence of large temperature variations as the concrete setting is also a common cause of cracking. Shear stresses and tensile strains and differential thermal expansion (as would occur most readily due to fire damage of a concrete structure) all cause cracking in concrete as well as the growth of existing cracks, which may lead to failure of the concrete structural element.

Crack formation width beyond 0.2 to 0.4 mm may induce durability problems and the corrosion of steel reinforcement. Larger widths of more than 1 to 2 mm are signs of severe damage and the need of the immediate closing of the facility. Crack information is significant and can be used to adopt the appropriate rehabilitation method to fix the cracked structure and prevent any catastrophic failure (Fujita, 2006). Therefore, the way to get crack information is to become an indispensable approach to assess the health of a structure. In the past, several efforts were made to detect the crack in a concrete structure, including the frequency response methods (Maeck, 2000; Ndambi, 2002), the processing of crack image (Dare, 2002; Sohn, 2005), wavelet techniques (Lee and Liew, 2001; Umesha, 2009; Xiang, 2008), piezoceramic transducers (Bhalla, 2004; Song, 2007), acoustic microscopy (Kim, 2003; Zinin, 2000), and fiber-based techniques

(Childs, 2008; Gu, 2000; Wan, 2007; Kuang et al., 2003a).

2.4.1 Conventional crack detection techniques

Farrar et al. (1999) studied the frequency response of a three-span steel girder bridge in one of the spans in order to simulate fatigue cracking. The span in concern was 163 ft with a prismatic 12 ft deep steel girder. Different degrees of damage were induced at the midspan by varying the depth and the extent of the roach cuts, starting from a 2 ft cut at the centre of the web to a 6 ft cut to the bottom of the web with its flanges cut completely. The vibration response of the bridge was obtained from the measurement of acceleration signals resulting from forced vibration caused by oncoming traffic. FFT was performed on the signals, and the modal frequencies for the first six modes were revealed. It was found that the maximum relative change in frequency due to damage was the fundamental frequency, registering a total of 10% reduction for the most severe damage induced, with the other modal frequencies registering only a 2%–6% reduction.

Maeck (2000) and Ndambi (2002) conducted studies on the crack identification of RC beams by stiffness determination from its frequencies and mode shapes. Different degrees of flexural damage was induced in the RC beams through a three-point and four-point bending configuration. Free vibration response of the slab was recorded at different damages. Using model updating, whereby the measured frequency was used to infer the damage, parameters (damage extent and depth) were minimized off the differences between numerical, experimental, and modal parameters. On the other hand, Ndambi (2002) used damage indices (MAC and COMAC) obtained from the

computation of correlation coefficients between different measured acceleration mode shapes, with measurements taken at 31 deferent locations along the beam, to obtain the magnitude and location of the flexural cracks. Both studies showed that the beam frequencies change significantly at different degrees of damages with an average of 26% total reduction in fundamental frequency when the beam was loaded to yield state. One main drawback of these studies lies in the method used for the damage quantification of the beams. Both literatures inferred the damage in the slab from the measured frequencies and mode shapes using optimisation and stochastic methods. These methods were largely heuristic without proper validation from experimental observations. This means that although the inferred reduced stiffness, damage extent, and crack locations gave an approximate idea of the existing damage in the slab, the studies did not show how well such inferred quantities correlate with actual experimental observations.

Sohn et al. (2005) proposed a crack monitoring system to quantify the change of cracks from multitemporal images. The images were taken from an off-the-shelf digital camera. A series of image processing techniques were used to extract crack information. It is important to transform the crack coordinates of cracks extracted from each image into the same object coordinates of the concrete surface. To overcome this issue, a two-dimensional projective transformation based on the modified iterated Hough transform algorithm was employed to recover such a geometrical relationship automatically.

Lee and Liew (2001) adopted the wavelet analysis of numerically simulated response signals of a beam with the purpose of locating damage. Two cases were studied—namely, a fixed-ended beam with a damage modelled in the form of a hinge

and a simple-supported beam with a transverse open crack. This study uses the real and imaginary parts of the wavelet transform (Newland, 1993), which characterise the local information along the length of the beam. The numerical results showed that the wavelet coefficient changes significantly at the damage points even for a very low level of damage, with the real part showing more significant changes than the imaginary part. The main weakness of this study is that a static spatial displacement signal was used for wavelet analysis, which is often practically difficult to obtain under ordinary laboratory and field conditions. Furthermore, although this study indicates the potential of this approach for damage detection, serious complications may arise when applied to field results due to the complicated nature of damage that cannot be duplicated numerically as well as the presence of noise.

Piezoceramic transducers have been used to detect the crack in a 6.1 m long reinforced large-scale structures (Song, 2007). Piezoceramic transducers were embedded in the concrete structure at predetermined spatial locations prior to casting and embedded in planar locations near one end of the bent cap. Stain gages, LVDTs, and microscopes were used in the experiments as references. The wavelet packet was used to analyse the recorded signal, in which one embedded piezoceramic patch was used as an actuator to generate high-frequency waves and the other piezoceramic patches were used as sensors to detect the propagating waves. By using this technique, the authors claimed that it has the ability not only to detect the existence of the crack but also to monitor the growth of cracks. Compared to the referenced techniques, the proposed method achieved better sensitivity.

Scanning acoustic microscopy (SAM) has proved to be of great value in the

detection of cracks in various materials such as ceramics, metals, and fiber composites. Recently, it has been found that detectability of cracks and voids in cement paste is greater than in refection optical microscopy. Crack detection in concrete composites using acoustic microscopy was studied by Zinin et al. (2000). A frequency range of 100–400 MHz can be used to detect the crack at the aggregate/paste interface and subsurface cracks in aggregates with high sensitivity.

2.4.2 Optical-fiber-based crack detection techniques

Among the techniques described above, however, the segmentation of cracks from the concrete image is particularly difficult because of the irregularities in crack shape and size, various blemishes, and irregularly illuminated conditions. These often lead to false detection. Due to material nonhomogeneities, the exact locations of cracks in a concrete structure cannot be predicted (although crack directions can often be accurately obtained from analysis). Conventional "point" sensors, which measure strain at a local point, can easily miss the crack (Ansari, 1993; Voss, 1994). With integrated sensors, which measure the displacement between two points separated by a relatively large distance, it is not possible to distinguish between the harmless case of many cracks and the undesirable situation of one widely open crack (Wolff, 1992). To overcome the limitations of existing crack sensors, fiber-optic-based "distributed" sensor inherited many advantages—for example, (i) it can detect the formation of cracks without requiring prior knowledge of exact crack locations, (ii) it can carry out continuous monitoring once the crack is formed, and (iii) it can detect and monitor a large number of cracks with a very small number of fiber sensors.

Thus, crack detection in a concrete beam employing BOTDR techniques was studied by Wu et al. (2008). In the study, two basic optical fiber installation methods, overall bonding installation and point fixation installation, were proposed and investigated experimentally for a reinforced concrete bending beam. The experimental results showed that the n-round superposition installation method can effectively and correctly detect the total crack width with a relatively local region.

There are good prospects for the development of ultrasonic excitation-fiber Bragg gratings (UE-FBG) damage detection techniques in the field of nondestructive testing (NDT). However, corresponding strain sensing theories are few and only applicable to the embedded FBG sensors in composite structures. Tan et al. (2012) followed the following procedure. First, a four-cylinder sensing model for both the embedded and the glued FBG sensors is established by introducing a surface-bonded effect coefficient obtained from the simulation analysis in this paper. According to the shear-lag theory, an improved strain-sensing function is derived from this model by considering the contribution made by the elastic modulus of the host material. Then, based on the above function, the strain-sensing characteristics are analysed. Finally, the system with an ultrasonic transducer to excite FBG and a demodulation device employing a tunable laser to detect FBG wavelength shifts was established to validate the theoretical analysis. Results showed that the ultrasonic strain-sensing ability of the FBG sensor decreased with the increase of ultrasonic frequency and glue thickness.

The fiber Bragg sensor has also been utilized to measure other parameters. Sensors are involved in the corrosion monitoring and structural monitoring of concrete structures. Muralidharan et al. (2007) monitored the corrosion of concrete structures by

employing an embeddable reference sensor. The performance was studied in the absence and presence of chloride ions for the exposure period of 18 months. Polarization behaviour and impedance characteristics of the sensor in mortar were carried out in three aqueous solutions—namely, distilled water, 3% NaCl solution, and natural seawater.

Lin et al. (2010) used a FBG measuring system to detect dynamic seismic signals in underground structures, rock mass, bridges, etc. To improve the sensitivity of dynamic strain measurement, the wavelength of the used distributed feedback (DFB) laser is automatically optimised by the actual DC photovoltage measurement. A strain calculation method is given. An adaptive filtering algorithm is proposed and applied to the noise reduction and the detectability of seismic signals. Results from laboratory and field experiments are given. This technique can be applied to the detection of dynamic strain variations down to 10^{-9} at 1.7 kHz in underground rock mass excavations and to the monitoring of bridge structures.

The strain measurement of concrete under uniaxial and biaxial compression by an embedded fiber-optic sensor was conducted by Li et al. (2003 & 2004). Both the fiber core and the matrix concrete were supposed to be elastic, whereas the coating of the optical fiber was supposed to be ideal elastic plastic. The existence of a coating on an optical fiber results in a difference between the strain of the matrix concrete and the strain sensed by the embedded fiber-optic sensor. Dong-Sheng et al. (2012) designed, validated, and applied a new flexible FBG sensing beam that can effectively measure dynamic lateral displacements inside a soil mass in a shaking table test. The special flexible FBG sensing beam was fabricated by employing a series of FBG sensors along

with the design of temperature compensation. Based on this design, equations of converting strains to lateral displacements were derived by using both differential and integral methods. Subsequently, the effectiveness of the FBG sensing beam has been verified in a shaking table test with noncontact laser displacement sensors (LDSs). The dynamic lateral displacements at different depths of the soil mass in the shaking table box throughout time history are calculated by differential and integral methods and compared with the results of LDSs. The comparison validates the measurement accuracy of the FBG sensing beam. The flexible FBG sensing beam is compatible to the stiffness of the soil and is capable of measuring dynamic lateral displacements with good accuracy in a shaking table test.

Antunes et al. (2012) monitored an adobe masonry structure with an optical fiber accelerometer and a network of 13 multiplexed displacement sensors. Results demonstrated that optical sensors can be useful in the static and dynamic monitoring of large raw-earth masonry structures. A novel electromagnetic force sensor has been proposed by Zhao et al. (2005). The force created by the input current results in the distortion of a cantilever structure. A couple of FBGs are mounted at either side of the cantilever. By monitoring the wavelength shift difference of the two FBGs, the electromagnetic force can be obtained and the cross-sensitive problem of the FBG sensor can be solved by compensating the temperature effect.

Crack detection using POF have received much attention. Kuang et al. (2003a) employed the plastic optical fiber as a monitor for initial cracks, postcrack vertical deflections, and failure cracks in concrete- and steel-reinforced concrete beams subjected to three- and four-point flexural bending test. The fibers were

surface-mounted. Two samples of each material were brought to their peak load, and then the load was released. This allowed for a measurement of the crack width. Four different samples of each material were loaded beyond their peak load in order to monitor vertical deflections in the cracked samples. The outcome of the three- and four-point bending tests showed that the intensity of light decreased gradually until cracks at the peak load appeared, resulting in a dramatic drop in intensity of the POF sensor. Therefore, by monitoring the intensity of the light deflection and crack, propagation can be recognized. Also, the POF exhibited necking at the crack site as well as a whitish colour indicating "stress crazing." The POF was proved to withstand large deflections and cracks to degrees that would not be obtainable by glass optical fibers.

Kuang et al. (2002) investigated an intensity-based POF sensor for curvature and strain measurements. Rectangular and H-section samples in this study were subjected to three-point bending flexural tests, and aluminium dog-bone specimens were tested in tensile loading conditions. POF sensors were surface-mounted with the portion of the sensitised region oriented away from the host specimen, and the light intensity was monitored during loading. Since the POFs were not expected to be as sensitive to in-plane loads, the fibers in the tensile tests were applied in a curved manner with the segmented surface facing outward from the curve. As the aluminium specimen was loaded, the POF would straighten, reducing the curvature of the POF and increasing the overall light transmission in the fiber. Results of quasistatic revealed a highly linear response to axial strains up to 1.2% and bending strains up to 0.7%. Cyclic tests were also run for which the POF sensor predicted the unloading and loading behaviour of the beam with a small amount of hysteresis and acceptable repeatability. Experiments with

the H-section beam showed the ability of the POF to monitor compressive forces exerted from the flexure test with good repeatability.

Xiong et al. (1999) fabricated POFs in their laboratory and wrote Bragg gratings in these fibers. The gratings were capable of being tuned within 12 nm of the wavelength range without a measurable change in the reflection spectra, an ability that was noted as being 10 times the range achieved by silica fiber gratings. The cladding was initially prepared from PMMA preforms according to Peng et al. (1996). At 1.3% strain, the spectrum moved by 20 nm and widened to 0.9 nm. The yield strain was determined to be 6.1% with a potential recoverable strain up to 13% according to material parameters from Emslie (1988).

2.4.3 Optical-fiber-sensors-based vibration detection techniques

Davis et al. (1996) reported the shape and vibration mode sensing using an FBG array. In this paper, they demonstrate that a multiplexed FBG sensor array can be used to monitor the DC and dynamic strain characteristics of a simple structure. The FBG array was attached on the surface of a cantilever beam to determine the shape and vibration mode. A Rayleigh-Ritz-type analysis was employed to predict static beam deformations through the use of three trial functions and the strain information obtained from the FBG.

Ling et al. (2004) studied an embedded multiplexed FBG sensor to monitor the dynamic strain and vibration for intact and delaminated composite beams under various external excitations. A dynamic strain calibration of the FBGs and surface-mounted strain gauges was reported to find out the correlation between the strain and the

photovoltage. In the experiment, the monitoring results of the FBG were compared to a laser vibrometer and an accelerometer. The experiment results revealed that the embedded FBG has the ability to measure the dynamic strain and identify the existence of the delaminating of the structures.

The dynamic structural displacement estimation using displacement-strain relationship and measured data were investigated by Kang et al. (2007). The strain data was obtained by employing the FBG sensors. Four FBG sensors were attached on the surface of an aluminium, and an acryl beam was subjected to various loading conditions, and the deformed and vibration shapes were reconstructed from the detected strain signals. The estimated displacement results agree well with the displacement detected by the laser displacement sensor. A shape reconstruction algorithm using finite element model combined with the use of the Brillouin-scattering-based optical fiber sensor was proposed by Nishio et al. (2009). The constructed algorithm was applied to the reconstruction of the deflection of a composite laminate specimen, in which the optical fiber sensor was embedded. The results demonstrated that the reconstruction accuracy can be improved by using weight values determined from the nonuniformity index of the strain distribution profile for each data point. The authors also declared that this algorithm can be applied to more general structures without considering the ill-posedness of the inverse analysis.

The dynamic strain measurement of a clamped-clamped composite beam by using an embedded FBG and surface-mounted strain gauge was studied by Ling et al. (2006). The experimental results show that the relationship between the photovoltage and the strain measured by the FBG and strain gauge has a linear slope when the strain value

exceeded 1 microstrain. Internal strain measurement in cross-ply carbon-epoxy composite plates under dynamic loading was studied by employing embedded FBGs (Jeannot et al., 2010). In this paper, the signal intensity of FBGs were demodulated via a Fabry-Perot filter was demodulated the detected light intensity. The FBG system was calibrated, and the amplitude of the strain data was validated to account the nonlinealy of the filter. In the experiment, the strain was monitored at a rate of 100 kHz with a noise level of 2 με for modal analysis in low energy impact. Besides, the results of FBGs agreed well with a pertinent numerical model and modal analysis using a laser vibrometer.

Many FBG sensors allow the simultaneous measurement of strain at many locations in a structure. The FBG system provides high precision but inherit a large delay time, and limited acquisition frequency makes it difficult for vibration detection. However, a multichannel FBG sensor system was proposed by Uwe et al. (2010) using a position-sensitive detector for the wavelength interrogation. A theoretical maximum bandwidth of over 300 kHz was achieved by using this approach, which is much higher than other systems. Such a system was tested for high-precision static strain measurement for shape control applications at a low frequency in a test rip (<0.3 μm/m) at 5 Hz and more than 12 kHz for high-frequency dynamic strain measurement. A strain-based modal analysis was performed using four FBGs, which allow to detect the bending modes 1–8 of a cantilever beam at a range of 9.2 to 1449 Hz. They also demonstrated that this system could have a versatile use for a high-precision shape control in a low frequency less than 0.5 Hz as well as in a high frequency over 1000 Hz.

On the other hand, POF-based sensors were also employed to detect the dynamic

strain in many works. Kuang and Cantwell (2003) demonstrated that POF sensors have the ability to monitor the dynamic response of fiber composite beams. The sensors were both surface-bound to a plastic beam or embedded in a carbon-fiber composite, and a series force and free vibration were subjected to it to assess this ability. The results on the natural frequencies of the beam agreed with that of the theoretical values and strain gauge. The impact test experiment also demonstrated that POF sensors can be used to monitor the out-of-plane deflection during the impact event. Those results were validated by employing a laser Doppler velocimeter and piezoelectric load cell.

In 2003, Kuang et al. reported the use of the same POF sensor and Ni-Ti shape memory alloys (SMA) wires as strain monitors of woven carbon fiber epoxy composite cantilever beams subjected to vibration tests. SMA wires were applied to control and modify the damping response of the composite beam. A 10 mm diameter hemispherical steel impactor was used to impact the specimens at 2 to 8 J, and then each sample was tested in a three-point bending with the impact surface in compression in order to obtain residual strength data. POF sensors were used to monitor the damping response of the composite samples with and without impact damage. The damping ratio did not change very much between 2 J and 4 J, suggesting that this sensing system is more suitable for larger impact energies.

An intensity-modulation-based POF sensor was used to measure both static and dynamic strains on a cantilevered beam (Sun and Oyadiji, 2007). The strain change was detected by the transmitted light intensity. The POF sensors were fabricated using three types of housing (silicon rubber tube, rubber tube, and PTFE tube), and their performances were evaluated. For a static test, the results found that the soft material

provided better sensitivity than hard material (PTFE tube); however, the PTEE tube gives a faster response time for a dynamic strain. A strain up to 20 με can be detected by those POF sensors. The ability for vibration detection was also studied in this work.

2.5 Summary

In this chapter, the relative literatures of the TPFS for SHM are reviewed. The backgrounds of POF are described in its historical and optical characteristics, in which the optical loss of POF is mainly discussed. In section 2, the hydration process of cement paste is reviewed. The basic knowledge of the hydration process, the degree of hydration, and the theoretical models are given. In the hydration process of cement, the liberated heat and hydration stress are two important factors for indicating the degree of hydration. Then, the techniques to monitor the hydration process of cement paste are discussed. A conventional technique such as the thermocouple is commonly used to monitor the curing temperature (liberated heat); however, it is a typical local sensor that only provides the temperature measurement at a certain location. Optical-fiber-based curing temperature techniques are reviewed from the use of the FBG, F-P fiber sensor, BOTDR, and intensity-modulation-based POF sensor. The techniques to detect the vibration and crack in a concrete beam are described in the fourth section. In this part, conventional detection techniques and optical-fiber-based techniques are reviewed and compared, respectively. Conventional techniques are electrical based and point sensing and too complex to multiplexing many sensors into one system; however, optical-fiber-based sensing techniques have the predominant advantages, such as small size, low cost, and capability to avoid electromagnetic influence, easy multiplexing.

CHAPTER 3

DEVELOPMENT AND OPTIMIZATION OF THE TPFSs FOR TEMPERATURE SENSING

In the first part of this chapter, a TPFS is developed to monitor the curing temperature of cement paste. The measurement principle of TPFS is analyzed by V-number of leaky ray. The numerical result of TPFS shows that the V-number of leaky ray increases with the temperature. However, the V-number theory cannot sufficiently reflect the difference between the temperature sensitivity and the geometries of tapered fiber. Hence, the ray-tracing theory demonstrates its potential ability to tracing the ray propagation along the tapered region. It can provide the information of how the propagation ray is perturbed by the different geometries of tapered fiber and the ambient refractive index and temperature; therefore, the temperature sensitivity can be optimized from optimization of tapered fiber geometries. Thus, in the second part, a ray tracing theory is employed to optimize the geometries of TPFSs for monitoring the early age curing temperature of cement pastes. A background of ray-tracing theory is described to analyse the light ray guided inside the multimode optical fiber. In general, the guided rays are classified into three different rays, named **Bound rays, Refracting rays,** and **Tunnelling rays**. Tunnelling and refracting rays are called leaky rays and they can be perturbed by the surrounding environment. Based on this property of leaky rays, the tapered fiber is employed to

sense the surrounding temperature when it is embedded into the host specimen like cement paste. Then, a mathematical model of TPFS employing the above ray-tracing theory is constructed and the optimization of the geometries of the TPFS is carried out. In the tapering of fiber, an optical multimode plastic fiber is used due to its typical inheritance properties, such as better signal coupling, larger core radii, higher numerical aperture, and larger thermal-optic coefficient in comparison than that of optical glass fiber. Numerical simulation on the tapering plastic multimode fiber is carried out and the effects of the geometries including taper ratio, taper length, and launch angle of the initial ray, and the surrounding temperature on the performance of TPFS is studied numerically. In the third section, an experimental preparation and experimental setup is described to implement the tapered fiber embedded into the cement paste. The experimental setup described in this section has the ability to stabilize the sensor performance, since the output power stability of light source is a key factor in influencing the stability of TPFS employs intensity modulation technique. On the other hand, an auto-data collection and the date noise removal technique are achieved from this experiment setup also. The experimental results of TPFS are described in the next section, in which two sets of geometries of tapered fibers were used, included the stripped lengths of 2.0 cm, 4.0 cm and 6.0 cm at diameter of 480 μm and the stripped length of 6.0 cm at diameters of 240 μm, 480 μm, and 600 μm. Both the experimental results and numerical results agree well and found that the higher sensitivity of TPFSs achieved by longer tapered length, small taper ratio and also proved that the TPFS has an ability to sense the early-age curing temperature and find the setting time of cement paste. Conclusions are given in the last section.

3.1 Development of TPFSs to monitor the curing temperature of cement paste

At the early age curing of concrete, the tensile strength develops with the age while the tensile stresses are generated due to the changes in volume. Controlling the variables that cause a volume change in concrete can minimize high tensile stress and the possibility of cracking. The volume of concrete begins to change shortly after it is cast and the early age volume changes within 24 hours can affect the tensile stress and the initiation of cracks in hardened concrete. At the early stages, however, the strength of the cement hydration at an increased temperature is reduced compared to those hydrated at room temperature (Bushnell-Watson, 1980, 1990a; Komonen, 2003). For the increased temperature, the initially fast hydration will result in more rapid precipitation of the hydration products during the first hours and days, and will cause a more heterogeneous distribution of the hydration products as the hydrates precipitate around the clinker (Bushnell-Watson, 1990b). For low temperatures, the hydration starts very slowly to allow the dissolved ions to diffuse before the hydrates precipitate and cause a less dense C-S-H (in cement chemistry notation, C=CaO, H=H_2O, S=SiO_2), a more even distribution of hydration products and a lower coarse porosity (Glišić, 2000). Hence, during the curing of cement paste, different temperatures not only induce changes in the morphology of solid phases but also influence the composition of the liquid phase. As cement hydrates, the reaction provides a significant amount of heat. In large elements, this heat is trapped and can induce significant expansion. When thermal changes are superimposed upon auto-genous shrinkage at an early age, cracking can occur. In particular, differential thermal stress can occur due to rapid cooling of massive concrete elements. As such, the hydration process monitoring and control are very

important during the casting of concrete structures.

3.1.1 The temperature sensing principle of TPFS

The tapering of the fiber makes the fiber core exposed to the ambient environment immediately. According to the ray-tracing theory described by Snyder and Love (1983) the Evanescent Wave (EW) only contributed by the leaky rays when the bound rays is hidden by the fiber core. When the incident rays reached the tapered region, some fraction of the bound rays become leaky rays to increase the strength of the EW and the rest bound rays are transmitted to the end of the fiber. In a tapered fiber, the numbers of bound rays are not only governed by its configuration, such as taper length, taper ratio, but also perturbed from the changing of refractive index of the fiber core and ambient environmental conditions. Based on this principle, the detected ray intensity contributed from transmitted bound rays can be modulated by the change of refractive index of the fiber core or the ambient environmental conditions. As such, the temperature sensing principle of tapered fiber can be explained by the detected ray intensity perturbed due to the change of ambient temperature if the refractive index of specimen is kept constant.

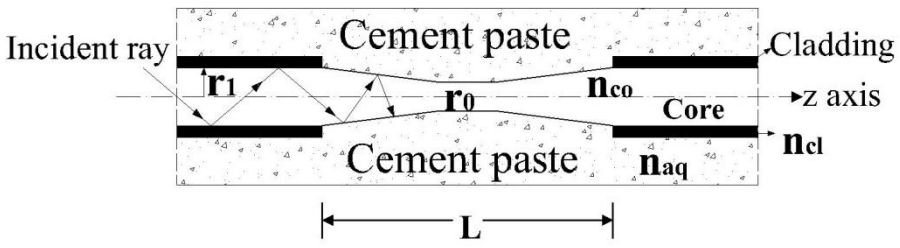

Fig. 3.1: Configuration of tapered fiber for monitoring the hydration process of cement paste.

The configuration of tapered fiber for curing temperature measurement is shown in Fig. 3.1. As shown in this figure, the fiber is tapered from radius of r_0 to r_1 along the length L. The cement paste has a refractive index of 1.73 for the real part and 0.003 for the imaginary part (Cyr et al. 2001). Temperature-caused index change of the plastic optical fiber core equals to $-1.3\times10^{-4}/℃$ (Zhang et al. 2006) and the temperature-induced index change of cement paste are considered insignificant since the refractive index of cement paste is approximated. The radius distribution along the taper is $r_{(z)}$. *V* number is a parameter to describe the number of propagation modes guided by the optic fiber, which is defined as

$$V = \frac{2\pi r_0}{\lambda}\sqrt{n_{co}{}^2 - n_{cl}{}^2} \tag{3.1}$$

where λ is the wavelength of transmitting light, n_{co} and n_{cl} are the refractive indies of fiber core and cladding, respectively. Removal of cladding increased the number of propagation modes in the sensing element while reduction of fiber core decreases the propagation modes. Thus, the *V*-number of tapered fiber can be derived

$$V_{(z)} = \frac{2\pi r_{(z)}}{\lambda}\sqrt{n_{co}{}^2(T) - n_{aq}{}^2(T)} \tag{3.2}$$

$n_{co}(T)$ is the refractive index changed by temperature, where $n_{co}(T) = n_{co} + \Delta n_{co} \times T$, $n_{aq}(T)$ is the refractive index of surrounding medium and functioned as $n_{aq}(T) = n_{aq} + \Delta n_{aq} \times T$, where the Δn_{co} and Δn_{aq} are the temperature-caused index change of fiber core and surrounded medium, T is the surrounded temperature (Bushnell-Watson,1990).

According to the ray-tracing theory described by Bushnell-Watson (1986), the EW only contributed by leaky rays when the bound rays is hidden by the fiber core. When the rays reached the tapered region, some fraction of bound rays becomes the leaky ray to increase the EW. Hence, the number of leaky modes is given by

$$M_{lm}(z) = \frac{V_{(z)}^2}{2}\left(\frac{1}{2\Delta} - 1\right) \tag{3.3}$$

where $\Delta = \frac{n_{co}^2 - n_{cl}^2}{2n_{co}^2}$. Thus, from Eq. (3.3) it can be seen that the guided modes are not only governed by the configuration of tapered fiber, but also can be influenced from the surrounding temperature.

3.1.2 Numerical results of TPFS

The MATLAB program is used for the numerical calculation. The incident light wavelength is 630nm from a laser diode and the multimode plastic fiber with core radius of 0.5mm. The refractive indices of core and cladding are 1.492 and 1.402 respectively. Assume the taper radius distribution is parabolic:

$$r_{(z)} = \frac{4}{L^2} r_0 (1-R)(z - L/2)^2 + Rr_0 \tag{3.4}$$

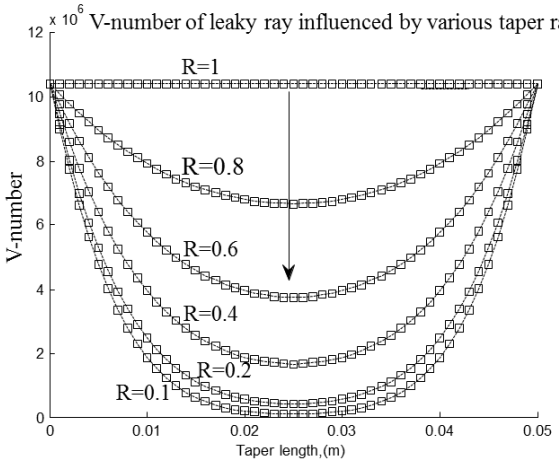

Fig. 3.2: V-number of leaky ray effected by different taper ratio in the taper length of L_0=0.05m.

The results shown in Fig. 3.2 depict the V-number of leaky rays influenced by various taper ratios in the taper length of 0.05m. From the figure, it can be seen that the uniform fiber has the highest number of leaky ray propagation modes 10.15×10^{6}; however, in the taper ratio of 0.1 the value of leaky ray propagation modes reduces to 0.1×10^{6}. Thereby, while the light transmitting from the sensing region to the cladded optical fiber, there is approximately 99% leaky ray propagation modes lost which finally contributes to the strength of EW. In this figure, the number of leaky ray propagation modes guides more for smaller taper ratio which finally achieved higher sensitivity of temperature response.

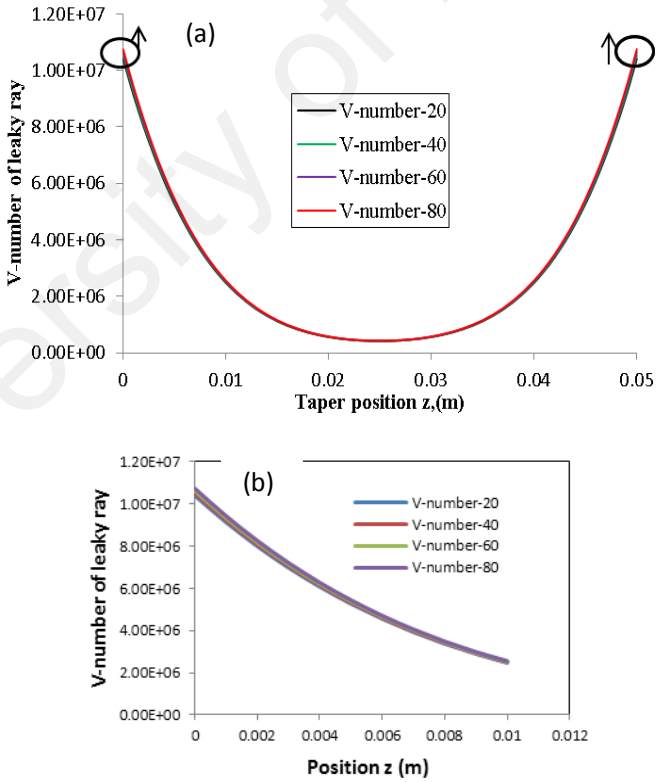

Fig. 3.3: V-number of leaky ray effected by different surrounded temperatures in the taper length of L=0.05m and taper ratio of R=0.2.

The results shown in Fig. 3.3 (a) depict the V-number of leaky rays influenced by various temperatures in the taper length of 0.05m and taper ratio of R=0.2, a zoom-in

view is shown in Fig.3.3 (b). From the figure, it can be seen that the V-number of leaky rays increases with increasing surrounding temperatures. In the taper position of 0 and 0.05m, the highest V-number of leaky ray1.08×10^{7} is obtained compared to that of 1.04×10^{7} for the surrounding temperatures of 80 ℃ and 20 ℃, respectively. The increased V-number of leaky ray will result in a change of sensor output intensity, thus, the output intensity of proposed sensor can be modulated by the surrounding temperatures. From the Fig. 3.3, it can also be observed that the operation of tapering the fiber can enhance the strength of EW. In the taper position of 0.025m, however, the V-number of leaky ray propagation modes is decreased to 0.42×10^{6}. As such, there is approximately 96% of leaky ray lost in the sensing region, which contributes to the strength of EW to increase the sensitivity of the proposed sensor.

3.2 Optimization of the geometries of TPFS

3.2.1 Theoretical background

An optical fiber consists of a core and a cladding surrounding the core as shown in Fig. 3.4. The refractive index of the core n_{co} is higher than that of the cladding n_{cl}. Hence, the light propagation inside the fiber is followed by the total internal reflection which meets the condition at the core-cladding interface as given by $n_{co}\sin(\frac{\pi}{2}-\phi)\geq n_{cl}$. The angle ϕ is related to the incident angle θ by $\sin\theta = n_{co}\sin\phi \leq \sqrt{n_{co}^2 - n_{cl}^2}$ .For the multi-mode fiber, it meets the condition $\frac{2\pi\rho}{\lambda}\sqrt{n_{co}^2 - n_{cl}^2}\geq 1$, where ρ is a linear dimension in the core, e. g. the radius of fiber core, λ is the wavelength of light in free space, n_{co} is the maximum refractive index in the core and n_{cl} is the uniform refractive

index in the cladding. In general, the electromagnetic propagation along the optic fiber can be described exactly by Maxwell's equations. However, it is well known that the classical geometric optics provide an approximate description of light propagation in regions where the refractive index varies only slightly over a distance comparable to the wavelength of light. This is typical of multi-mode optical waveguide used for communication. Thus, the most direct and conceptually simple way to describe the light propagation in multimode fiber is by tracing the rays along the core which is described in this section.

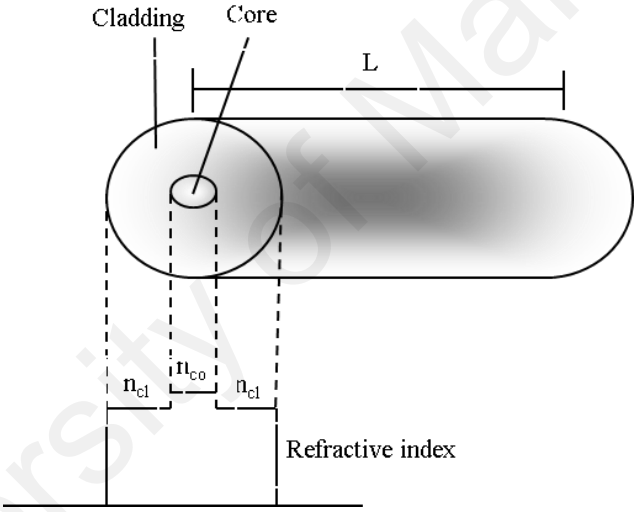

Fig. 3.4: The structure and refractive index distribution of step index optical fiber.

3.2.1.1 Bound rays of Step-index fibers

Reference to the Fig. 3.1 the step index fiber has the refractive index profile defined by Snyder et al. (1974)

$$n(x) = n_{co},\ -\rho<x<\rho;\ n(x) = n_{cl},\ |x|>\rho, \tag{3.5}$$

where the $n_{co}>n_{cl}$ and both of them are constants. To construct the ray paths within the core using ray tracing and Snell's laws, it is assumed that the core is non-absorbent

without loss of power for ray propagation along the fiber.

3.2.1.2 Construction of ray paths

The ray propagation of step index multimode fiber is shown in Fig. 3.5 along the direction of *z* axis. In Fig. 3.5, the ray in point *P* propagation along the fiber makes an angle of θ_z with the fiber axis, it will meet the opposite interface at *Q* as shown. The situation at *Q* is equivalent to incidence at an interface between two half spaces of refractive indices n_{co} and n_{cl} as shown in Fig.3.6. Thus, in terms of complementary angles, the incident ray at *Q* is totally internally reflected if $0 \leq \theta_z < \theta_c$ and is partly reflected and partly refracted if $\theta_c < \theta_z \leq \pi/2$, where θ_c is the complement of critical angle, defined by Rawson et al. (1970)

$$\theta_c = \cos^{-1}\left(\frac{n_{cl}}{n_{co}}\right) = \sin^{-1}\sqrt{1-\frac{n_{cl}^2}{n_{co}^2}} \tag{3.6}$$

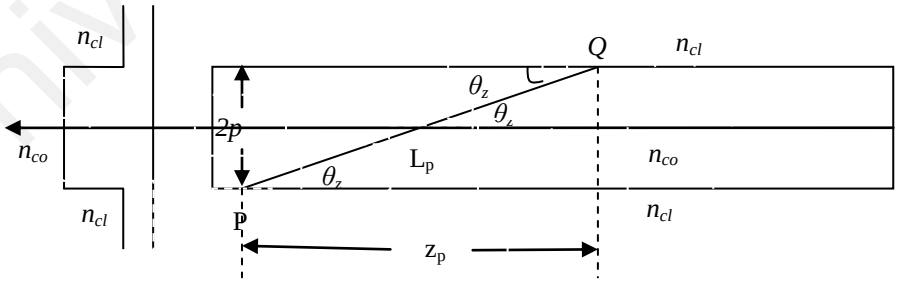

Fig. 3.5: The ray propagation along the fiber core of *z* axis in the step-index fiber.

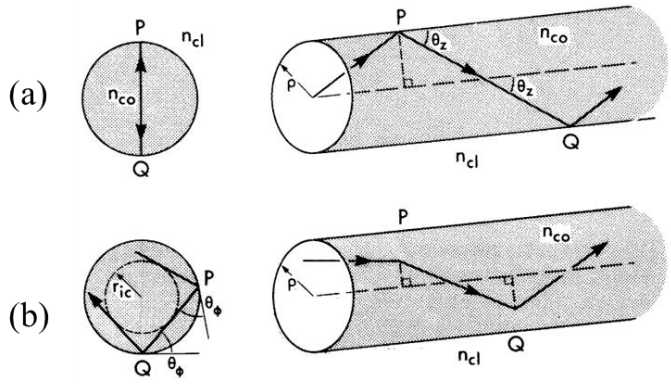

Fig. 3.6: Ray paths within the core of step-index fiber showing (a) the zig-zag path of a meridional ray and (b) the helical path of a skew ray, together with their projections onto the core cross-section (Snyder et al. 1974).

It is useful to distinguish the rays which cross the fiber axis between reflections-known as meridional rays and rays which never cross the fiber axis known as skew rays. It is seen from Fig. 3.6 (a) that meridional rays lie in a plane of width 2ρ through the axis. Skew rays, on the other hand, follow a helical path whose projection onto the cross-section is a regular as shown in Fig. 3.6 (b). The midpoints between successive reflections all touch a cylindrical surface of radius r_{ic}, known as the inner caustic. To specify the trajectory of a skew ray, it is clear from the Fig. 3.6 (b) that in addition to the inclination θ_z to the axial direction, we need second angle to indicate the skew is needed. The angle in the core cross-section between the tangent to the interface and the projection of the ray path is defined as θ_ϕ, as shown in Fig. 3.6 (b) (Snyder et al. 1974). Geometrically, θ_ϕ has the same value at its every reflection. The radius r_{ic} of the inner caustic is given by Ankiewicz et al. (1977); Jackson et al. (1999); Marcatili et al. (1977).

$$r_{ic} = \rho \cos\theta_\phi \tag{3.7}$$

and thus depends only on the skew angle. For meridional rays $\theta_\varphi = \pi / 2$ and $r_{ic} = 0$.

The angles θ_z and θ_ϕ are spherical polar angles correspond to the fiber axial direction, which also shows that the angle α between the incident and reflected rays and the normal. The relation between these three angles is given by Ankiewicz et al. (1977); Jackson et al. (1999); Marcatili et al. (1977).

$$\cos\alpha = \sin\theta_z \sin\theta_\phi \tag{3.8}$$

3.2.1.3 Classification of rays

The rays on the step-index fibers show in Fig.3.7. The rays can be categorized by the value of θ_z, θ_ϕ and α according to Bound rays: $0 \le \theta_z < \theta_c$, Refracting rays: $0 \le \alpha < \alpha_c$, and Tunnelling rays: $\theta_c \le \theta_z \le \pi/2$. Where α is the angle of incident ray and normal and α_c is the critical angle of fiber defined by $\sin\alpha_c = \frac{n_{cl}}{n_{co}} = \cos\theta_c$. Rays which are not bound, i.e. tunnelling rays and refracting rays are known as leaky rays. Since the power of bound ray is totally reflected back into the core at every reflection, the rays can propagate indefinitely without any loss of power. A refracting ray loses a fraction of its power at each reflection and therefore attenuates as it propagates.

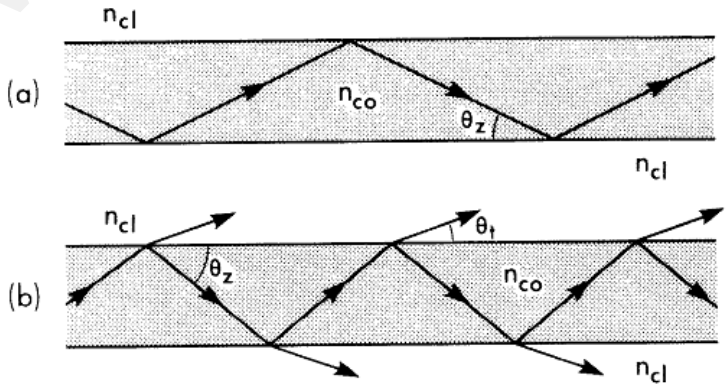

Fig.3.7: Zig-zag paths within the core of a step index fiber for (a) bound rays and (b) refracting rays (Snyder et al. (1974)).

3.2.1.4 Ray invariants

The ray invariant $\bar{\beta}$ is constant along the path and specifies the ray direction at any position in the cross-section and the second ray invariant $\bar{l}$ is related to the skew angle θ_ϕ, accounts for the azimuthally symmetry of the fiber (Rawson et al. 1970). Hence

$$\bar{\beta} = n_{co}\cos\theta_z = n_{cl}\cos\theta_t, \quad \bar{l} = n_{co}\sin\theta_z\cos\theta_\phi \tag{3.9}$$

$$\bar{\beta}^2 + \bar{l}^2 = n_{co}^2\sin^2\alpha \tag{3.10}$$

Therefore, the rays can be classified by the value of $\bar{\beta}$ and subdivision of leak rays into tunnelling and reflecting rays depends on the values of $\bar{l}$ which are given by Snyder et al. (1974) as:

Bound rays: $n_{cl} < \bar{\beta} \le n_{co}$, (3.11)

Refracting rays: $0 \le \bar{\beta}^2 + \bar{l}^2 < n_{cl}^2$, (3.12)

Tunnelling rays: $n_{cl}^2 \le \bar{\beta}^2 + \bar{l}^2 < n_{co}^2$ and $0 \le \bar{\beta} < n_{cl}$. (3.13)

3.2.1.5 Leaky rays

When the fibers are illuminated by a diffused source, both the bound and leaky rays will be excited. Each leaky ray will have radiated away virtually all of its power and the bound rays will carry nearly all the remaining power in the fiber when the rays are propagated into the fiber along a sufficient distance. However, the leaky rays contribute significantly to the total light power in the intermediate region of the fiber (Albertin et al. 1974; Barrel et al. 1979; 1980; Snyder et al. 1976) This section analyzes the intermediate region of leaky rays. In this region, the refracting rays and

tunnelling rays attenuate very fast, but the tunnelling rays may have arbitrarily low attenuation rates and behave almost as bound rays when the fiber parameter V is sufficiently large.

Refracting rays

Within the core of a step-index fiber, the Fresnel coefficient is used to describe the fraction of power lost by rays which undergo refraction at the interface. Thereby, the power attenuation coefficient of refracting rays is as given by Gloge et al. (1975):

$$\gamma = \frac{2\sin^2\theta_z}{\rho\cos\theta_z}\frac{\sqrt{\sin^2\theta_z\sin^2\theta_\phi - \theta_c^2}}{\left\{\sin\theta_z\sin\theta_\phi + \sqrt{\sin^2\theta_z\sin^2\theta_\phi - \theta_c^2}\right\}^2} \tag{3.14}$$

Tunnelling rays

The transmission coefficient T determines the fraction of incident ray power which is conveyed across the evanescent region by tunnelling. The expression for transmission coefficient of tunnelling rays on a weak guiding step-index fiber is given by Barrel et al. (1978) and Love et al. (1979).

$$T = \left|T_f\right|\exp\left\{-2k\int_{\rho}^{r_{rad}}\sqrt{\bar{\beta}^2 + \bar{l}^2\frac{\rho^2}{r^2} - n_{cl}^2}\,dr\right\} \tag{3.15}$$

Where r_{ad} is given in $r_{ad} = \dfrac{\bar{l}\,\rho}{\sqrt{n_{cl}^2 - \bar{\beta}^2}}$, and T_f is the analytic continuation of the classical Fresnel transmission coefficient to angles less than the complementary critical angle θ_c. In terms of ray invariants it is given by Love et al. (1977) and Snyder et al. (1976):

$$\left|T_f\right| = \frac{4}{n_{co}^2 - n_{cl}^2}\sqrt{n_{co}^2 - \bar{l}^2 - \bar{\beta}^2}\sqrt{\bar{l}^2 + \bar{\beta}^2 - n_{cl}^2} \tag{3.16}$$

The factor $\left|T_f\right|$ is accounts for the jump at the interface, and the exponential factor is due to the evanescent field in the region between the interface and the radiation caustic. The transmission coefficient at the closed form is given by.

$$T = \left|T_f\right| \exp\left\{-2k\rho\bar{l}\left[\ln(p + \sqrt{p^2 - 1}) - \sqrt{p^2 - 1}/\, p\right]\right\} \tag{3.17}$$

where the p is defined by $p = \dfrac{\bar{l}}{\sqrt{n_{cl}^2 - \bar{\beta}^2}}$. Only rays whose radiation caustic are very close to the interface are inaccurately described by this expression (Love et al. 1978).

3.2.2 Optimization of the geometries of TPFSs

In this section, the geometrics of tapered fiber are optimized for achievement of high temperature sensitivity. A mathematical model based on ray tracing theory is made and the optimization of the geometries of the proposed sensor is carried out theoretically. Numerical simulation on the tapered multimode plastic fiber is carried out and the effects of the geometries including taper ratio, taper length, and launch angle of the initial ray, and the surrounding temperature on the performance of proposed sensor is studied numerically. Experimental study on the proposed sensor, for which a high strength reactive powder is used, is carried out and the experimental results agree well with the simulation results.

3.2.2.1 Mathematical model of tapered fiber

Three reasonable assumptions are made to analyse the proposed sensor

theoretically. Firstly, ignore the change of ray tracing angles from thermal expansion of the fiber core. Secondly, ignore the change of refractive index of tapered fiber from shrinkage stress during curing of cement paste. When the plastic optical fiber is selected as host specimen to fabricate the tapered fiber, it is equitable to ignore the shrinkage stress effect since the thermo-optic affect dominates the change of refractive index which is around -1.3×10^{-3} for 10 ℃ temperature change. The stress-optic coefficient of plastic optical fiber is $-4.5\times10^{-12}\,Pa^{-1}$ (Szczurowski et al. 2010). It only perturbs the axial refractive index at value of -5.4×10^{-5} where a roughly compressive stress of 1750 psi was measured at early-age by using embedded piezoelectric transducers (Gu et. al. 2006). Thirdly, ignore the humidity affect for the detected power of proposed sensor. It was found that in the ageing test of plastic optical fiber the maximum attenuation decreased around 25% due to water absorption within 24 to 48 hours (Ziemann et. al. 2000). Based on this measurement, the detected power only decreases around 0.28% when a tapered fiber length of 6 cm was embedded.

3.2.2.2 Rays invariants

The sensing principle of the tapering plastic multimode fiber is based on the attenuated total internal reflection spectroscopy. After tapering the fiber, some of the guided light modes do not satisfy the condition of total internal reflection due to the reduction of the fiber core's diameter. The theoretical analysis is described as follows by ignoring the change of ray tracing angles from thermal expansion of the fiber core.

Fig. 3.8 shows the ray propagation inside the core of a tapered fiber. The refractive indices of the core, cladding and surrounding medium are n_{co}, n_{cl} and n_{aq}, respectively.

The ray propagation from taper length 0 to L_o results in the height z decreasing from r_0 to r_1 and the taper ratio defined by $R=r_1/r_0$. $r_{(z)}$ is the radius of distribution of the unclad taper in the propagation direction of z, L_o is the length of the taper. $n_{co}(T)$ is the function of the refractive index changing with temperature, where $n_{co}(T) = n_{co} + \Delta n_{co} \times T$, $n_{aq}(T)$ is the refractive index of the surrounding medium and functions the same as $n_{aq}(T) = n_{aq} + \Delta n_{aq} \times T$, where the Δn_{co} and Δn_{aq} are the temperature-caused index change of the fiber core and surrounding medium, T is the surrounding temperature (Zhang et al. 2006).

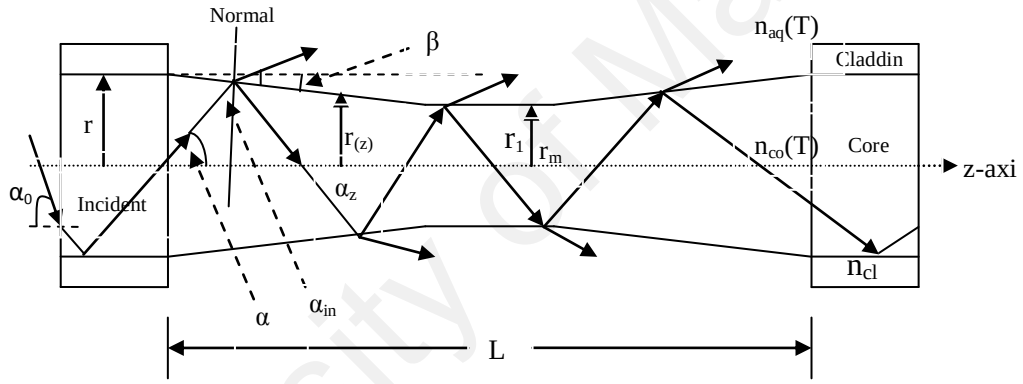

Fig. 3.8: The ray propagation inside the core of tapered fiber.

The ray emitted into the tapered region with an angle of $\alpha = \sin^{-1}\left(\frac{\sin\alpha_0}{n_{co}}\right)$, where the angle α_0 is the ray incident angle on the input face of the fiber, and makes a variant angle α_z with the fiber axis, which changes with the geometry of the tapered fiber and also has a skew angle a_ϕ. The relationship between the α and α_z is given by

$$r_0 \sin(\alpha) = r_{(z)} \sin(\alpha_z) \tag{3.18}$$

The propagation angle α_z can be described according to Equation (3.19)

$$\alpha_z = \sin^{-1}\left[\frac{r_0 \sin\alpha_0}{n_{co}(T) r_{(z)}}\right] \tag{3.19}$$

The α_{in} shown in Fig. 3.8 is the incident ray angle with the normal to the fiber core and surrounding medium interface. It varies from *z*, hence, geometrically the $\alpha_{in}(z)$ can be derived from the triangle in Fig. 3.8, which has the relationship between the taper angle $\beta = \tan^{-1}\left(\frac{2r_0(1-R)}{L_o}\right)$ and ray launched angle α_z,

$$\alpha_{in}(z) = \frac{\pi}{2} - \alpha_z + \beta \tag{3.20}$$

Three direction angles α_{in}, α_z, and a_ϕ are related by $\cos\alpha_{in} = \sin\alpha_z \sin\alpha_\phi$, which results in the skew angle given by Equation (3.21),

$$\alpha_\phi(\alpha_z, z) = \sin^{-1}\left(\frac{n_{co}(T) r_{(z)} \sin\left\{\sin^{-1}\left[\frac{r_0 \sin\alpha_0}{n_{co}(T) r_{(z)}}\right] - \tan^{-1}\left[\frac{2r_0(1-R)}{L_o}\right]\right\}}{r_0 \sin\alpha_0}\right) \tag{3.21}$$

Thus, the ray invariants along the taper portion are governed by Equations (3.22), (3.23), and (3.24) (Snyder et al. 1974)

$$\bar{\beta}(z) = n_{co}(T)\cos\alpha_z = \frac{1}{r_{(z)}}\sqrt{n_{co}^2(T) r_{(z)}^2 - r_0^2 \sin^2\alpha_0} \tag{3.22}$$

$$\bar{l}(z) = n_{co}(T)\sin(\alpha_z)\cos(\alpha_\phi)$$

$$= \frac{1}{r_{(z)}}\sqrt{r_0^2 \sin^2\alpha_0 - \left[n_{co}(T) r_{(z)} \sin\left(\sin^{-1}\left(\frac{r_0 \sin\alpha_0}{n_{co}(T) r_{(z)}}\right) - \tan^{-1}\left(\frac{2r_0(1-R)}{L_o}\right)\right)\right]^2} \tag{3.23}$$

$$\bar{\beta}^2(z)+\bar{l}^2(z)=n_{co}^2(T)\sin^2\alpha_{in}=n_{co}^2(T)\cos^2\left(\sin^{-1}\left(\frac{r_0\sin\alpha_0}{n_{co}(T)r_{(z)}}\right)-\tan^{-1}\left(\frac{2r_0(1-R)}{L_o}\right)\right) \quad (3.24)$$

3.2.2.3 Power transmission coefficients

In most of the literature (Ahmad et al. 2005; Guo et al. 2003; Sun et al. 2008), the theoretical analysis of light-waves guided by multimode fibers is based on the assumption that the fiber is a spatial steady state. This means that the fiber is non-absorbing, which results in the bound rays propagating along the fiber without a loss of power, and is long enough to cause no tunnelling ray or refractive ray effects. Actually, the power attenuation in multimode fiber is strongly related to the tunnelling rays, since the bound ray losses along the non-absorbing fiber and the refracting ray can be ignored at a propagation distance $z = 100r_0$ (Pask et al. 1974). Hence, the refracting ray does not take into the account the leaky ray, since it attenuates quickly when leaving the light source. The power transmission coefficient of the tunnelling ray is defined by

$$T_{tr}=\left|T_f\right|\exp\left(-2kr_{(z)}\bar{l}\left(\ln\left(p+(p^2-1)^{1/2}\right)-(p^2-1)^{1/2}/p\right)\right) \quad (3.25)$$

where $\left|T_f\right|=\frac{4}{n_{co}^2-n_{aq}^2}\left(n_{co}^2-\bar{\beta}^2-\bar{l}^2\right)^{1/2}\left(\bar{\beta}^2+\bar{l}^2-n_{aq}^2\right)^{1/2}$,

$p=\frac{\bar{l}}{\left(n_{aq}^2-\bar{\beta}^2\right)^{1/2}}$, $k=\frac{2\pi}{\lambda}$ is the free space wave number, and λ is the light wavelength at free space.

3.2.2.4 Leaky ray power

The leaky ray power distribution function $F(\bar{\beta},\bar{l})$ is only dependent on the ray path along the fiber core; hence, the distribution functions of the tunnelling ray can be given as

$$F(\bar{\beta},\bar{l}) = \frac{8\pi r_{(z)}^2 I_0 \bar{\beta}\left(n_{co}^2 - \bar{\beta}^2 - \bar{l}^2\right)^{1/2}}{n_{co}^2 - \bar{\beta}^2} \tag{3.26}$$

where I_0 is the intensity of the laser output and is normalized to 1 watt in this paper. Based on the criteria of categorized rays in Snyder and Love (1983), the tunnelling ray power at the distance *z* can be determined by the following Equation (3.27),

$$P_{tr}(z) = \int_0^{n_{aq}(T)} d\bar{\beta} \int_{\left(n_{aq}^2(T)-\bar{\beta}^2\right)^{1/2}}^{\left(n_{co}^2(T)-\bar{\beta}^2\right)^{1/2}} F(\bar{\beta},\bar{l}) \exp\left(-\gamma_{tr}(\bar{\beta},\bar{l})z\right) d\bar{l} \tag{3.27}$$

where $\gamma_{tr}(\bar{\beta},\bar{l}) = \frac{T_{tr}}{z_p}$, and $z_p = 2r_{(z)}\frac{\sin\alpha_\phi}{\tan\alpha_z} = 2r_{(z)}\bar{\beta}\frac{\left(n_{co}^2 - \bar{\beta}^2 - \bar{l}^2\right)^{1/2}}{n_{co}^2 - \bar{\beta}^2}$ is the ray half-period.

The theoretical analysis in Equation (3.27) shows that the power intensity is functioned by temperature *T*, taper geometry $r_{(z)}$, initial launch angle α_0, as well as the refractive index of the surrounding medium n_{aq}.

3.2.3 Numerical results and discussions

In the numerical simulation and experimental implementation, the step-index plastic multi-mode fiber is selected as the sensing element. Since the thermal-optic coefficient of the plastic fiber is one order of magnitude higher than that of glass fiber, which induces the refractive index to vary more rapidly with a change of temperature.

The numerical simulation is carried out with MATLAB. The incident light wavelength is 594nm from a laser diode and the multimode plastic fiber with a core diameter of 0.5mm; the 1.492 and 1.402 are the refractive indices of the core and cladding, respectively. The cement paste has a refractive index of 1.73 for the real part and 0.003 for the imaginary part (Cyr et al. 2001). Temperature-caused index change of the fiber core Δn_{co} equals to-1.3×10^{-4}/℃ (Zhang et al. 2006), and the taper radius distribution is assumed to be parabolic (Ahmad et al. 2005) $r_{(z)} = r_0\left(1+\frac{z}{L_0}(\frac{r_m^2}{r_0^2}-1)\right)^{1/2}$.

3.2.3.1 Effect of taper length L_o and taper ratio R

For a given length of unclad fiber, the EW strength and sensitivity are strongly dependent on the number of ray reflections per unit length. Fiber tapering is a way of exposing the evanescent field to the surrounding medium, as well as increasing the evanescent field magnitude (Ahmad and Hench, 2005). Therefore, the tunnelling ray power effect from the taper ratios and taper lengths are analysed and shown in Fig. 3.9 & 3.10. In Fig. 3.9, the curves show that the power of the tunnelling ray is influenced by different taper ratios along the taper position *z* in the taper length of 0.1m. The negative values represent the contribution of the tunnelling ray on the EW. From Fig. 3.9 & 3.10, it can be found that the tunnelling ray power decreases from 4.115×10^{-6} w to 0.05×10^{-6} w when a fiber is tapered from uniform to a ratio of 0.1. This means that the tunnelling ray power of 4.11×10^{-6} w is contributed to the EW, which results in the achievement of higher sensitivity. It is clear that the higher EW can be achieved by a smaller taper ratio since the uniform fiber has the lowest EW. The 3-D graph shown in Fig. 3.10 demonstrates the combination effect of the taper ratios and taper lengths. It can be seen that the tunnelling ray power along each tapered fiber has the same

distribution for different taper lengths. For different taper lengths, the highest tunnelling ray powers are produced by the same taper ratio of 0.1. From the contribution of EW, hence, the higher sensitivity of tapered fiber can be achieved from a longer taper length and lower taper ratio.

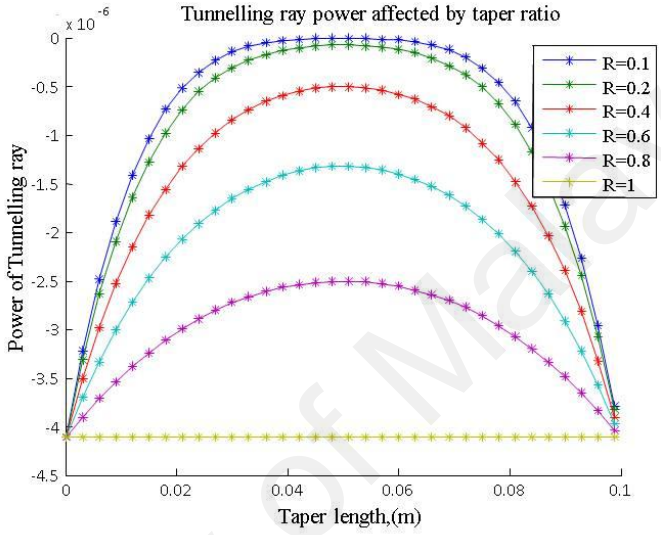

Fig. 3.9: Tunnelling ray power influenced by different taper ratios along the taper position z in the length of L_o=0.1m.

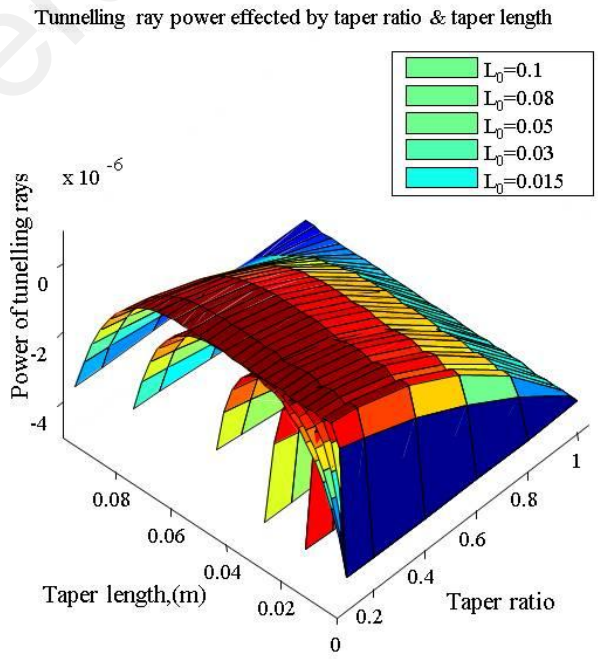

Fig. 3.10: 3-D view of tunnelling ray power effect from taper ratio and taper length.

3.2.3.2 Effect of initial ray launch angle α_0

A tilted initial ray launch condition can be used to excite the leaky ray when the laser light spot is much smaller than the diameter of the fiber. The launched ray reflected and refracted along the fiber is dependent on the angle of incidence, refractive indices of the core and the surrounding medium. When the incidence ray angle is smaller than the critical angle, the ray is almost totally reflected into the core and a small fraction of the ray becomes the EW in the surrounding medium. As shown in Fig. 3.11, the tunnelling ray is only excited in the radian angle range of 0.01 (-0.01) to 0.1 (-0.1) rad. In this range, the tunnelling ray power decreases with the increase of the launch angle of the initial ray. The highest tunnelling ray power is evoked from the launch angle of 0.01 (-0.01) rad of the initial ray, and in the range of 0 to 0.01 (-0.01) rad only the bound ray is excited.

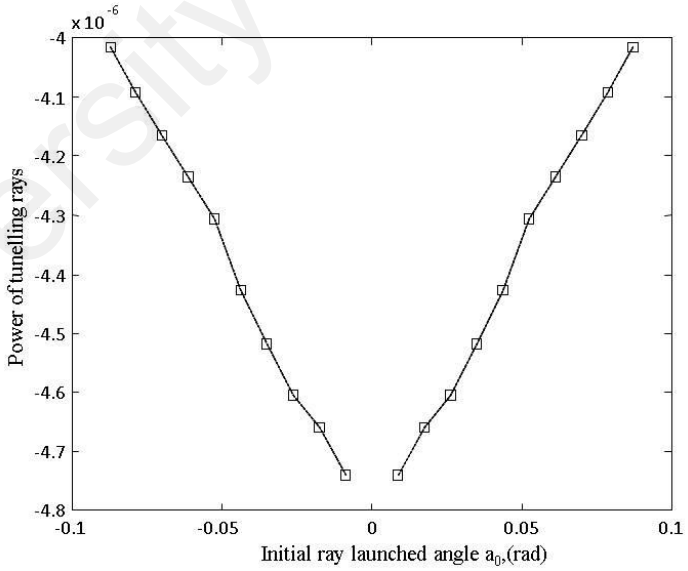

Fig. 3.11: The tunnelling ray power excited by various initial ray launched angles α_0.

3.2.3.3 Effect of surrounding temperature T

The proposed sensor is modulated by the output intensity, which varies with the

change in the surrounding temperature. The leaky ray induced by the tapering of the fiber will be compensated dynamically by the thermal effect, which finally causes the output intensity modulated by the detected temperature (Remouche, 2007). Fig. 3.12 shows the tunnelling ray power evoked by the different initial ray launched angles and surrounding temperatures. As shown in Fig. 3.12, the power of the tunnelling ray decreases with the increase in the temperature. From the curves, it can also be seen that in various surrounding temperatures the biggest difference of the tunnelling ray powers occurs when initial ray launches from the angle of 0.01 rad. Thus, the highest sensitivity can be obtained from this angle. The results illustrated in Fig. 3.13 are the corresponding 3-D view of the tunnelling ray power influenced by the combination of the different launch angles of the initial ray and the temperatures. From this figure it can be observed that the tunnelling ray power has a large variation when the initial launch angle of the initial ray varies from -0.05 to 0.05 rad.

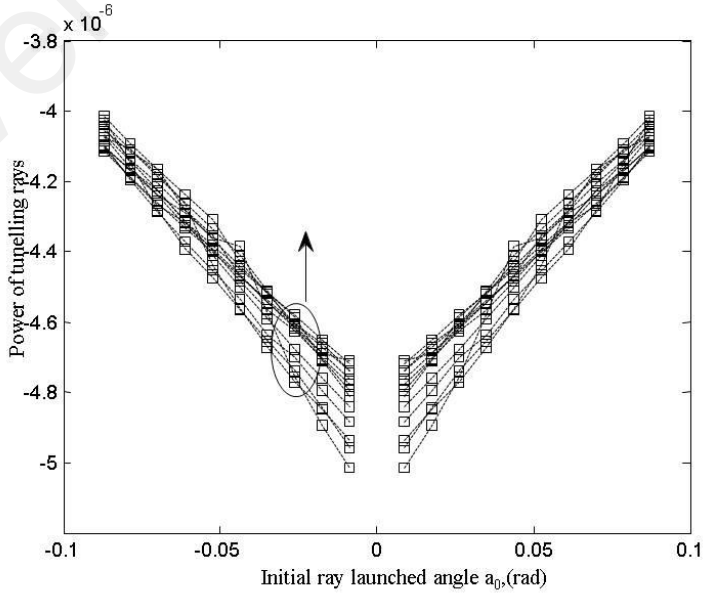

Fig. 3.12: The power of tunnelling ray affected by initial ray launched angles and temperatures (taper length L_o=0.05m, taper ratio R=0.1).

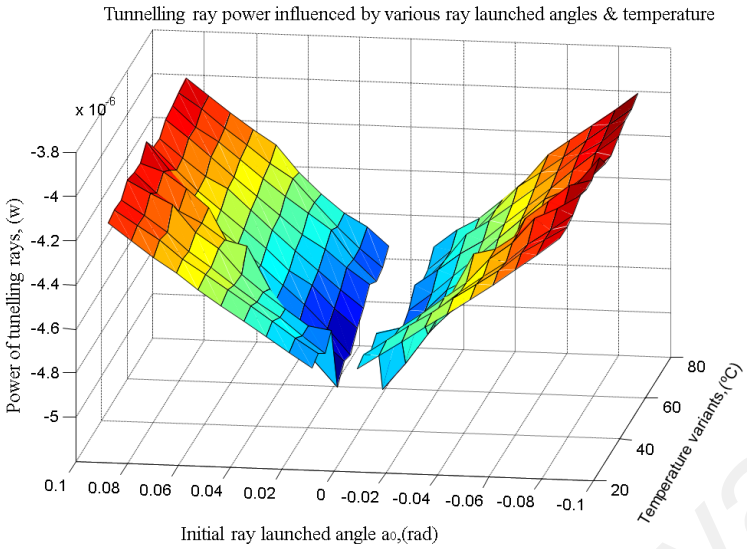

Fig. 3.13: 3-D view the power of tunnelling ray evoked by various ray launched angles and surrounding temperatures.

3.3 Experimental study

3.3.1 Fabrication of sensor probe

The POF was purchased from Mitsubishi with fiber diameter of 1mm, core diameter of 980μm, refractive indices of 1.492 and 1.402 for the core and cladding, respectively. The fiber core is made of acrylic polymer PMMA and is sheathed with a special thin layer of fluorine polymer (cladding) to reduce the refractive index than that of fiber core. To taper the fiber, acetone solution was applied to the optical fiber by using cotton buds. Some contents of plastic fiber were dissolved by the applied acetone to form a layer of milky white material. Then, the distilled water was used to neutralize the reaction between the fiber and acetone. The milky white surface was carefully removed by using sandpaper with grits size of 320. This process was repeated until certain of tapering length and diameter was formed. Finally, the tapered optical fiber was cleaned by using the 2-propanol. By using this process, it is easy to control the geometrical structure of tapered fiber since the reaction of acetone and plastic fiber is

uniformed in the performed region. The fiber tip is cut by a shears and polished by sandpaper carefully to make sure a flat facet is formed.

A comparative photograph of tapered fiber and uniform fiber was taken using optical microscopy, as shown in Fig.3.14 (a). Two sets of tapered fibers have been carefully fabricated with the stripped lengths of 2.0 cm, 4.0 cm and 6.0 cm at diameter of 480 μm and the stripped length of 6.0 cm at diameters of 240 μm, 480 μm, and 600 μm.

3.3.2 Experimental preparation and setup

Prior to pouring the cement paste into the mould the tapered fiber and type T thermocouple are careful fastened on a steel wire as shown in Fig. 3.14 (d). The fastened TPFS is well attached on a steel wire to avoid the effect of micro-bending and strain in the sensor. The steel wire was inserted parallel through the centre of the mould, as shown in Fig. 3.14 (b). The head of the thermocouple is located as close as but not touch with the center position of tapered fiber to make sure the same temperature environment is surrounded in both sensors. The size of the mould was 75×75×200 mm and a plastic sheet was used to cover the mould to prevent water evaporation after the pouring of the cement. The cement used was GP Portland cement compliant with AS3972. The specimen of cement paste (Fig. 3.14 (c)) had a mix proportion by weight of 340, 487, and 75 for the cement, sand and water, respectively. To ensure the accuracy of the experiment, we have carefully prepared all of the experiments under the following recipe. The room temperature was kept at 25 ℃. The materials cement, sand and water were stored at room temperature of 25 ℃ for 1 day. They were mixed in a

container for 2 minutes and poured into the mould slowly to prevent bending of the steel wire. The mould was vibrated for 15 seconds by hand and the data recording/monitoring system was started immediately.

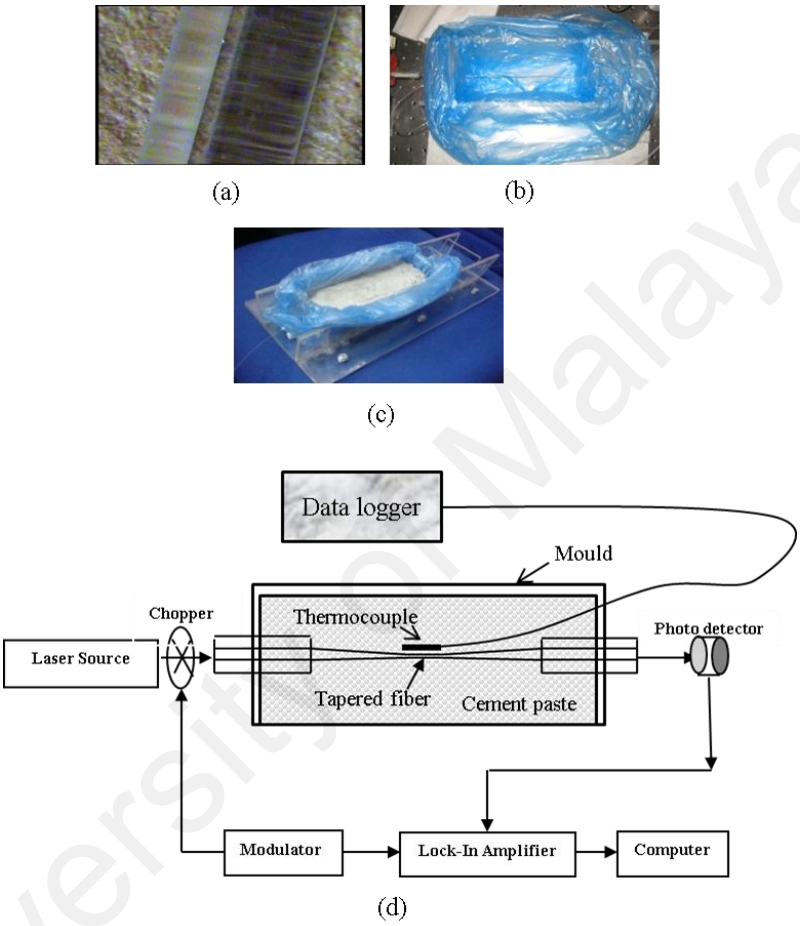

Fig. 3.14: Experimental preparation and setup for the proposed monitoring approach.

As shown in Fig. 3.14 (d), the experimental setup consists of a He-Ne laser source with a wavelength of 594nm (average output power is 3.0mW with the long-term power drift ±2% per hours, with beam diameter and divergence of 0.75mm and 0.92mRads) which coupling the light into the tapered plastic fiber. An external chopper modulated the light with a frequency of 200Hz before launching into the tapered plastic fiber. The tapered plastic fiber was placed in the centre of mould. A photo-detector was located at the end of the fiber to convert the received power into voltage (mV). A model SR-510

lock-in amplifier was connected with the chopper and photo-detector. It plays the function of the experiment data-acquisition system, matches the phase between the transmitting light and receiving light, and removes the noise generated by the laser source, photo-detector and amplifier (Yang et al. 2010). The sensitivity of lock-in amplifier and the data-acquisition system is set as 10μV and 6 points per minute, respectively. A TDS 530 data logger is used to collect the data from the thermocouple. The data logger is set for acquisition of 3 points at one minute interval.

3.3.3 Experimental results

The measurement of the early-age curing temperature of the cement paste at the first 24 hours after casting is shown in Fig. 3.15. The temperature of the air was recorded before the specimen was poured into the mould. Fig. 3.15 shows that the normalized output power suddenly decreased from 1 to a small value (the small figures shown inside of Fig. 3.15 (a) & (b)) when the specimen was poured into the mould. This is because the sensor was initially surrounded by air then changed to the cement paste, which has different refractive indices, which caused the change of output power. The measurement results of thermocouple are also presented for the purpose of comparison and calibration with the proposed sensors. As shown in Fig. 3.15 (a) & (b), the curves of the thermocouple and proposed sensors $S_{1\text{-}5}$ agree well with each other, if the curve of the thermocouple is flipped down. It was found that all of curves of proposed sensors can precisely reflect the early-age curing temperature change as the curing progresses. A closer comparison is shown in Fig. 3.16(a), in which the data are presented for the thermocouple and tapered fibre sensor S4 over a time period of 0 to 0.72 h. As shown in

Fig. 3.16(a), the curves of the thermocouple and proposed optimised sensor agree well with each other if one flips down the curve of the thermocouple. From Fig.3.16(a), it is easy to calibrate the temperature sensitivity of the tapered fibre sensor, which is shown in Fig. 3.16(b). From Fig. 3.16(b), it can be seen that the tapered fibre sensor S4 has a temperature sensitivity of 0.0178 mV/℃, and the coefficient of determination, R^2, is 0.9983. This coefficient indicates that the two curves in Figure 8(a) closely overlap.

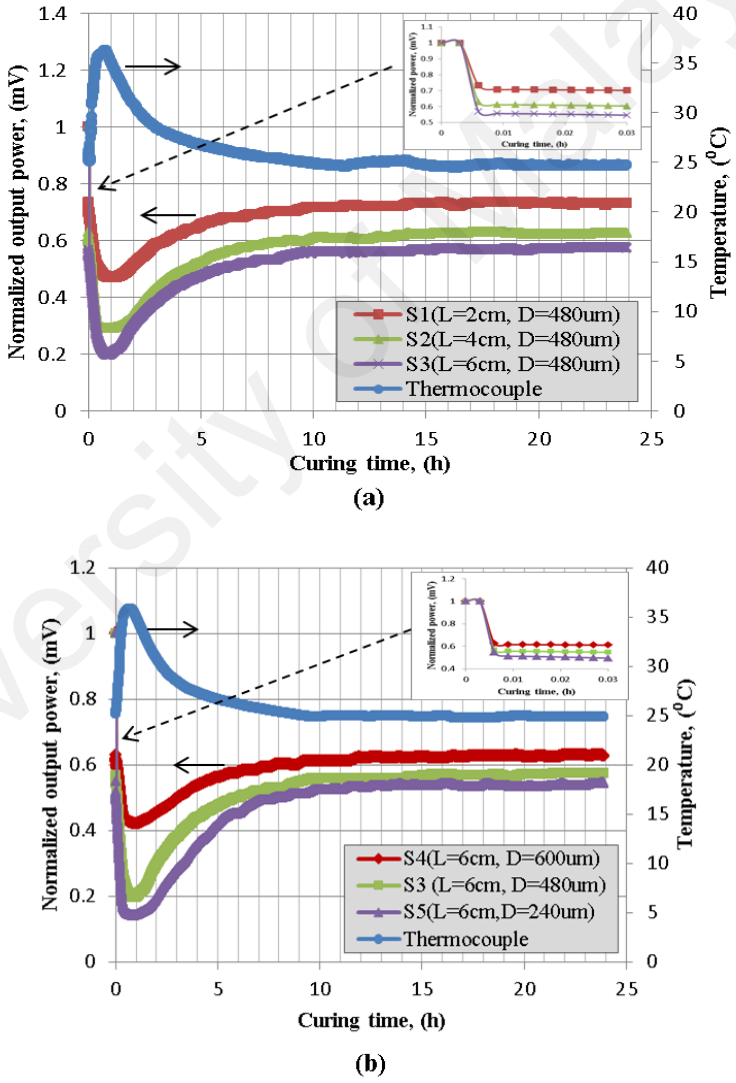

Fig. 3.15: Experiment results of the proposed monitoring approach.

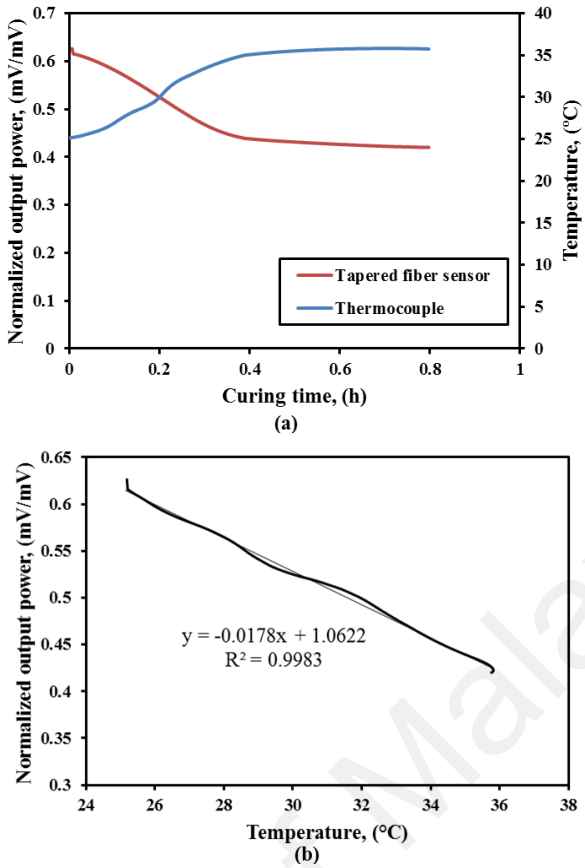

Fig.3.16: Comparison and calibration of tapered fibre sensor S4 using thermocouple measurements.

The resolutions are determined when the sensor system has a measurement sensitivity of 10μV. In Table 3.1, by comparing the sensors of S_{1-3} it was found that the sensitivity of these sensors increased with the taper length increasing for the same taper ratio. The higher sensitivity also gained from the sensor with smaller taper ratio if compared to the sensors of S_{3-5}. From Table 3.1, it can also be found that the highest sensitivity of 0.035 mV/℃ is obtained from the sensors S_5 which has the longest taper length of 6cm and the smallest taper ratio of 0.24. The higher resolution of proposed sensor is obtained from the sensor with higher sensitivity. In the proposed sensor system, the stability of sensor is strongly dominated by the stability of laser source which has the long-term power drift ±2% per hours.

Table 3.1: Summary of the sensitivity and resolution for the proposed sensors (with different tapered structure)

Sensor type (L=cm, D=μm)	Sensitivity, (mV/°C)	Resolution (±°C)
$S_1(2,480)$	0.023	0.43
$S_2(4,480)$	0.028	0.36
$S_3(6,480)$	0.031	0.32
$S_4(6,600)$	0.018	0.57
$S_5(6,240)$	0.035	0.28

From one of curve S_1 in Fig. 3.15 (a), it can be observed that the temperature of cement paste increases as reflected from initial normalized output power of 0.733mV (25 ℃) to a recorded minimum value of normalized output power of 0.465mV (36.8 ℃) after the first 0.72h and increases immediately from there due to the absorption of water during the hydration of cement. Hence, the starting point can be referred to as the initial setting time of the specimen. Furthermore, the hydration of the cement is an exothermic reaction, which releases heat and results in the increase of the temperature of the specimen. The increment of the temperature is observed and reaches its peak at about 0.72 hours. This time is treated as the final setting time of the specimen. After that, the increases in the temperature of the cement paste slow down and became almost stable at 10 hours.

3.4 Summary

In this chapter, a TPFS is developed to sense the curing temperature of cement paste. A V-number theory is employed in the first section to describe the temperature sensing principle. In the second section, the geometries of TPFS are optimized by

using a ray-tracing theory to achieve the higher temperature sensitivity. A background theory on the multimode optical fiber waveguide is described firstly. The mathematical model is employed to optimize the configuration of the tapered fiber, such as, taper length, taper ratio, and the launch angle of the initial ray. The numerical results show that the sensitivity of the proposed sensor is heavily governed from the strength of EW, since the strength of the EW is mainly contributed by the power of the tunnelling ray. Higher sensitivity of the proposed sensor can be achieved by combining a longer taper length and lower taper ratio with the initial ray launch angle of 0.01 rad. The experimental setup is illustrated in the third section. The experiment measurement system using a He-Ne laser, a silicon photo-detector, and a lock-in amplifier is proposed. An accuracy measurement and an auto-data collection are achieved by using this system. The experimental result is described in the last section. The experimental result demonstrates that the proposed sensor has the ability to find the setting time of cement paste since the setting process is accompanied by the temperature change of the cement paste.

CHAPTER 4

THE MONITORING OF EARLY-AGE HYDATION PROCESS OF CEMENT PASTE USING FBG AND TAPERED PLASTIC FIBER SENSORS

In this chapter, the FBG and TPFS were used as sensing element to study the early-age hydration process of cement paste. The FBG is inscribed by a Continuous Wave (CW) 244nm argon ion laser in the photosensitivity fiber. The fabricated FBG is calibrated from room temperature to 105 ℃. In this temperature range, the FBG is found to be in good conditions for both the sensitivity and linearity which around 9pm/ ℃ and 99.9%, respectively. The experimental results show that the FBG is a good alternative to sense the liberated heat when the calibrated FBG is embedded into the cement material. A high reactive power was mixed as specimen, in which a tapered optical fiber sensor was embedded to measure the liberated heat (temperature). The sensor characteristics were determined and calibrated by an embedded thermocouple, which had a sensitivity of 0.0293mV/ ℃, resolution of ±0.34 ℃, and stability of long-term power drift of ±2% per hour. The experimental studies were carried out for the host specimen with different sizes, various water/cement (w/c) ratios, as well as different ambient temperatures. From the experimental results, the curing temperature and setting time were determined by monitoring the curing temperature curves as the curing progressed. The curing temperature rose with increasing mould sizes, decreasing w/c

ratio, and increasing ambient temperature. The setting time could be shortened by a smaller size of specimen, lower w/c ratio, and higher ambient temperature.

4.1 FBG temperature sensing

4.1.1 FBG temperature sensing principle

The basic principle of operation of an FBG-based sensor system lies in the monitoring of the shift in wavelength of the returned "Bragg" signal, as a function of the measured (e.g., strain, temperature). The Bragg wavelength, λ_B, is related to the effective refractive index of the material, n, and the grating pitch, Λ

$$\lambda_B = 2n\Lambda \tag{4.1}$$

A narrow spectral component centered at the Bragg wavelength λ_B is reflected by a FBG, when the light from a broadband light source is injected into the fiber. In the application of temperature sensing, the thermal response of FBG is arisen due to the inherent thermal expansion of the fiber material and the temperature dependence of the refractive index. Thus, the shift in resonance wavelength λ_B with temperature can be expressed according to Escalante-Garcıa (2001) as:

$$\Delta\lambda_B = 2n\Lambda(\alpha + (dn/dT)\Delta T/n) \tag{4.2}$$

where α is the thermal expansion coefficient of fiber material, ΔT is the temperature change, dn/dT is the thermal optic coefficient of fiber material.

From Eq. (4.2), the resonance wavelength is modulated by the changing of temperature, and the measurement temperature can be obtained by

$$T_m = T + \Delta\lambda_B / S \tag{4.3}$$

where T_m is the measurement temperature, T is the initial start temperature, S is the temperature-wavelength sensitivity of FBG, it needs calibrated before FBG used. However, care must be paid to the cross-sensing of FBG in the temperature and strain due to the sensing principle of FBG is monitored the change of grating period. Thus, the experiment should be designed carefully to avoid the strain effect.

4.1.2 Experimental works of FBG sensing

4.1.2.1 FBG fabrication and calibration

A configuration of the FBG fabrication set up is shown in Fig. 4.1. In this setup, an Amplified Spontaneous Emission (ASE) is used as broadband light source (Bushnell-Watson, 1986; Komonen, 2003; Price, 1951) A 244nm light beam is emitted from an argon ion laser and then reflected by a mirror, expanded with two circular lenses, focused by a cylindrical lens and passed through a phase mask (with pitch 1026.8nm) before being exposed to light on a bared photosensitivity fiber (bared fiber means stripped the protection polymer coating, because the UV light cannot pass this type of protection layer). After the light passed through the phase mask, three interfering beams are generated close to the fiber as shown in Fig. 4.2. In this figure, the good condition of phase mask should generates the zero order beam power as low as possible in order to achieve higher interference beams power in both +1 order and -1 order. The phase mask is placed just alongside the fiber with its mask pattern perpendicular to the fiber and the laser. The fiber is placed in near contact with the fine corrugations of the phase mask before writing. Care must be taken to ensure that in the alignment process

the fiber does not come into contact with the phase mask otherwise the phase mask can be damaged in this way. In their experimental, the FBGs are inscribed in single mode high-germania boron co-doped fibers. One of the fabricated FBG is shown in Fig. 4.3(a). The FBG spectra are monitoring in both reflection and transmission in-situ by using Optical Spectrum Analyzer (OSA) (Bushnell-Watson, 1990; Glišić, 2000; Okabe, 2002). The typical reflective and transmission spectrums are shown in Fig. 4.3(a) & (b), respectively.

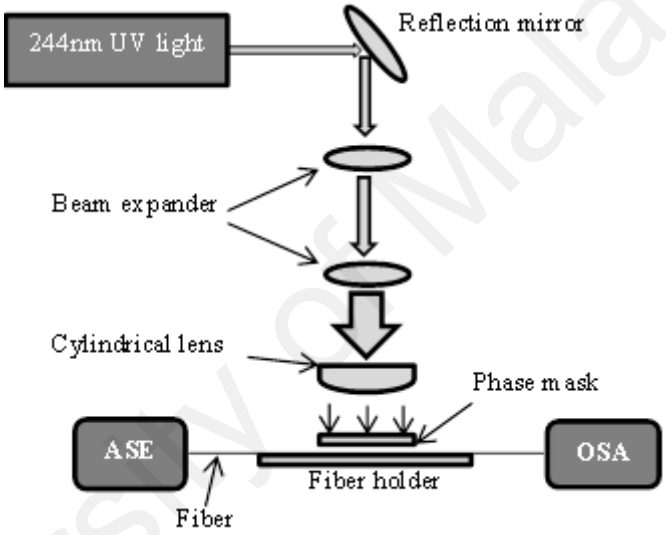

Fig. 4.1: FBG fabricated by using phase mask approach.

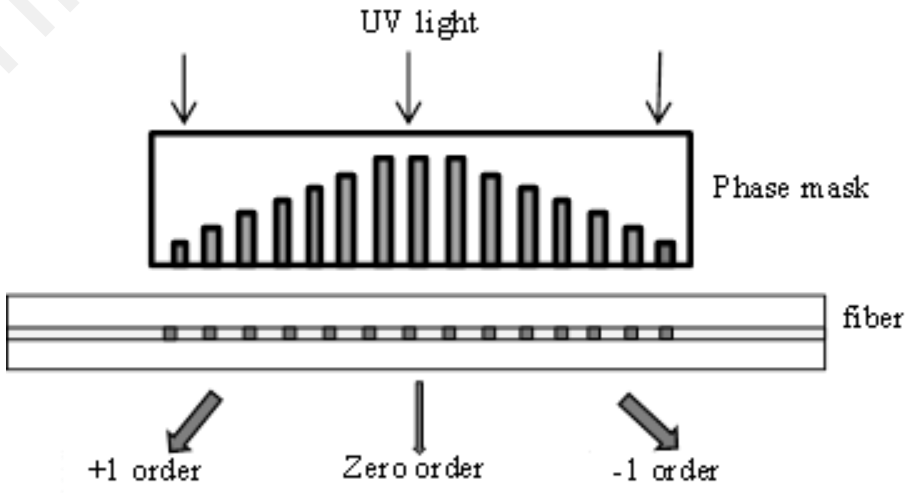

Fig. 4.2: The interfering beams generated by phase mask.

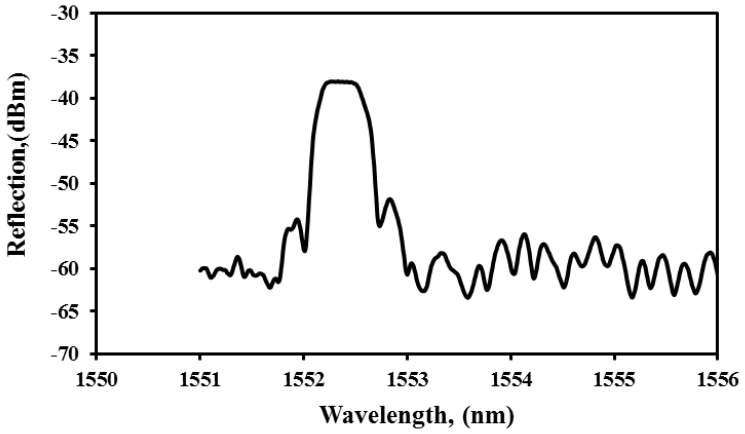

(a)

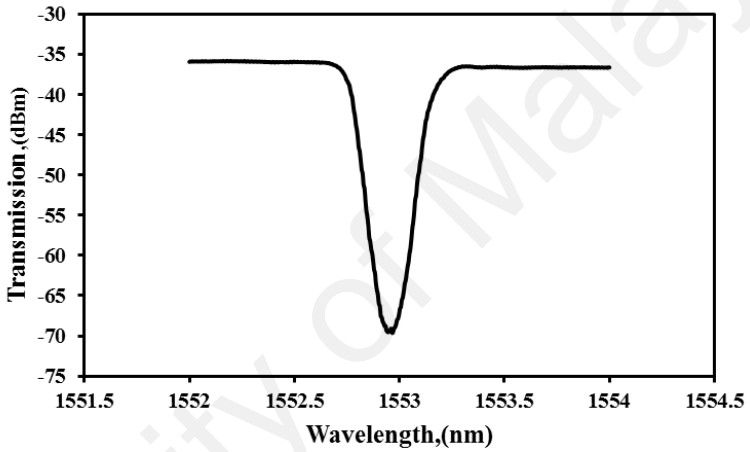

(b)

Fig. 4.3: (a) A typical reflective spectrum of FBG; (b): A typical transmission spectrum of FBG.

4.1.2.2 Sensor temperature-wavelength calibration

Before the FBG is embedded into the cement paste it is better to calibrate the wavelength shift with the change of temperature. A furnace with the temperature resolution of ±0.5 ℃ is used and the climbing temperature step is set to 1 ℃/min. The wavelength shift data is recorded by the temperature increase and decrease at every 10 ℃. When the temperature is reached at each increase/decrease of 10 ℃ points, the

furnace will be held at this point around 5mins to stabilize the temperature and FBG response. The FBG temperature-wavelength calibration result is shown in Fig. 4.4. From this figure, it can be observed that both the calibration curves show good linearity and sensitivity and agree with each other. A sensitivity of 9pm/℃ is founded for both increase/decrease temperatures. From these sensitivities data, a temperature response of gratings can be obtained by capturing the wavelength shift information when the FBG is used in the thermal environment.

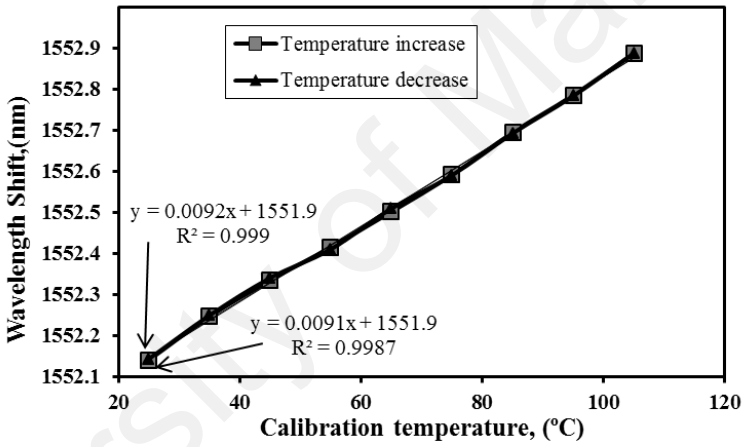

Fig. 4.4: FBG temperature-wavelength calibration figure.

4.1.2.3 Experiment procedures and setup

Prior to pouring the cement paste into the mould the fiber is fastened on a steel wire to avoid the effect of micro-bending and the sensing tip is inserted into a glass tube to protect it and avoid the effect of strain. The glass tube has the inner and outer diameter of 200um and 250um, respectively. The glass tube fastens in the steel wire also. The steel wire is inserted parallel through the centre of the mould as shown in Fig. 4.5 (b). The size of the mould is 75×75×200 mm and a plastic sheet is used to cover the mould

to prevent water evaporation after the pouring of the cement. The cement used is GP Portland cement compliant with AS3972. The specimen of cement paste (Fig. 4.5(c)) has the mix proportion by volume of 800 ml, 500ml, and 275 ml for the cement, sand and water, respectively. They are mixed in a container for 2 minutes and poured into the mould slowly to prevent bending of the steel wire. The mould was vibrated for 15 seconds by hand and data recording/monitoring system was started immediately (Okabe, 2002). During the experiment, the room temperature was kept at 25 ℃. The experiment setup is shown in Fig. 4.5(c). In this figure, the broadband light is emitted from an ASE source, passed through an optical circulator and then reached the FBG sensing element. Part of light is reflected by the grating to form a resonance peak. This resonance peak is feedback and channelled by the optical circulator again and detected, recorded by an OSA.

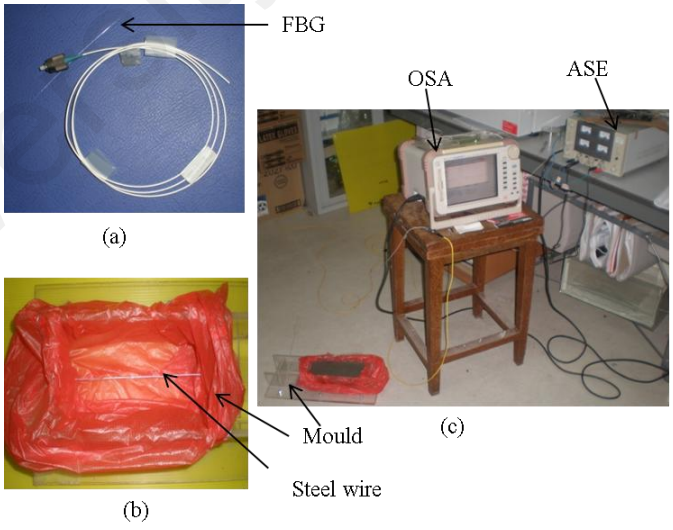

Fig. 4.5: Experiment preparation and setup of FBG monitoring approach.

4.1.3 Results and discussion

The measured early-age curing temperature of the cement paste at the first 19 h

after casting is shown in Fig. 4.6. This figure is plotted based on the Eq. (4.3), where the wavelength shift data are recorded by the OSA. In this figure, the temperature of the air is recorded before the specimen is poured into the mould. The starting point in this figure is 25 ℃ which is the temperature of the surrounding air. From the figure, it can be observed that the temperature of cement paste increases immediately after the cement paste is poured into the mould which is due to the absorption of water during the hydration of cement. Hence, the starting point can be referred to as the initial setting time of the specimen. Furthermore, the hydration of cement is an exothermic reaction which releases heat and resulting in the increase of the temperature of the specimen. The increment of the temperature is observed and reaches its peak at about 5 h. This time is treated as the final setting time of the specimen. After that, the increases in temperature of cement paste slow down and became almost stable at time of 19 h.

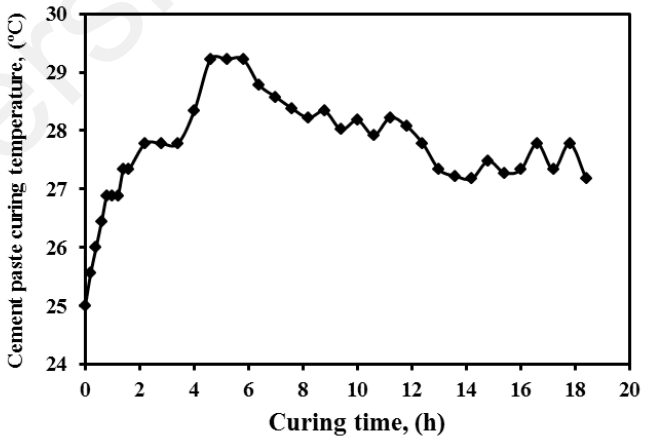

Fig. 4.6: Experiment result of FBG as sensing element.

4.2 Hydration process monitoring by using TPFS

4.2.1 Experimental works

4.2.1.1 Sensor probe

Many of TPFS probes were fabricated by using the approach described in previous chapter. The tapered optical fibers with a tapered length of 5.0 cm and diameter of 480 μm were used in this study.

4.2.1.2 Cement Paste Mixture

Before pouring the cement paste into the mould a tapered fiber and a type T thermocouple were fastened on a steel wire where the steel wire was inserted parallel through the centre of mould. The head of the thermocouple was located at the centre position but not touching the tapered fiber in order to ensure that the same ambient temperature is surrounding both sensors. Moulds with sizes of 7.5×7.5×20 cm and 2.5×2.5×20 cm were used to contain the mixed cement paste and a plastic sheet covered the mould to prevent vaporization of water. The room temperature was kept at 25 ℃. The mixture materials, cement, sand and water, etc. were stored at room temperature of 25 ℃ for 1 day. Before mixing with water and super plasticiser, all of other elements were mixed together in a drum mixer for about 20 min. Then, the water and super plasticiser were added into the drum mixer for 2 minutes and poured into the mould slowly to prevent bending of the steel wire. The mould was vibrated for 15 seconds by hand and the data recording/monitoring system was started immediately. The mixed cement paste with a mixture proportion is shown in Table 4.1. Three w/c ratios, 0.4, 0.5

and 0.6 were prepared by using the above method.

Table 4.1: The mixture of cementitious materials.

Materials	w/c=0.4	w/c=0.5	w/c=0.6
OPC (kg)	1.98	1.98	1.98
Water (kg)	0.792	0.990	1.188
Superplasticiser3% (l)	0.07	0.07	0.07
Silica Fume (kg)	0.20	0.20	0.20
Sand (kg)	2.54	2.54	2.54

4.2.1.3 TPFS calibration

The measurement of the early-age curing temperature of the cement paste for the first 24 hours after casting is shown in Fig. 4.7 (a). The temperature of the air was recorded before the specimen was poured into the mould. Fig. 4.7 (a) shows that the normalized output power suddenly decreased from 1mV to 0.528mV when the specimen was poured into the mould. This is because the sensor was initially surrounded by air then changed to the cement paste, which has different refractive indices. This caused the change of output power. The measurement results of thermocouple also presented for the purpose of comparison and calibration with the TPFS. As shown in Fig. 4.7 (a), the curves of the thermocouple and TPFSs agree well with each other, if flips down the curve of thermocouple. Thus, the curve of TPFS can precisely indicate the early-age curing temperature change as the curing progresses.

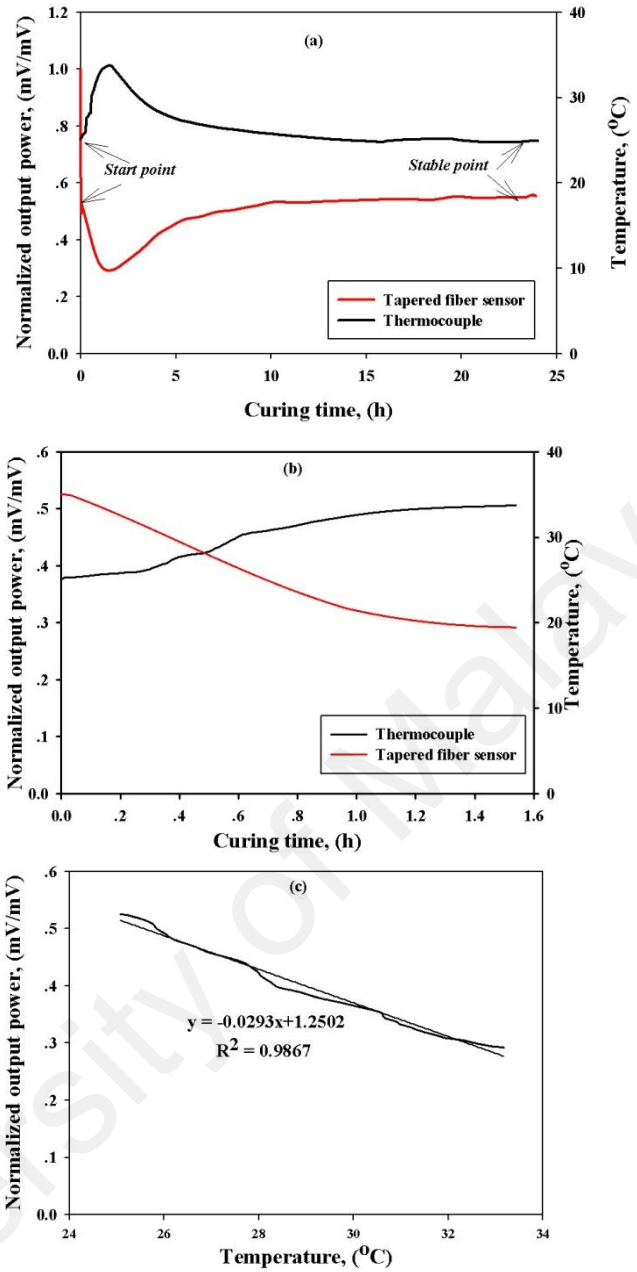

Fig. 4.7: The experiment results of thermocouple and TPFS (w/c=0.5).

A closer comparison is shown in Fig. 4.7(b), in which the data are presented for the thermocouple and TFS over a time period of 0 to 1.54 h. As shown in Fig. 4.7(b), the curves of the thermocouple and proposed sensor agree well with each other if one flips down the curve of the thermocouple. From Fig. 4.7(b), it is easy to calibrate the temperature sensitivity of the TFS, which is shown in Fig. 4.7(c). From Fig. 4.7(c), it can be seen that the TFS has a temperature sensitivity of 0.0293 mV/℃, and the

coefficient of determination, R2, is 0.9867. This coefficient indicates that the two curves in Fig. 4.7(b) closely overlap. Thus, the curve of TFS can precisely indicate the early-age curing temperature change as the curing progresses. The resolutions are determined when the sensor system has a measurement sensitivity of 10μV, which is ±0.34 ℃. The higher resolution of TPFS is obtained from the sensor with higher sensitivity. In the sensor system, the stability of sensor is strongly dominated by the stability of laser source which has the long-term power drift ±2% per hours.

From the curve of TPFS in Fig. 4.7(a), it can be observed that the temperature of cement paste increases from initial normalized output power of 0.528mV (25 ℃) to a recorded minimum value of normalized output power of 0.291mV (33.1 ℃) after the first 1.54h and increases immediately from there due to the absorption of water during the hydration of cement. Hence, the starting point can be referred to as the initial setting time of the specimen. Furthermore, the hydration of the cement is an exothermic reaction, which releases heat and results in the increase of the temperature of the specimen. The increment of the temperature is observed and reaches its peak after about 1.54 hours. This time is treated as the final setting time of the specimen (Neville, 1987). After that, the increases in the temperature of the cement paste slow down and became almost stable at 10 hours.

4.2.2 Results and Discussions

4.2.2.1 Effect of Specimen Size

The curing temperature curves for the first 24 h of hydration are shown in Fig. 4.8 for the mould size of $7.5 \times 7.5 \times 20$ cm^3 and $2.5 \times 2.5 \times 20$ cm^3, respectively. From Fig. 4.8, it can

be seen that the curing temperature rises with increasing size of the mould. The dip positions (at y-axis) are 0.291mV and 0.369 mV which corresponds to the curing temperatures of 33.1 ℃ and 30.9 ℃ for mould sizes of 7.5×7.5×20 cm^3 and 2.5×2.5×20 cm^3, respectively. It is also observed that the dip position (at x-axis) progresses earlier for smaller sample size (at 1.14 h) than that of for bigger sample size (at 1.54 h). It suggests that the setting time of specimen is strongly affected by the size of specimen. The bigger size of specimen processes the longer time for setting the cement. This observation suggests that a proper specimen size should be selected for different curing purposes, such as the expected strength of cured cement.

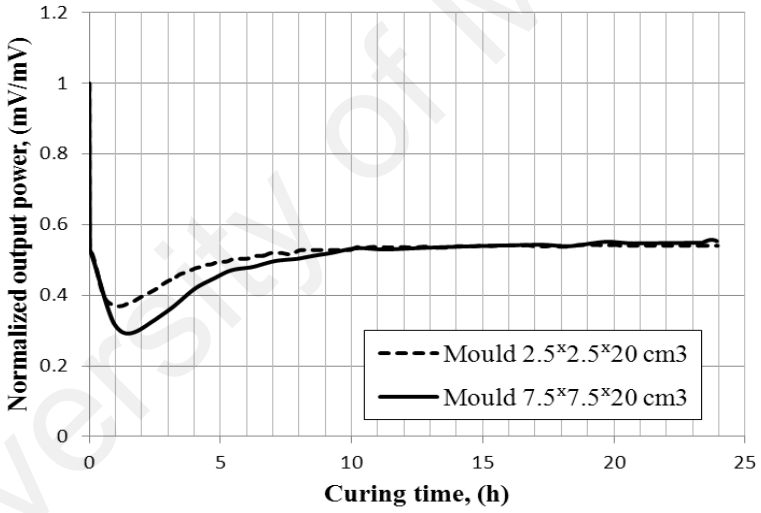

Fig. 4.8: The experimental results of the hydration process of cement paste with various specimen sizes (w/c=0.5).

4.2.2.2 Effect of Various w/c Ratios

Three w/c ratios, 0.4, 0.5 and 0.6 were used to investigate the early-age curing temperature of cement pastes and its results are shown in Fig. 4.9. In this figure, the difference between three curves clearly reflects that the curing temperature is strongly

affected by w/c ratio. The curing temperature rises with the increasing of w/c ratio. A bigger temperature rise is observed from the increasing of w/c ratio. The higher w/c ratio of cement paste has more volume of water and available microstructure space to hydrate the cement. It can turn a higher liberated heat (temperature) resulting a higher ultimate degree of hydration. From this figure, it can also be observed that the dip positions (at x-axis) of three curves are functions of change of w/c ratios. The higher w/c ratio of cement paste needs longer time to process the hydration. Therefore, the setting time of cement paste can be shortened by decreasing the w/c ratio.

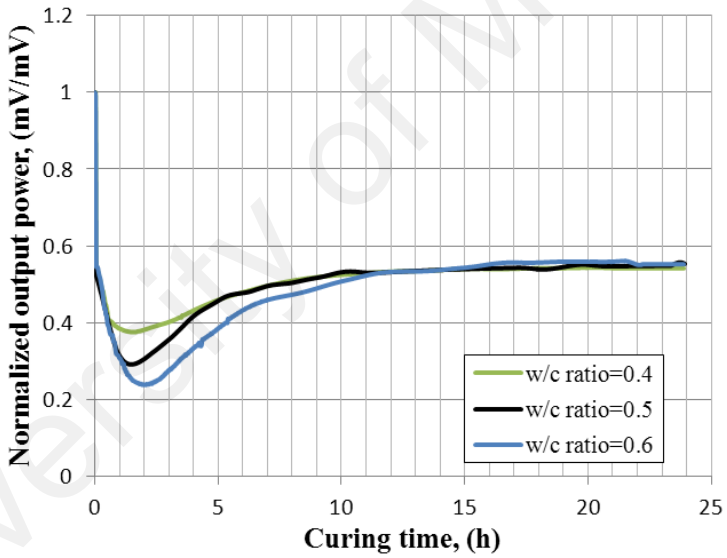

Fig. 4.9: The experimental results of the hydration process of cement paste with various w/c ratios.

4.2.2.3 Effect of Different Ambient Temperatures

The results in Fig. 4.10 show the curing temperatures are influenced by three different ambient temperatures of 20 ℃, 25 ℃ and 30 ℃, respectively. From this figure, it can be seen that the curing temperature is affected by the ambient temperatures. The

three curves indicate that the peak temperature (dip position at y-axis) is decreased by reducing the ambient temperature. The dip position (at x-axis) is delayed by the decreasing of ambient temperature. From this figure, it also can be seen that the hydration of cement is accelerated at early age under high ambient temperature but decelerated later on. Under high ambient temperature, the initial hydration forms a layer of coating on the surface of the cement specimen, which delays the process of hydration. The increasing of ambient temperature makes a thicker layer of coating. Under lower ambient temperature, the hydration of cement specimen is generally higher than under higher temperature (Ghosh, 2003). Thus, at early-age, the curing temperature is higher under higher ambient temperature. However, a longer time is gained under lower temperature for setting the cement paste.

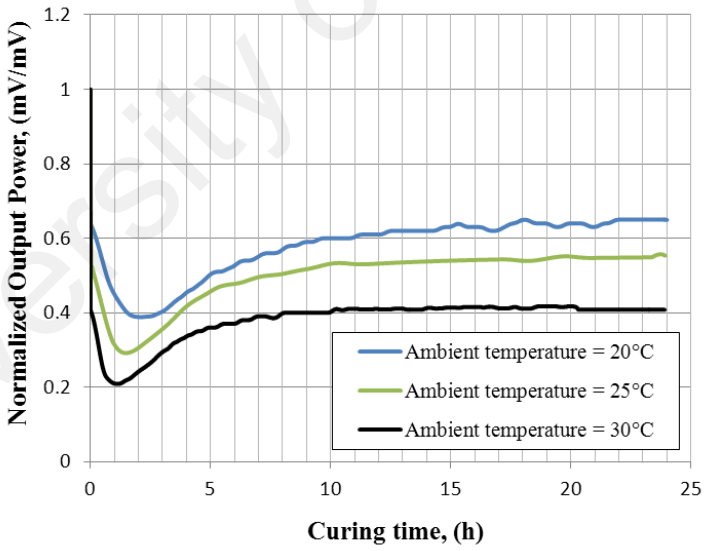

Fig. 4.10: The experimental results of the hydration process of cement paste with different ambient temperatures (w/c=0.5).

4.3 Summary

In this chapter, a FBG is used to study the hydration process of cement paste as a

comparative purpose. The fabricated and calibrated FBG was embedded into the cement material to detect the curing temperature of cement paste. Compared with FBG, however, a much cheaper and easier installation fiber sensor, namely, TPFS is employed to monitor the early-age hydration process of cement paste. The TPFSs were fabricated from tapering a cheap step-index multimode plastic optical fiber. The TPFS with stripped length of 5.0 cm and diameter of 480μm are used for all experimental. The sensitivity of 0.0293mV/℃, resolutions of ±0.34 ℃ and the stability of ±2% per hours are found and calibrated with an embedded thermocouple. The hydration process of cement paste was studied from influence of different sample sizes, w/c ratios, and ambient temperatures. The experimental results showed that the curing temperature rises with increasing size of the mould, decreasing of w/c ratio, and increasing ambient temperature. The setting time is shortened by smaller size of specimen, lower w/c ratio, as well as higher ambient temperature. The experiment results indicate that the proposed TPFS has the ability to monitor the curing temperature in order to find the setting time of the cement paste.

CHAPTER 5

VIBRATION AND CRACK DETECTION USING TAPERED PLASTIC FIBER SENSORS

5.1 Introduction

In this chapter, the TPFSs are used to study the vibration and crack detection in concrete beams (CB). The crack detection principle using the embedded tapered plastic fiber sensors (ETPFSs) is described by employing the V-number theory. The accelerometers, ETPFSs, and surface-mounted TPFSs are mounted on the full-scale reinforced CB to study the ability for vibration detection. The vibration was monitored before and after crack occurrence to predict the structural conditions of the CB. A four-point loading test was applied for several samples to evaluate their ability to monitor the crack and beam deflection. For crack detection, the scale-model CBs and full-scale reinforced CBs are used, in which the TPFSs were embedded. In addition, some TPFSs were mounted on the surface of the CBs in order to explore the sensor performance affected by the sensor installation approaches between the embedded sensors and the surface-mounted sensors. The linear variable differential transformer **(**LVDT) sensors and strain gauges were employed to detect the deflection and strain of the CBs when the CBs were being load-tested.

5.2 Crack detection principle of embedded TPFS

The configuration of the embedded TPFS for the experiments on crack detection is similar to the configuration as shown in Fig. 3.1 for the hydration process monitoring. After the CB had been cured for 28 days, the tapered fiber was embedded inside a relative stable environmental, with the exception of the change of ambient temperature and humidity. Humidity effects can be ignored as described before in section 3.2.2.1. In a laboratory environment, the embedded tapered fiber sensor can then be used to detect the strain and crack of a loaded beam if there is no change of ambient temperature. For a loaded CB, the properties of embedded POF involve two separate parameters—namely, photoelastic effect and mechanical effect. The photoelastic effect induces the change of refractive index in fiber core, and the deflection of POF is considered the effect of mechanical property (Kiesel et al., 2007).

Accordingly, a V-number theory is employed to analyse the crack detection principle of the embedded TPFS, which is based on the effects as described above. *V* number is a parameter to describe the number of propagation modes guided by the optical fiber, which is defined by Snyder and Love (1983).

$$V = \frac{2\pi r}{\lambda}\sqrt{n_{co}^2 - n_{aq}^2} \tag{5.1}$$

where r is the fiber radius, λ is the transmitted light wavelength, n_{co} is the refractive index of the fiber core, and n_{aq} is the refractive index of the surrounding medium.

As shown in Fig. 3.1, the number of transmission modes is determined by the tapered fiber radius r_0, the refractive index of the fiber core $n_{co,}$ and cement paste n_{aq}, respectively. It is assumed that the refractive index change of concrete induced by the loading stress can be ignored. It is reasonable to make this assumption because a small

change in the refractive index of the concrete can only perturb the higher-order modes in the modes guided by TPFS, in which the energy carried by the higher-order modes is much less than that of the lower-order modes. In the absence of external loading, the guided modes of the embedded tapered fiber is governed by

$$V_e = \frac{2\pi r_\varepsilon}{\lambda}\sqrt{n_{co(\varepsilon)}^2 - n_{aq}^2} \tag{5.2}$$

where $n_{co(\varepsilon)} = n_{co} + C_f \times S_c$, $n_{co(\varepsilon)}$ is the refractive index of the embedded fiber, r_ε is the fiber radius of the embedded fiber, C_f is the stress optic coefficient of the fiber core, $S_c = E \times \varepsilon$ is the stress applied to the embedded fiber, ε is the strain of the embedded fiber, $E = 0.1 \times 10^{10}$ N/m^2 is the Young's modulus of POF.

For a loaded CB, the guided modes can be classified under three cases according to the strain of the embedded fiber.

Case 1, small strain on the POF, the loading force perturbs the refractive index of POF only,

$$V_1 = \frac{2\pi r_\varepsilon}{\lambda}\sqrt{n_{co1(\varepsilon)}^2 - n_{aq}^2} \tag{5.3}$$

where $n_{co1(\varepsilon)} = n_{co(\varepsilon)} + C_f \times S_f$, where $S_f = \varepsilon_f \times E$ is the refractive index change of the fiber core induced by the strain ε_f applied on POF.

Case 2, the large strain on the POF, caused the embedded fiber to bend

$$V_2 = \frac{2\pi r_{\varepsilon}}{\lambda}\sqrt{n_{co2(\varepsilon)}^2 - n_{aq}^2} \tag{5.4}$$

where $n_{co2(\varepsilon)} = n_{co1(\varepsilon)}(1+\frac{x}{n_e})$, x is the bending radius,

$n_e = \frac{R}{1-\frac{n_{co1(\varepsilon)}^2}{2}[P_{12}-\nu(P_{11}+P_{12})]}$, R is the bending radius, P_{11}=0.30 and P_{12}=0.297 are the components of the photoelastic tensor. $n_{co2(\varepsilon)}$ is the refractive index of the bending fiber in which a conformal mapping technique is employed to transform the curved fiber to an equivalent straight fiber (Ulrich et al., 1980). For a bending fiber, a change occurs to the refractive index of the fiber upon bending due to the photoelastic effect. The inner half of the fiber stands a compressive stress towards the centre of the bend, and a tensile stress is applied along the outer half of the fiber.

Case 3, the CB is cracked resulting in the reduction of fiber radius,

$$V_3 = \frac{2\pi r_{\varepsilon r}}{\lambda}\sqrt{n_{co2(\varepsilon)}^2 - n_{aq}^2} \tag{5.5}$$

where $r_{\varepsilon r} = r_{\varepsilon}(1-\nu\varepsilon+\alpha\varepsilon^2)$ is fiber radius reduced by the strain ε applied to the fiber (Kiesel et al., 2007). ν=0.34 is the Poisson's ratio for POF, α = -2.3 is the nonlinearity constant in the transverse elongation.

From Eq. (5.5), it can be seen that the V number of TPFS is governed by the applied strain of the embedded fiber; it induced the change of the refractive index and the radius of the fiber. V number is a parameter that can be used to indicate the light intensity which is guided by the TPFS. As such, the transmitted light intensity guided by the embedded TPFS can be modulated by the applied strain and thus its capability for crack detection.

5.3 Experimental materials and methods

The materials and procedure for crack detection are similar to the materials and procedure for the cement paste hydration studies. A brief description follows. A more detailed account has been presented in previous chapters. In this chapter, two types of CBs are prepared—namely, scale-model CBs and full-scale reinforced CBs. The loading test is performed on the scale-model CBs and full-scale reinforced CBs. The vibration detection is studied on the full-scale reinforced CBs.

5.3.1 Specimen preparation

5.3.1.1 Scale-model concrete beam specimen

A TPFS was embedded together with a type T thermocouple and a strain gauge for calibration purposes. All of these elements were fastened to a steel wire, which was inserted parallel to the centre of the mould. Three sensing elements were carefully aligned to make sure there is no contact with each other and the head of the thermocouple and the strain gauge were located at the centre position of TPFS region to ensure the same condition for all elements. The mould (with size $100 \times 100 \times 500$ mm) was used to contain the mixed cement paste, and a plastic sheet was covered on the mould to prevent the evaporation of water. To ensure the accuracy of the experiment, all of the experimental material preparations were carried out at a room temperature of 25 ℃. The OPC, silica fume, and sand were mixed together by a drum mixer for about 20 minutes. Then, water and a superplasticiser were added into the drum mixer for 2 minutes and poured into the mould slowly to prevent the bending of the steel wire. The

mould was vibrated for 15 seconds by hand, and the data recording/monitoring system for curing the temperature measurement was started simultaneously. The used mixture cementitious materials are shown in Table 5.1.

The curing temperatures and curing strains were monitored for the first 24 hours after the cement paste was cast. The moulds were removed after 3 days of casting. After that, the beams were stored at a room temperature of 25°C for more than 28 days. A total of six scale models of CBs were cast by using two grades of cement, 35 and 40, respectively.

Table 5.1: The mixture of cementitious materials for scale-model CBs

Materials	OPC (kg)	Water (kg)	Superplasticiser 3% (l)	Silica Fume (kg)	Sand (kg)
w/c=0.5	1.98	0.99	0.07	0.20	2.54

5.3.1.2 Full-scale reinforced concrete beam specimen

Two reinforced CBs with dimensions of 150 mm × 250 mm × 2300 mm were prepared using standard procedures. The details of the mix proportion of these beams are shown in Table 5.2. The cement grade of 30 was used in this experiment.

Table 5.2: The mixture of cementitious materials for full-scale reinforced CBs

Materials per m^3	OPC (kg)	Water (kg)	Coarse aggregate (kg)	Sand (kg)
w/c=0.67	317	208	735	1140

The configuration of reinforced CB was photographed and shown in Fig. 5.1(a).

Concrete strengths of 35 MPa and 40 MPa were cured for two reinforced CBs, respectively. Fig. 5.1 (b) shows that the full-scale reinforced CBs consist of the deformed bars with a diameter of 10 mm, plain bars with a diameter of 8 mm, and steel stirrups with a diameter of 6 mm.

Two TPFSs were embedded into a CB. The location of the embedded TPFS is shown in Fig. 5.1 (c). As shown in this figure, one of TPFSs is fastened with a thermocouple and a strain gauge on a reinforced bar, which is located at the centre of the CB. These elements are located as close as but not touching each other so as to avoid any interference. One TPFS was mounted on the top surface of the CB, which withstands a different strain with that of the embedded TPFS in the centre of the CB. Furthermore, an LVDT sensor system is mounted on the bottom surface of the CB to detect the deflection.

(a) Photograph of reinforcement for full-scale reinforced CB.

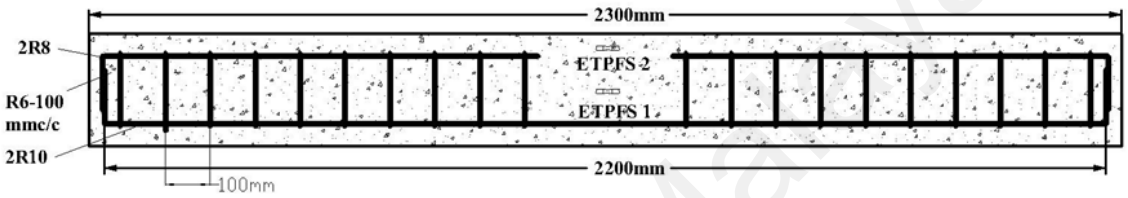

(b) Layout of reinforcements.

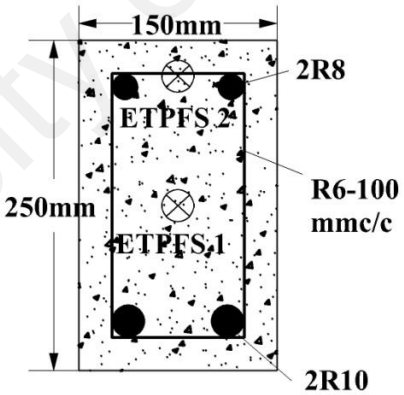

(c) Cross-section view of reinforcements and ETPFSs.

Fig. 5.1: The reinforcement configuration of the full-scale reinforced CB.

5.3.2 Experimental setup

5.3.2.1 Casting monitoring system

The experimental setup of hydration process monitoring is shown in Fig. 5.2. In this figure, a DC power supply is used to drive a light-emitting diode (LED) (red light, centred at 660 nm), which is acting as the light sources. The TPFS, thermocouple, and strain gauge are placed in the centre of the mould. High-speed photologic detectors are employed to detect the received light intensity and convert it as voltage signals. A TDS-530 data logger is used to collect the signals of the thermocouple, strain gauge, and TPFSs. The TDS-530 data acquisition system is set at 640mV detection range. The data logger is also set for acquisition of one point at a one-second interval.

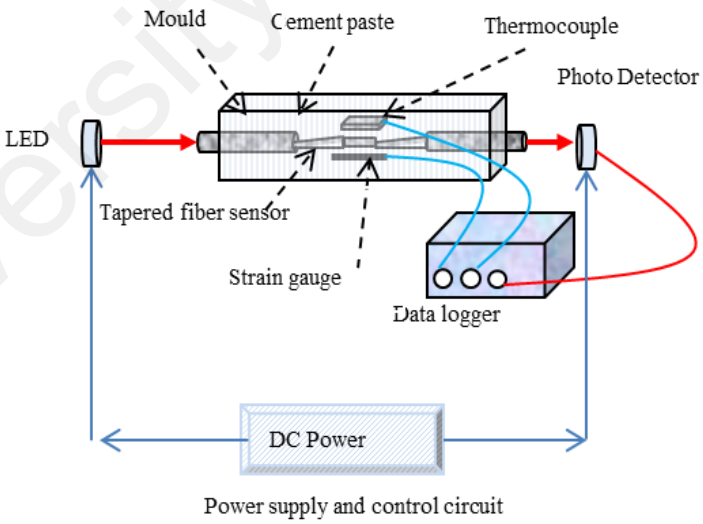

Fig. 5.2: Experiment setup of hydration process monitoring.

5.3.2.2 TPFSs for vibration and loading test monitoring system

The TPFSs system for vibration and loading test monitoring is shown in Fig. 5.3. In this system, many TPFSs are multiplexing into one system. A power supply with an output voltage of ~1.9 V is used to drive the LEDs. A circuit is designed to control the output of power supply. This control circuit is functioned to maintain the output voltage as close to 1.9 V. A long-term drift study indicates that the power supply has a very good stability, which is ±1%. The LEDs derived by this power supply show an excellent stability for output light intensity. The light passes through the TPFSs and is collected by photodetectors. The photodetector converts the light signal into a voltage. Then the voltage signals are received by an integrated measurement control instrumentation (IMC) data logger. In this system, all of the TPFSs are synchronized to detect the vibration and cracks on a full-scale reinforced CB.

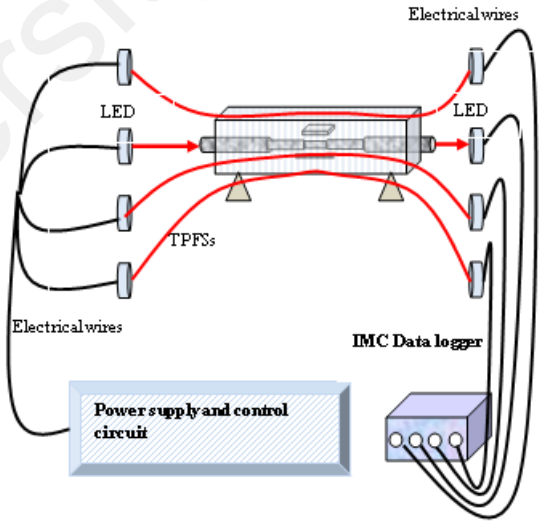

Fig. 5.3: Experiment setup for vibration and loading test using TPFSs systems.

5.3.2.3 Vibration monitoring system

The configuration of a vibration monitoring system is shown in Fig. 5.4. A 3.1 MHz function generator and an amplifier are employed to drive the shaker to produce vibration information. The function generator has a frequency range of 1–100 Hz. As shown in this figure, a total of six Kistler accelerometers are used as reference devices. Five of them are attached to the upper surface of the CB, one of them and a TPFS are mounted on the surface of the shaker as a reference input. Five TPFSs are mounted on the side surface of the CB and are located at the same position with that of the Kistler accelerometer. Each sensor is positioned at a distance of 425 mm apart. The sensors are attached to the CB to provide information of the vibration of the CB, while the mounted sensors on the shaker are used to provide reference information. Besides, two ETPFSs are employed to monitor the vibration of the CB as shown in Fig. 5.4 (b). An IMC data logger (Model D5335) is used to collect the signals of the Kistler accelerometers and TPFSs. The IMC data logger is set to acquire at 100 Hz. A system with this setting can provide a very high precision for vibration detection for both the Kistler accelerometers and the TPFSs.

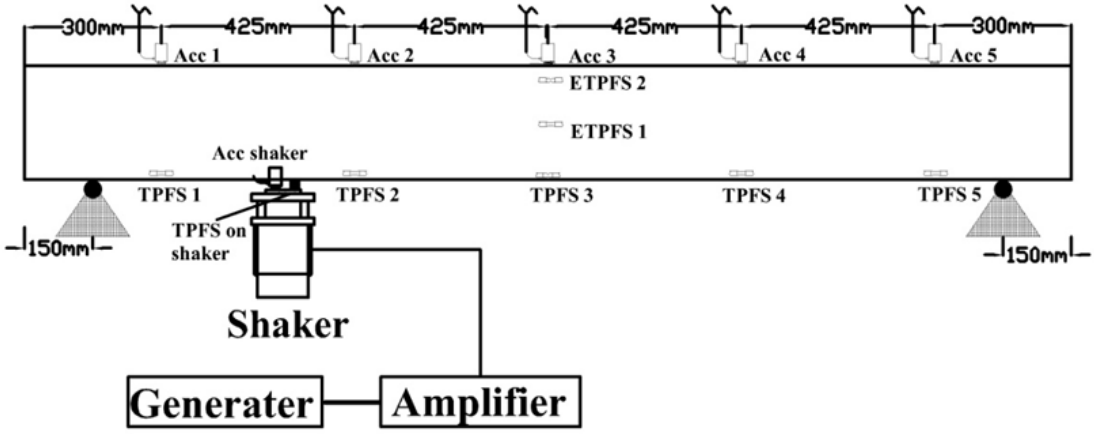

(a) Layout of accelerometers TPFSs and ETPFSs installation.

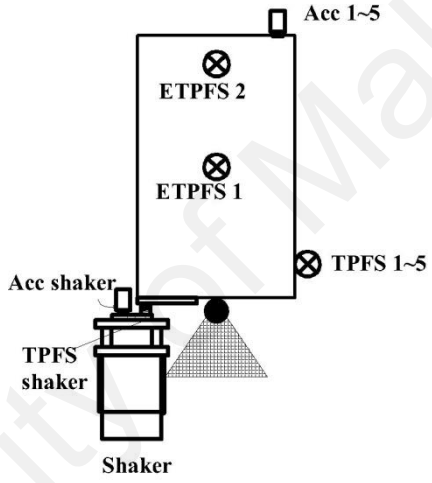

(b) Cross-section view of sensors installation.

Fig. 5.4: Experimental setup of a vibration monitoring system.

5.3.2.4 Loading test system

In this study, a four-point bend loading test was applied to all the CBs. The loading test system is shown in Fig. 5.5 (a). Fig. 5.5 (b) shows the loading force applied to a scale-model CB. A minimum loading force rate of 0.02 kN/sec was used for all scale-model CBs. The loading is controlled by an Excute UCS-608 Meas data acquisition system. Experimental results found that the scale-model CBs have a load force range (crack occurred) of 14 kN to 17 kN, depending on the grade of the cements.

A CB cast by a higher-grade cement withstands a higher loading force. A single ETPFS is employed to detect the strain and crack of the scale-model CBs where an embedded strain gauge and a surface-mounted strain gauge are used for comparative purposes.

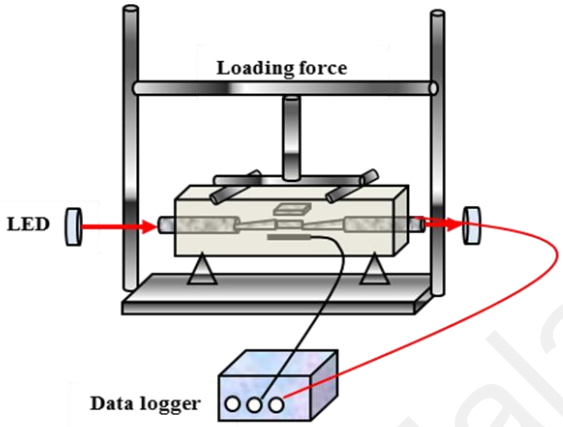

(a) Loading test for scale-model CB

(b) Photograph of loading test for scale-model CB.

Fig. 5.5: Four-point loading test system for scale-model CB.

For a full-scale reinforced CB, the universal testing machine (UTM) Instron 8800 was used for the loading test as shown in the photograph in Fig. 5.6 (a). The UTM has a minimum loading force of 0.01 kN; however, a loading rate of 2 kN/second is applied due to the higher strength of the reinforced CB. To fully monitor the health conditions of the full-scale reinforced CB, the LVDTs, strain gauge, and TPFSs are used in this study. The configurations of the sensors installation are shown in Fig. 5.6 (b). A TDS

530 data logger is used to collect all the data, including TPFSs, strain gauge, loading tester, LVDTs. The data logger is also set for an acquisition of one point at a one-second interval.

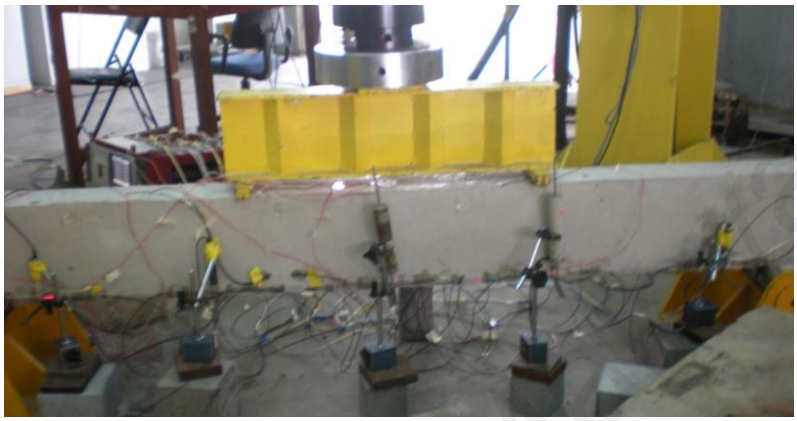

(a) Photograph of loading test for full-scale reinforced CB.

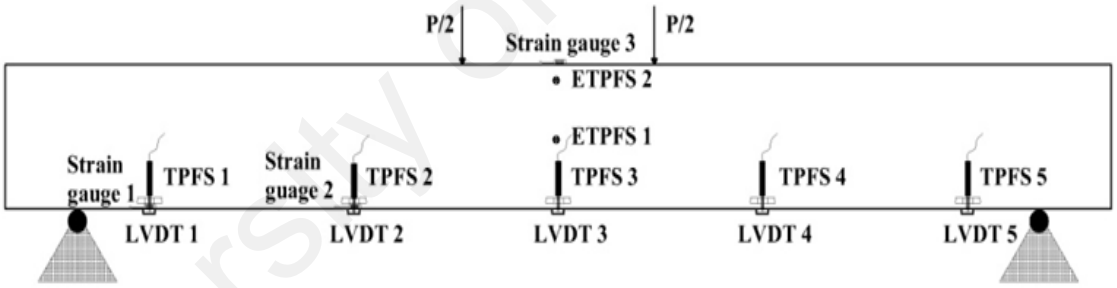

(b) The placements of the strain gauges, TPFSs, and LVDTs.

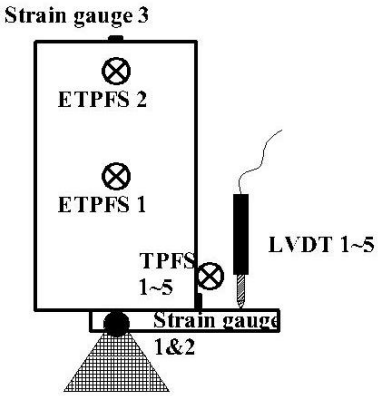

(c) Cross-section view of the sensors installation.

Fig.5.6: Four-point loading test system for full-scale reinforced CBs and sensors installation.

5.4 Experimental results and discussion

5.4.1 Vibration monitoring

5.4.1.1 Beam analysis

A single-degree-freedom (SDOF) system is used to describe the vibration of the CB, in which the CB can be treated as a simply supported beam. The motion can be described by a single coordinate; the radian frequency depends on two system properties: mass and stiffness. The radian frequency of the SDOF system is given by

$$\omega_n^2 = \beta_n^4 \frac{EI}{(m/L)} \tag{5.6}$$

where $E = 57000 \times \sqrt{f_c}$ is the Young's modulus of elasticity, f_c is the concrete curing strength in the unit of psi, $I = \frac{a \times b^3}{12}$ is the moment of inertia, a and b are the width and height of the CB, m is the total distributed mass of the CB, L is the effective length of the CB, β_n is the boundary condition for different natural frequencies. For a simply supported beam, the boundary conditions are given by

$$\beta_n L = n \times \pi \tag{5.7}$$

By employing the boundary condition, the natural frequency of the CB can be calculated by

$$f = \frac{\omega}{2\pi} \tag{5.8}$$

5.4.1.2 The study of vibration monitoring using TPFSs with different installation approaches

In this experiment, the vibration responses were measured using surface-mounted TPFSs (SMTPFSs) (with different mounting methods) and ETPFSs. For SMTPFSs, the sensors were attached to the beam using two techniques, which are plastic tape and superglue. The two SMTPFSs on the surface of the CB were attached, located in the same horizontal position with that of the ETPFS. A vibration test was performed for the CB. The measurement data are shown in Fig. 5.7 (a)–(c). It can be observed that the signals in Fig. 5.7 (b) and (c) are much better than that in Fig. 5.7 (a). From this study, it can be concluded that the TPFS can be used to detect the vibration response of the CB, and the best performance is given by the ETPFS. For the cured CB without the embedded TPFS, the surface-mounted TPFS can also provide acceptable measurement results.

Comparing figures 5.7 (a), (b), and (c), it can be observed that the ETPFS (c) managed to capture the vibration response of the beam.

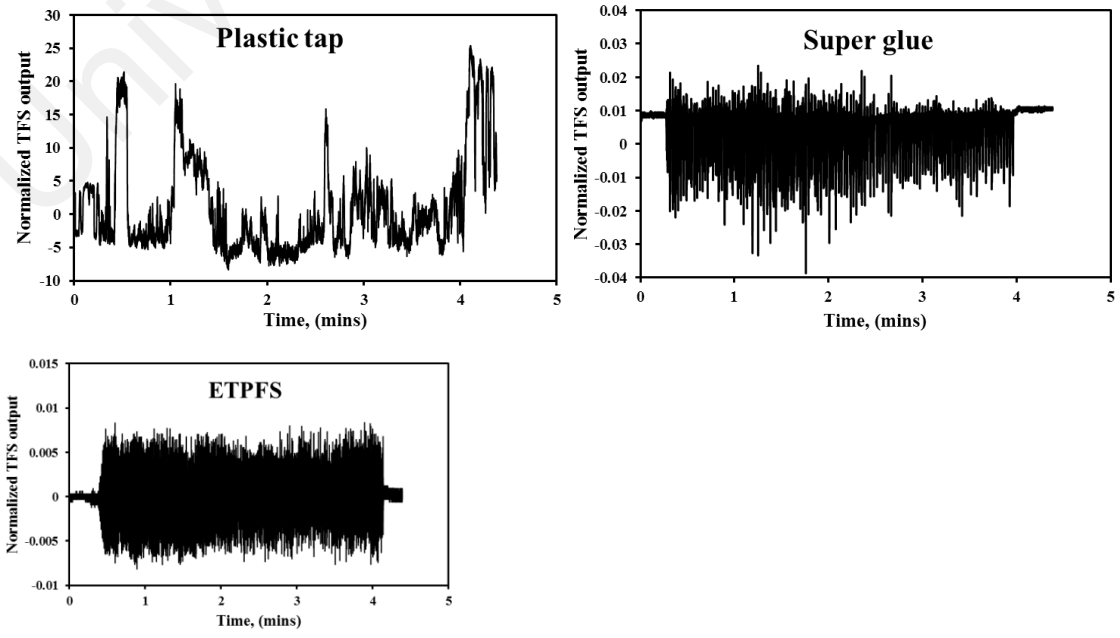

Fig. 5.7: The vibration monitoring using TPFSs with different installation approaches.

5.4.1.3 The study of the vibration monitoring using TPFSs with different taper diameters

In this study, three TPFSs with diameters of 900 µm, 700 µm, and 480 µm were fabricated using the technique described earlier. Three TPFSs were surface-mounted on the CB, which were placed next to each other in the same horizontal position. Fig. 5.8 (a), (b), and (c) show the detected vibration signals for the SMTPFS with diameters of 480 µm, 700 µm, and 900 µm, respectively. From this figure, it can be seen that the SMTPFS with a diameter of 480 µm gives the best performance compared to the other two SMTPFSs. The figures also show that the SMTPFS with a diameter of 900 µm has the worst performance. Hence, it can be concluded that the TPFS with a smaller diameter will give better performance for vibration detection.

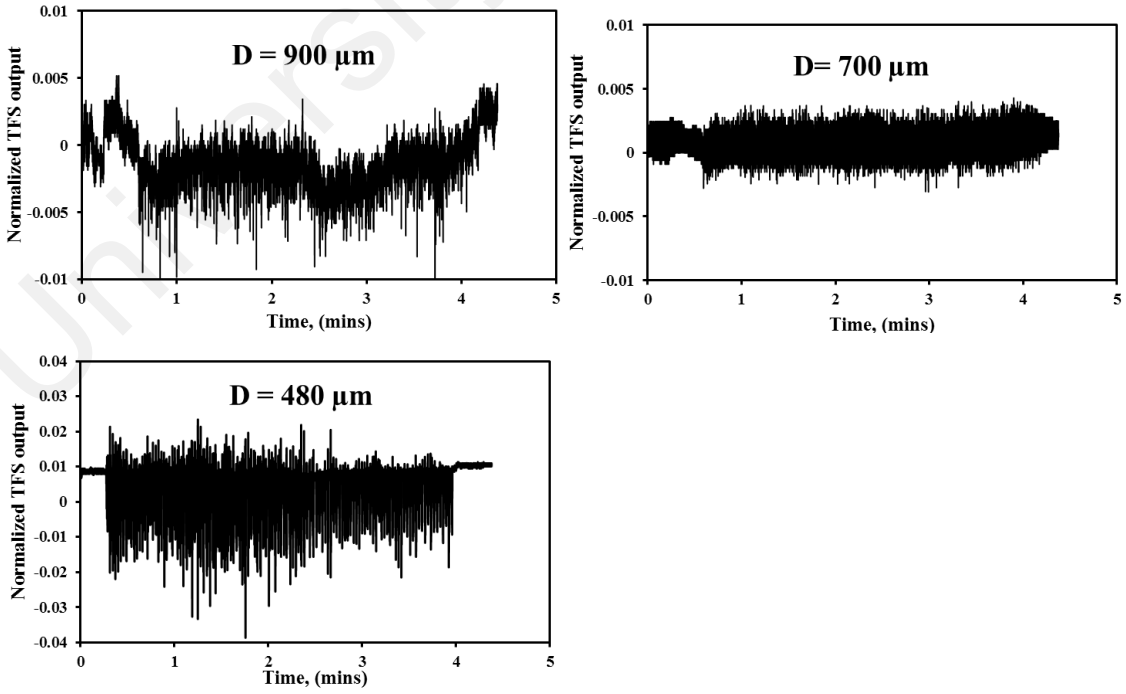

Fig. 5.8: The vibration motoring using TPFSs with different taper diameters (900 µm, 700 µm, and 480 µm).

5.4.1.4 Vibration monitoring on the full-scale reinforced CB

In order to predict the structural condition of the CB, the vibration test was implemented first by employing the accelerometers, ETPFSs, and SMTPFSs. Then a loading force was continually applied to the CB until the crack occurred. During the loading test, the attached accelerometer was removed, and SMTPFSs were kept attached on the CB to detect its crack. The crack detection results are given in the following section. Then, a vibration test was performed again for the cracked CB, in which the accelerometers were installed again. Typical vibration responses monitored by the accelerometer and TPFS are shown in Fig. 5.9 and 5.10 for before crack and after crack occurred on the CB, respectively.

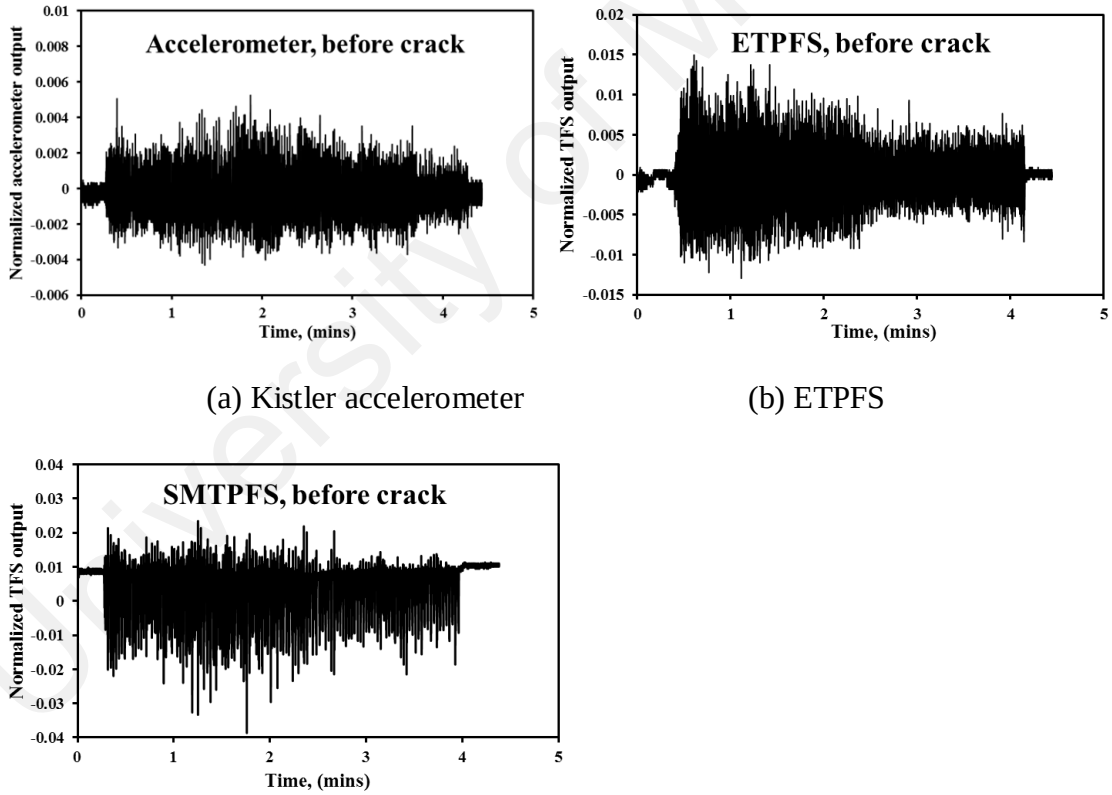

(a) Kistler accelerometer (b) ETPFS

(c) SMTPFS

Fig. 5.9: Vibration detected before crack by using (a) Kistler accelerometer, (b) ETPFS, and (c) SMTPFS.

In Fig. 5.9 and 5.10, it can be observed that both the TPFSs and the accelerometer

have the ability to indicate the vibration of the CB. The responses of TPFSs are constant with that of the accelerometer. Both of them can reflect the time for vibration start and stop precisely.

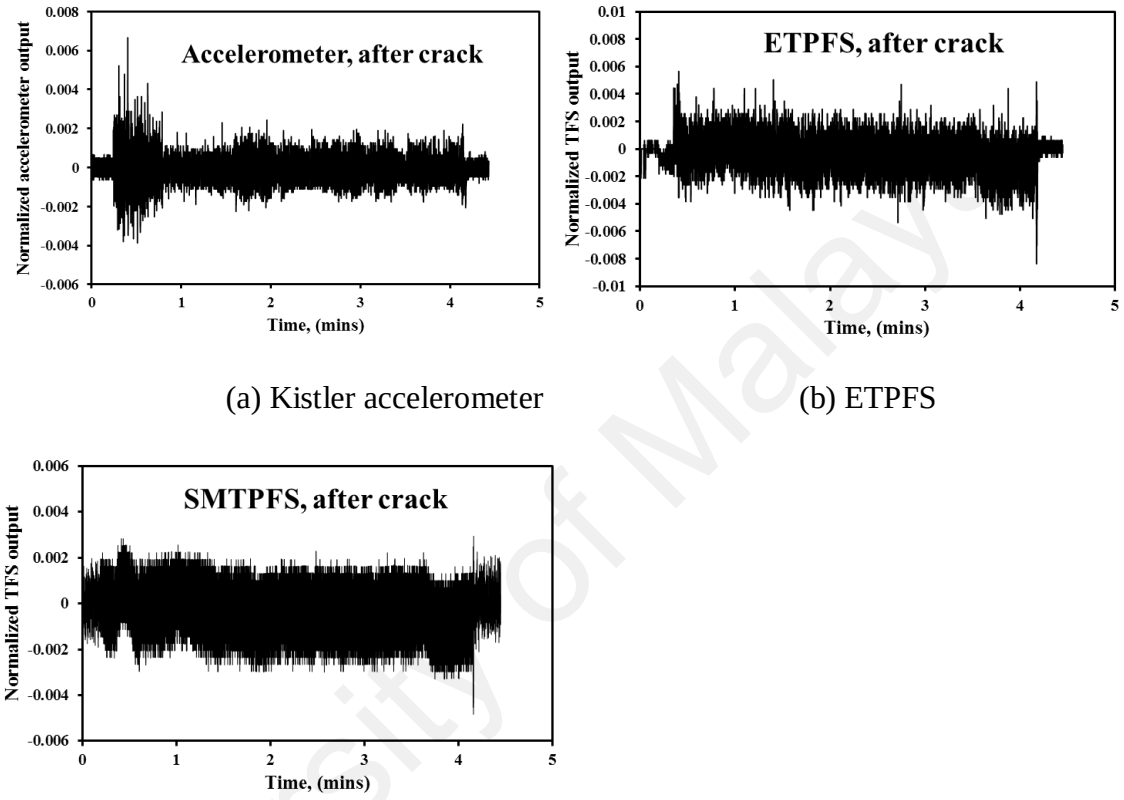

(a) Kistler accelerometer (b) ETPFS

(c) SMTPFS

Fig. 5.10: Vibration detected after crack by using (a) Kistler accelerometer, (b) ETPFS, and (c) SMTPFS.

5.4.1.5 Results and discussion

The vibration based on the accelerometer and TPFSs measurements are employed to establish the change in the modal frequencies of the CB. For a given structure, the damage detection methods based on modal frequencies are that any shifts in the natural frequencies indicate a change in its structure properties has taken place. The raw data detected by the accelerometers and TPFSs are stored, which are in time domain. In order to see its frequency responses, a low-pass Butterworth filter is applied to remove its high frequency parts, and then a fast Fourier transform (FFT) is performed on all of the data. In this study, a manual peak-picking technique is used to extract the natural frequencies of a structure. The peaks picking in the frequency spectra are based on the numerical results and the results recorded by the accelerometers. Further research is carried out to optimize the TPFS for vibration response in order to eliminate the noise signals, which are showing many small peaks in the spectra. By employing this technique, the raw data are transformed into the frequency domain, as shown in Figs. 5.11 and 5.12, for accelerometers, ETPFS, and one surface-mounted TPFS only for observation. The results detected by other accelerometers and TPFSs are similar to the results presented here, and they are not shown in this chapter.

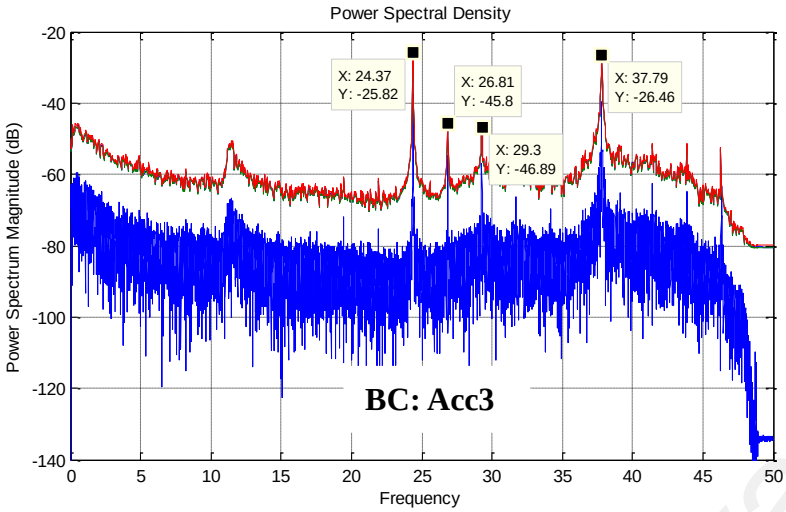

(a) Before crack: Acc3

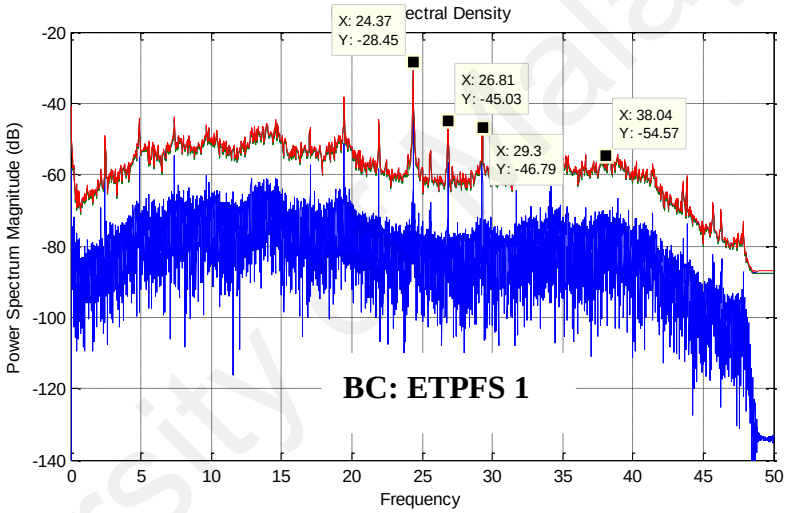

(b) Before crack: ETPFS 1

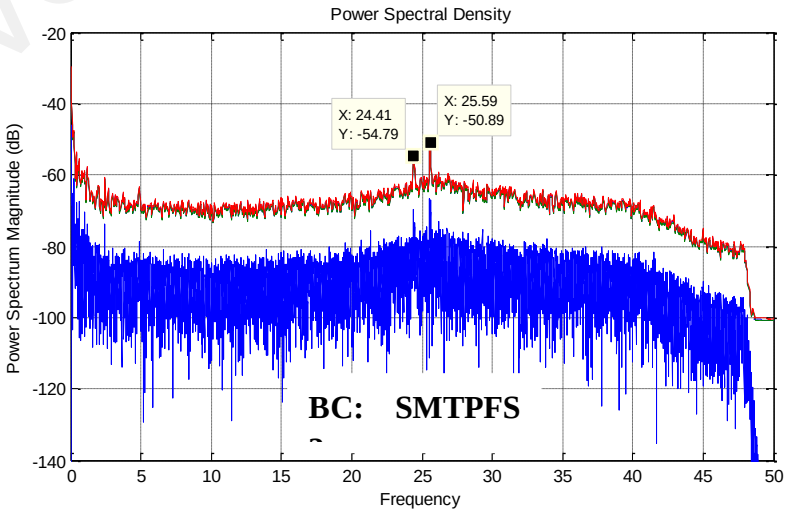

(c) Before crack: SMTPFS 3

Fig.5.11: Spectral density estimated from measurements using accelerometer, ETPFS, and SMTPFS.

Figs. 5.11 and 5.12 show the detected frequencies by the accelerometers and TPFSs for the CB before the loading test and after the crack occurred, respectively. The beam was excited by a shaker in the frequency range of 1~100 Hz with a sweep rate of 0.01 Hz. By using this vibration range, some natural frequencies can be estimated and observed in Figs. 5.11 and 5.12. Both of them have several spectrum magnitude peaks, and each of these peaks appears the same trends and location. Compare the figures between the ETPFS in Fig. 5.11 (b) and the SMTPFS in Fig. 5.11 (c); it can observed that the trend of the SMTPFS is not as good as the ETPFS, which can only estimate two peaks. But this result is still acceptable considering the peak's obvious stability. The correlation between the TPFS and the accelerometer for after cracked measurement in Fig. 5.12 is also similar to Fig. 5.11. Both the ETPFS and the TPFS can detect the CB's vibration response comparing the corresponding with the accelerometer's spectral density. However, the mode shape of the natural frequency is desired for analysis for future works.

The spectral density estimated from the measurement results are summarized in Tables 5.3 and 5.4. These tables show that TPFSs have the ability to detect the natural frequencies of the CB since they have almost the same detected frequency values as that of the accelerometers. For a cracked CB, the natural frequency of the CB will have a certain decrease; this can also be observed by comparing Tables 5.3 and 5.4. It can be concluded that both the accelerometers and the TPFSs have the ability to monitor the frequency shift on the CB.

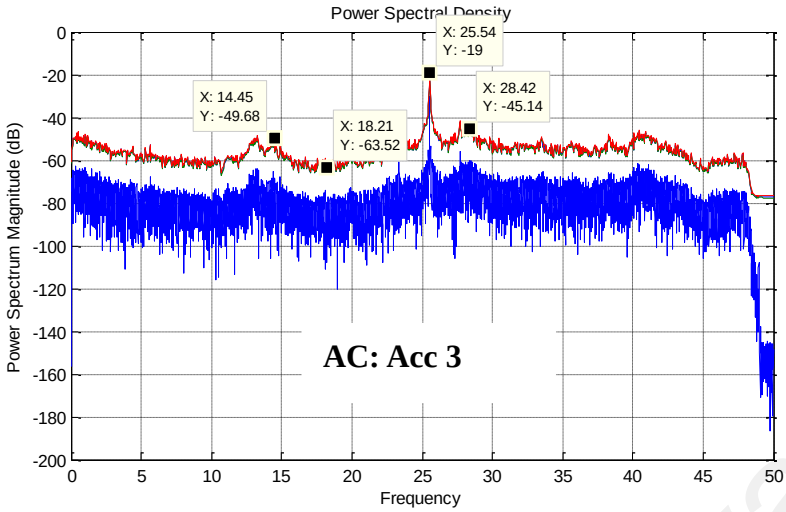

(a) After cracked: Acc 3

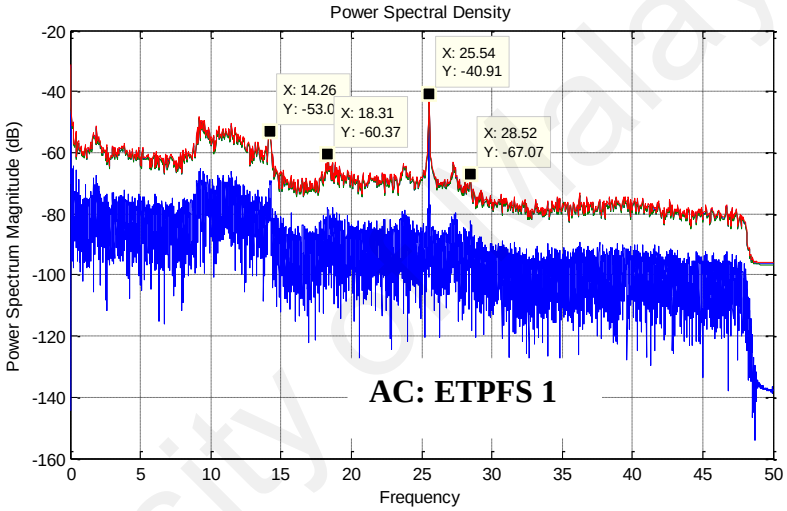

(b) After cracked: ETPFS 1

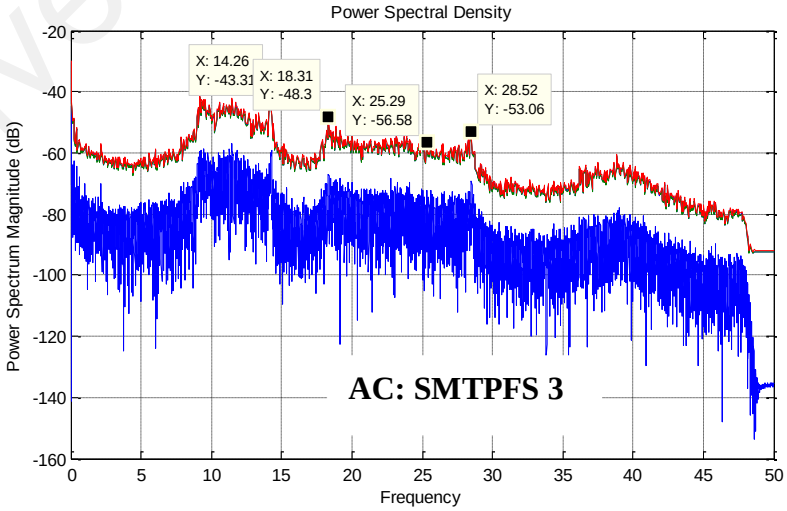

(c) After cracked: SMTPFS 3

Fig.5.12: Spectral density estimated from measurements, ETPFSs, and SMTPFSs after crack occurred.

Table 5.3: Summary of estimated frequency contents before crack

Estimated frequency contents before crack				
Acc 3	24.37	26.81	29.3	37.79
ETPFS 1	24.37	26.81	29.3	38.04
SMTPFS 3	24.41	25.59	-	-

Table 5.4: Summary of estimated frequency contents after crack

Estimated frequency contents after crack				
Acc 3	14.45	18.21	25.54	28.42
ETPFS 1	14.26	18.31	25.54	28.52
SMTPFS 3	14.26	18.31	25.29	28.52

5.4.2 Crack detection

5.4.2.1 Crack detection on the scale-model CBs

The results of the four-point bending test for scale-model CBs are shown in Fig. 5.13. When a loading force is applied on a CB, the beam exhibits a global deflection over its entire span region. In Fig. 5.13 (b), it can be seen that the beam deflection detected by an LVDT agreed well with the loading force history. The deflection of the beam is small when a 0.02 KN loading force is applied on it. This small deflection cannot perturb the propagation modes guided by the ETPFS. Hence, the ETPFS output is constant in such a loading force. The increase of loading force results in the rise of beam deflection, which will cause the increase of the bending radius of the ETPFS. ETPFS subjected to bending will induce higher propagation modes to become a leaky

mode which cannot be guided by the ETPFS. As such, in Fig. 5.13 (a), it can be observed that the light intensity of the ETPFS is decreased with the increase of the loading force applied. This remarkable result shows that the ETPFS has the ability to detect the axial strain and the crack initiation.

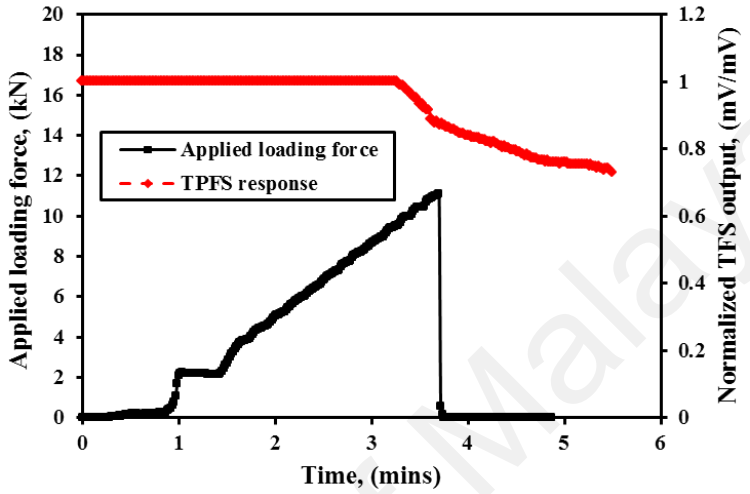

(a) ETPFS response to the applied loading force.

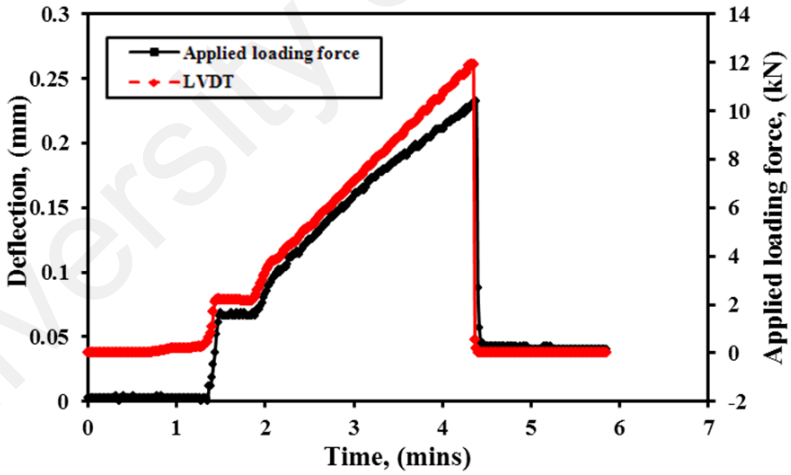

(b) The beam deflection detected by an LVDT.

Fig. 5.13: An applied loading force on the scale-model CB, (a) ETPFS response to the applied loading force, (b) the beam deflection detected by an LVDT.

From the theoretical analysis, it is found that the ETPFS can be employed to monitor the postcrack of the CB, in which the fiber diameter is reduced due to the mechanical effect. To test this ability, the loading force is increased continually. In Fig.

5.13 (a), it is evident that the ETPFS signal drops sharply when a peak loading force is applied on the CB. From this observation, it may be concluded that it was caused by the combination effects of photoelastic and mechanical deflection of the optical fiber. After reaching peak loading, a small step of loading force of 0.02 kN is continuously applied on the CB. The width of the crack is enlarged, which results in the diameter of the ETPFS being reduced continually. In Eq. (5.5), it can be observed that the reduction of fiber diameter will cause the decrease of the number of guided modes. Thus, a near-linear optical loss is observed in Fig. 5.12 (a).

5.4.2.2 Crack detection on the full-scale reinforced CBs

The results shown in Fig. 5.14 are the photomicrographs of the crack taken with a camera to determine the width of the crack that could be detected by the TPFSs. As shown in Figs. 5.15 and 5.16, the width of the crack is enlarged by increasing the loading force, which corresponds to the decrease of the output of the TPFSs.

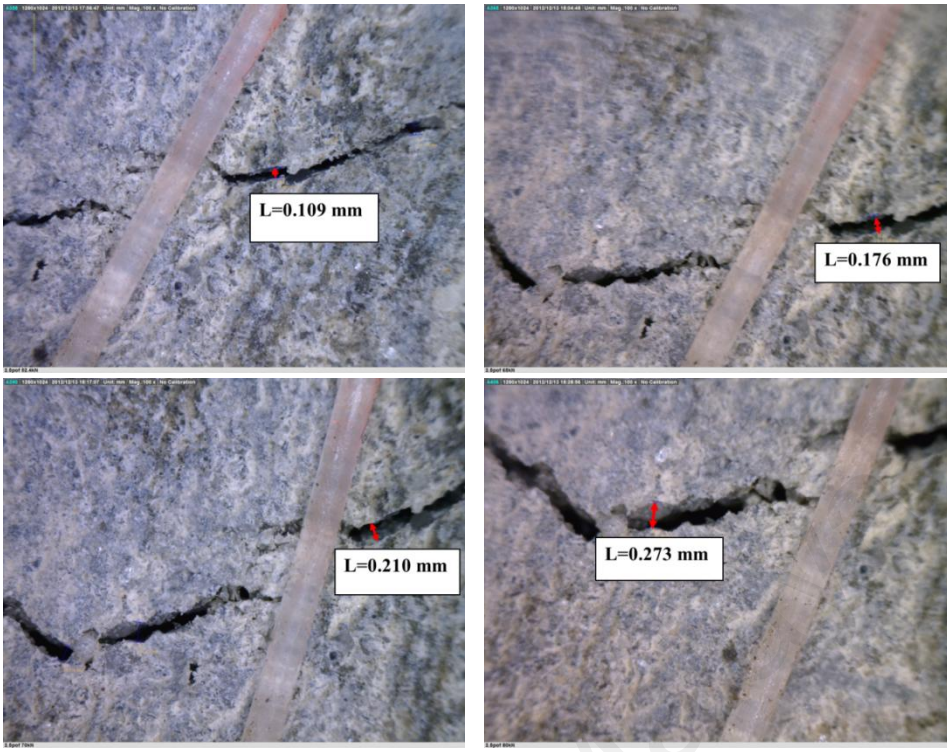

Fig.5.14: Photomicrographs of the cracks with different widths.

The structural condition of the full-scale reinforced CB is monitored by LVDTs for its deflection (Fig. 5.15 (a)), the strain gauge for its strain (Fig. 5.15 (b), and the TPFSs for its strain and crack (Fig. 5.15 (c)). In Fig. 5.15 (a), the curves of the LVDTs share the same trend with that of the loading force history. As known, the maximum deflection point occurred at the centre of the beam, and this value has become smaller with the point going closer to the support points. It is generally known as shown in Fig. 5.15 (a): a maximum deflection of 10.5 mm for LVDT 3 and a minimum deflection of 2.4 mm for LVDT 1. The minor different deflections between the LVDTs of 1 and 5, 2 and 4 may be due to the difference of the curing strength, structural, applied loading positions or LVDT systems on those monitored points. The findings in Figs. 5.15 (b1) and (b2) show that the monitored strains of the beam agreed with the trend of the loading force. As shown in Fig. 5.15 (b2), the strain detected by the strain gauge 3 is negative, which means a compressive strain is formed. Two curves in this figure are not

consistent with each other. This is because of the large crack formed on the top surface of the CB where the strain gauge is attached. However, from this curve it still can be found that the maximum compressive strain of 2450 με is detected by strain gauge 3. A maximum tensile strain of 846 με is detected by strain gauge 2 as shown in Fig.5.15 (b1). The maximum strains detected by three strain gauges are well reflected in the strain situations of the CB when a loading force is applied to it. This situation shows that the maximum strain occurred on the central top surface of the CB, and the next maximum strain happened on the central bottom surface of the CB, while the strain was decreasing with the detect point closing to the support point, if the loading force was applied to the central position of the CB.

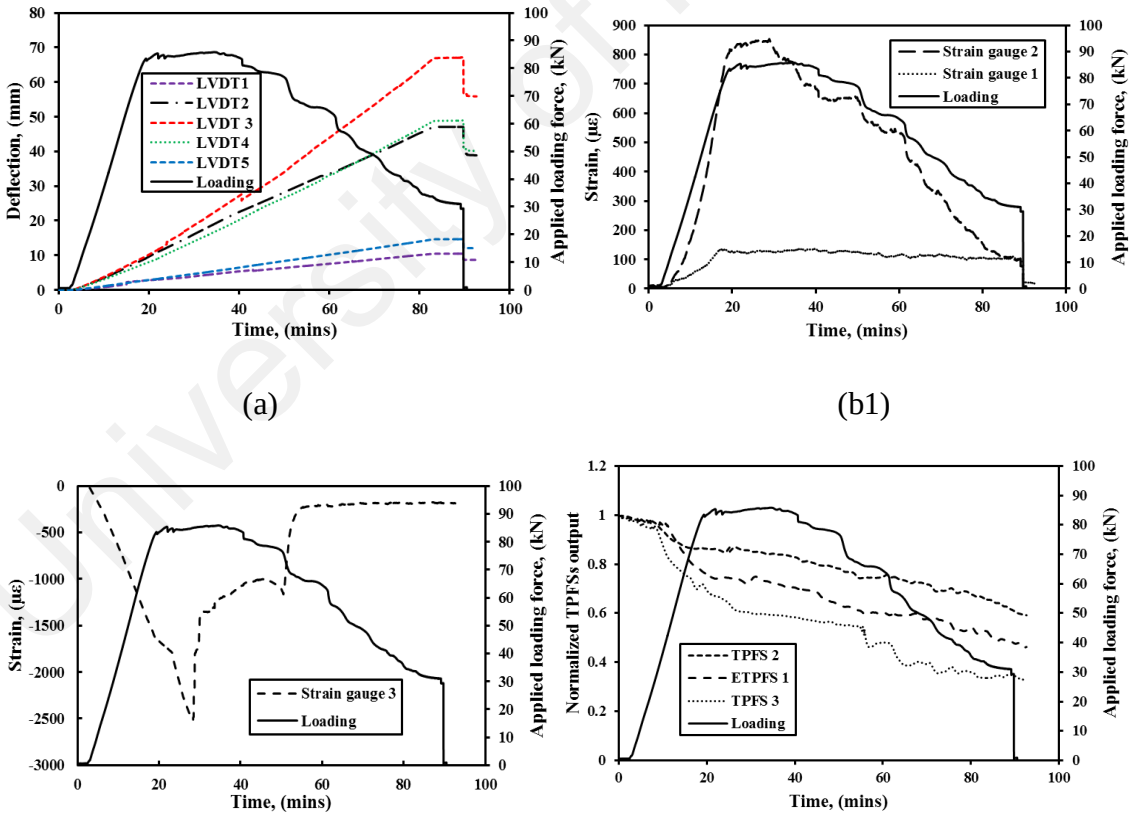

Fig. 5.15: The health monitoring of the full-scale reinforced CB during the loading test, (a) the beam deflection monitored by the LVDTs, (b) the beam strain monitored by the strain gauges, (c) the strains and cracks detected by the TPFSs.

Fig. 5.15 (c) shows the loading force trace and its corresponding TPFS responses. The initial cracks emerged on the CB when the loading force was beyond 16.3 kN. The beam deflection can be observed in Fig. 5.15 (c) where the normalized the TPFS output decreases with the increase of the loading force from 0.02 kN to 16.3 kN. Further increment at the loading force resulted in the output of the TPFSs' sharp decreases. Then, almost-linear responses corresponding to the loading force were exhibited on the TPFSs. It is important to note that the response of TPFS 3 fluctuated after 53 minutes; however, this fluctuation is still following the trend of the loading force, as shown in Fig. 5.15 (c). It is reasonable to expect this result because at this stage the TPFS is tightly attached to the CB and spanned through the crack. The crack width is varied with the change of loading force, which induces the loading force propagating into the TPFS immediately. However, such fluctuation is not observed in the other two TPFSs because the width of the crack at the bottom of the CB is large. The loading force cannot perturb the ETPFS immediately due to the small crack width at this stage. Furthermore, from the observation of TPFS 3, it is concluded that it is necessary to study its ability for postcrack detection, especially in the monitoring of the large width of the crack.

5.4.2.3 Postcrack detection using different installation methods

The installation method of TPFSs for postcrack detection is tested by attaching two TPFSs on the surface of the CB after the crack occurred. The configuration of the TPFS installation is shown in Fig. 5.16 (a). As shown in this figure, one TPFS (TPFS1) is installed on the bottom surface of the CB, and the other (TPFS2) is on the side surface of the CB. The installation positions of TPFSs predict that TPFS1 has a better crack

sensing ability than TPFS2 due to the fact the crack first occurred at the bottom of the CB if the loading force was applied on top of the CB. The TPFS responses with the loading force history are shown in Fig. 5.16 (b). In this figure, it can be observed that the outputs of the TPFSs decreased with the increase of the loading force at a range of 0 to 20 kN, and then it dropped sharply when the loading force reached 20 kN. When the width of the crack is enlarged at such loading force, this sharp drops of the TPFS output may be caused by the reduction of the fiber diameter. The loading force continues to increase from 20 to 60 kN, whereas the output of TPFS1 is decreasing linearly. However, the output of TPFS2 seems not to function at this loading force range. It may be due to the fact that the crack line did not happen at the sensing region of TPFS2 on the CB surface. After that, the responses of the TPFSs reflect well the change of the loading force—i.e., the output of the TPFSs decreases with the increase of the loading force in the range of 60 kN to a maximum point of 108 kN. Correspondingly, the outputs of the two TPFSs agreed well in the whole loading force range—as such, a higher sensitivity can be observed for TPFS1 because TPFS1 has a sharper gradient in output. From this study, it is found that proper packaging of the TPFSs is necessary to avoid the loading force propagating onto the TPFS. Immediately for postcrack monitoring, the TPFS should be installed on the bottom surface of the CB for a great achievement in sensitivity. The proper packaging TPFS for crack detection will be investigated in a future study.

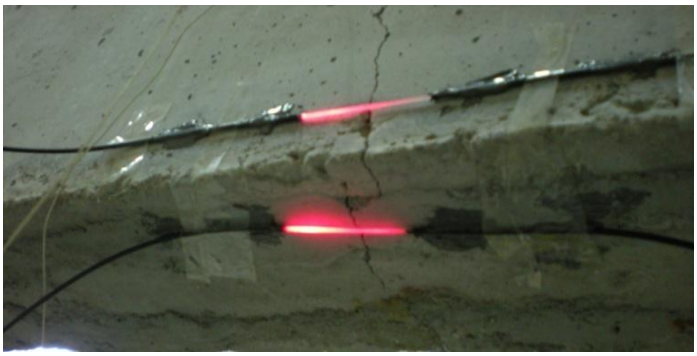

(a)

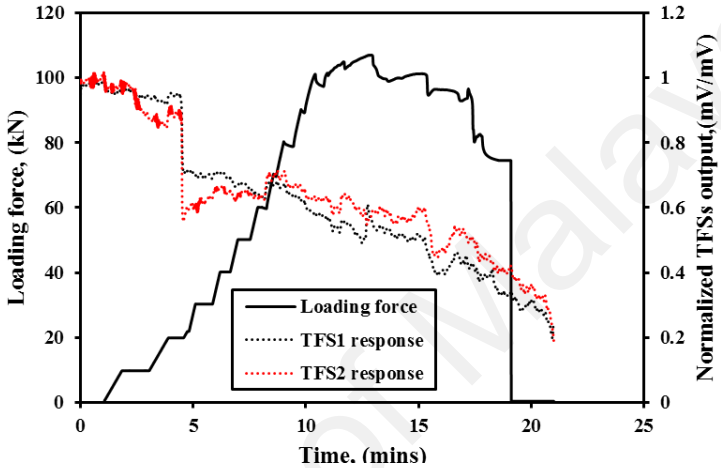

(b)

Fig. 5.16: Postcrack detection using TPFSs on full-scale reinforced CB 2, (a) TPFS installation, (b) TPFS responses with the loading force history.

5.4.3 Sensor drift study

The system drift was studied by employing the measurement system to detect the received light intensity, in which the light is passing through a POF without tapering. On top of this, the room temperature was also monitored by using a thermocouple. This study was performed for 48 hours, and a maximum drift of ~2% and 1.0 ℃ was found for light intensity and room temperature, respectively. On the other hand, the temperature drift can be obtained from Fig. 4.8. As shown in this figure, the initial temperature (start point) and final temperature (stable point) have almost the same value of 25 ℃, if compared at the curve of the thermocouple carefully. It is an indication that

the experimental works are under a very well-controlled ambient condition. However, these two points in the curve of the tapered fiber sensor do not agreed well; it differ by a value of 0.05mV/mV corresponding to a 1.8℃ drift. This temperature drift may be caused by the effects described above.

5.5 Summary

In summary of this chapter, the TPFSs are employed to study the early-age hydration process of cement paste, the vibration monitoring, and the crack detection in CBs. An integrated monitoring system is built in which many TPFSs are multiplexing. The hydration process monitoring is described briefly since it was fully explored in previous chapters. A simple crack detection principle is given by employing the V-number theory. In the study of vibration detection, the responses of the TPFSs are calibrated by using the accelerometers. Three different installation methods of the TPFSs were studied, and the experimental results showed that the embedded TPFSs give the best performance. However, gluing the TPFSs on the surface of the CB also provides acceptable results. This study proves that the installation of the TPFSs is flexible for the structure. Three TPFSs with various tapering diameters were studied. The findings show that a smaller diameter of TPFS gives a better frequency response. Five accelerometers and seven TPFSs were used, and the results showed that the TPFS have the ability to detect the natural frequency of the CB. In addition, the natural frequencies shift, indicating the damage occurred on the CB also found by employing the accelerometers and TPFSs. The capability of the TPFSs for crack detection was

studied in the scale-model CBs and full reinforced CBs. The beam deflection was monitored by using the LVDTs, and the strain of the CB was detected by employing the electrical strain gauges. The results found that the TPFSs have the ability to detect the crack on the scale-model CB, deflecting the crack on the full-scale reinforced CBs. The installation of the TPFSs for postcrack monitoring was also studied, and the results showed that the bottom-surface installation provides a better sensitivity for the beam crack detection. The sensor drift study was carried in the last section. The characteristics of TPFSs make it an ideal alternative for the application of structural health monitoring in the civil engineering.

CHAPTER 6

CONCLUSIONS AND FURTHER WORK

6.1 Conclusions

In this thesis, the performances of the TPFSs on the monitoring of the early-age hydration process in cement paste, detection of vibration, and crack in a concrete beam were assessed. Initially, the geometries of a TPFS are optimized theoretically from its taper ratio, taper length, and the incident ray launch angle. Then, the optimized TPFS is used to study the cement paste during early-age curing. It is influenced by various specimen sizes, water/cement ratios, and different ambient temperatures. Finally, several experiments were carried out using the optimized TPFSs in the detection of vibration and crack of the concrete beam. The conclusions can be derived from the work presented in this thesis. These conclusions are presented following the research objectives.

1) Two TPFSs systems were validated for monitoring the hydration process of cement paste and detecting the vibration and crack in a concrete beam. First, the hydration process measurement system was proposed by using a He-Ne laser, a silicon photodetector, and a lock-in amplifier. An accuracy measurement and an autodata collection are achieved by using this system. This experimental setup is described in Chapter 3. The vibration and crack detection system was described in Chapter 5. A multiplexing TPFSs system is built by employing a DC power supply to drive the

LED (red light, centred at 660 nm), which is acting as the light sources. The high-speed photologic detectors are employed to detect the received light intensity and convert it as voltage signals. The voltage signals are collected by a TDS-530 for temperature and static strain monitoring, or by an IMC data logger (Model D5335) for vibration detection.

2) A low-cost TPFS was fabricated and proposed to monitor the curing temperature of cement paste. Theoretically, a simple sensing principle of the TPFS is carried out based on the analysis for the modes of leaky ray which was perturbed by the surrounding temperature. Results of theoretical analysis show that the number of leaky ray modes increases with the increase of temperature. Furthermore, a mathematical model based on ray-tracing theory is employed to optimize the configuration of the TPFS, such as taper length, taper ratio, and launch angle of the initial ray. The numerical results show that the sensitivity of the proposed sensor is strongly governed by the strength of EW since the strength of the EW is mainly contributed by the power of the tunnelling ray. In the experiment works, two sets of sensor configurations were carried out, which included tapered fibers with stripped lengths of 2, 4, and 6 cm with a diameter of 480 μm and a stripped length of 6 cm with diameters of 240, 480, and 600 μm. Theoretical and experimental results agreed with each other, and it was found that higher temperature sensitivity of the TPFS can be achieved by combining a longer taper length and a lower taper ratio with the initial ray launch angle of 0.01 rad. The sensor characteristics were determined and calibrated by an embedded thermocouple.

3) The hydration process of cement paste is studied to determine its setting time by using the FBG and TPFSs where both were embedded into the host specimen respectively in Chapter 4. The FBG has a sensitivity of 9pm/℃ in both increase/decrease temperature in the temperature calibration range of 25 ℃ to 105 ℃. The experimental results demonstrate that the FBG is a good alternative for the measurement of early-age curing temperature of cement paste.

4) The optimized TPFSs are applied to study the cement paste early-age curing influenced by various specimen sizes, water/cement ratios, and different ambient temperatures. The hydration process of cement paste is predicted from the monitored information of temperature, experimentally. The experimental results showed that the curing temperature rises with the increasing size of the mould, decreasing of w/c ratio, and increasing ambient temperature. The setting time is shortened by a smaller size of the specimen, lower w/c ratio, and higher ambient temperature. The experimental results show that the proposed sensor has the ability to find the setting time of cement paste since the setting process is accompanied by the temperature change of cement paste.

5) In chapter 5, vibration and crack monitoring are studied in the cured concrete beam by using the TPFSs. For vibration detection, three different installation methods of the TPFSs were studied, and the experimental results showed that the embedded TPFSs gave the best performance and that gluing the TPFSs on the surface of CB also provide acceptable results. The experimental results showed that the small diameter of the TPFS provides a good frequency response. The experimental results also demonstrated that the accelerometer and TPFSs have the ability to detect the

natural frequency of the CB. Besides, the natural frequencies shift, indicating the damage occurred on the CB is also proved by employing the accelerometers and TPFSs.

6) In the study of crack detection using the TPFSs, the beam deflection was monitored by using the LVDTs, and the strain of the CB was detected by employing the electrical strain gauges. The experimental results found that the TPFSs have the ability to detection the crack on the scale model CB and deflection and the crack on the full-scale reinforced CBs. The installation methods of the TPFSs for postcrack detection are experimentally studied, finding that the bottom-surface installation provides a better sensitivity for the beam crack detection. The sensor drift study is carried out in the last section.

6.2 Recommendation for further work

The TPFS used in this work is fabricated by tapering the plastic optical fiber by stripping the cladding. This fabrication approach makes the fiber core exposure to the surrounding medium immediately. There are many advantages inherited by TPFSs, such as low cost and high performance, and the performance of this sensor is highly acceptable in the laboratory condition; therefore, applying this sensor in the field test is highly desired and has a greater potential to be discovered and improved. As such, future researches should be carried out by the following points and guidelines:

1) To improve the fabrication method of the TPFS, such as tapering the optical fiber without stripping the cladding by using the flame-flush method.
2) For the vibration detection, including the crack location and crack width, employing

the TPFSs is desired by monitoring the natural frequencies and mode shapes of a CB.

3) Future research could carry out to improve the detection method of a transmission light signal, such as inscribing the FBG on the plastic optical fiber to discriminate the detected light intensity loss from the optical spectrum.

REFERENCES

Adeli, H., & Jiang, X. (2006). Dynamic fuzzy wavelet neural network model for structural system identification. *Journal of Structural Engineering, 132*(1), 102-111.

Afromowitz, M. A. (1988). Fiber optic polymer cure sensor. *Lightwave Technology, Journal of, 6*(10), 1591-1594.

Ahmad, M., Chang, K. P., King, T., & Hench, L. L. (2005). A compact fiber-based fluorescence sensor. *Sensors and Actuators A: Physical, 119*(1), 84-89.

Albertin, F., Di Vita, P., & Vannucci, R. (1974). Geometrical theory of energy launching and pulse distortion in dielectric optical waveguides. *Optical and Quantum Electronics, 6*(5), 369-386.

Ankiewicz, A., & Pask, C. (1977). Geometric optics approach to light acceptance and propagation in graded index fibers. *Optical and Quantum Electronics, 9*(2), 87-109.

Ansari, F. (2003). Fiber optic health monitoring of civil structures. *Proceedings of the First Structural Health Monitoring and Intelligent Infrastructure*, 19-30.

Ansari, F., & Navalurkar, R. K. (1993). Kinematics of crack formation in cementitious composites by fiber optics. *Journal of Engineering Mechanics, 119*(5), 1048-1061.

Antunes, P., Lima, H., Varum, H., & Andr é, P. (2012). Optical fiber sensors for static and dynamic health monitoring of civil engineering infrastructures: Abode wall

case study. *Measurement, 45(7)*, 1695-1705.

Bakhshi, M., Mobasher, B., & Zenouzi, M. (2012). Model for Early Age Rate of Evaporation of Cement-Based Materials. *Journal of Engineering Mechanics, 138(11)*, 1372-1380.

Ballim, Y. (2004). A numerical model and associated calorimeter for predicting temperature profiles in mass concrete. *Cement and Concrete Composites, 26*(6), 695-703.

Barrell, K., & Pask, C. (1978). The effect of cladding loss in graded-index fibers. *Optical and Quantum Electronics, 10*(3), 223-231.

Barrell, K., & Pask, C. (1980). Pulse dispersion in optical fibers of arbitrary refractive-index profile. *Applied optics, 19*(8), 1298-1305.

Barrell, K. F., & Pask, C. (1979). Ray launching and observation in graded-index optical fibers. *JOSA, 69*(2), 294-300.

Bayle, J., & Mateo, J. (1996). *Plastic optical fiber sensor of refractive index, based on evanescent field.* Paper presented at the Proceedings of the Fifth International Conference on Plastic Optical Fibers and Applications—POF.

Bhalla, S., & Soh, C. K. (2004). Structural health monitoring by piezo-impedance transducers. II: Applications. *Journal of Aerospace Engineering, 17*(4), 166-175.

Bløtekjær, K. (1993). Strain distribution and optical propagation in tension-coiled fibers. *Optics letters, 18*(13), 1059-1061.

Bocca, M., Eriksson, L. M., Mahmood, A., Jäntti, R., & Kullaa, J. (2011). A synchronized wireless sensor network for experimental modal analysis in structural health monitoring. *Computer - Aided Civil and Infrastructure*

Engineering, 26(7), 483-499.

Bushnell-Watson, S., & Sharp, J. (1990). Further studies of the effect of temperature upon the setting behaviour of refractory calcium aluminate cements. *Cement and Concrete Research, 20*(4), 623-635.

Bushnell-Watson, S., & Sharp, J. (1990). On the cause of the anomalous setting behaviour with respect to temperature of calcium aluminate cements. *Cement and Concrete Research, 20*(5), 677-686.

Bushnell-Watson, S. M., & Sharp, J. (1986). The effect of temperature upon the setting behaviour of refractory calcium aluminate cements. *Cement and Concrete Research, 16*(6), 875-884.

Carleson, R. W. (1937). *A simple method for the computation of temperatures in concrete structures. Journal Proceedings, 34(11),* 89-104.

Chen, B., & Liu, W. (2010). Mobile agent computing paradigm for building a flexible structural health monitoring sensor network. *Computer‐Aided Civil and Infrastructure Engineering, 25*(7), 504-516.

Chen, Y. C., Chen, L. W., & Chen, P. C. (2005). Combined effects of bending and elongation on polymer optical fiber losses. *Optics letters, 30*(3), 230-232.

Chiang, C. C. Curing Monitoring of Composite Material Using Embedded Fiber Bragg Grating Sensors.

Childs, P., Wong, A. C. L., Terry, W., & Peng, G. (2008). Measurement of crack formation in concrete using embedded optical fiber sensors and differential strain analysis. *Measurement science and technology, 19*(6), 1305-1311.

Cook, R. O., & Hamm, C. W. (1979). Fiber optic lever displacement transducer. *Appl.*

Opt., 18(19), 3230-3241.

Cyr, M., & Tagnit-Hamou, A. (2001). Particle size distribution of fine powders by LASER diffraction spectrometry. Case of cementitious materials. *Materials and Structures, 34*(6), 342-350.

Dare, P., Hanley, H., Fraser, C., Riedel, B., & Niemeier, W. (2002). An operational application of automatic feature extraction: the measurement of cracks in concrete structures. *The Photogrammetric Record, 17*(99), 453-464.

Daum, W., Hoffman, A., Strecker, U., Brockmeyer, A., & Weinert, A. (1994). *Influence of chemicals on the durability of polymer optical fibers.* Paper presented at the Proceedings of the 3rd International Conference on Plastic Optical Fibers, Yokohama, 111-114.

Davis, M., Kersey, A., Sirkis, J., & Friebele, E. (1999). Shape and vibration mode sensing using a fiber optic Bragg grating array. *Smart materials and structures, 5*(6), 759-765.

De Oliveira, R., Ramos, C., & Marques, A. (2008). Health monitoring of composite structures by embedded FBG and interferometric Fabry–Pérot sensors. *Computers & structures, 86*(3), 340-346.

Dong-Sheng, X., Jian-Hua, Y., Zhen-Zhong, C., Yun-Long, W., Hong-Hu, Z., & Hua-Fu, P. (2013). A New Flexible FBG Sensing Beam for Measuring Dynamic Lateral Displacements of Soil in a Shaking Table Test. Measurement, 46(1), 200-209.

Emborg, M., & Bernander, S. (1994). Assessment of risk of thermal cracking in hardening concrete. *Journal of Structural Engineering, 120*(10), 2893-2912.

Emslie, C. (1988). Polymer optical fibers. *Journal of materials science, 23*(7), 2281-2293.

Escalante-Garcia, J., & Sharp, J. (1998). Effect of temperature on the hydration of the main clinker phases in Portland cements: Part I, neat cements. *Cement and Concrete Research, 28*(9), 1245-1257.

Escalante-Garcıa, J., & Sharp, J. (2001). The microstructure and mechanical properties of blended cements hydrated at various temperatures. *Cement and Concrete Research, 31*(5), 695-702.

Fan, S., & Hanson, J. M. (1998). Effect of alkali silica reaction expansion and cracking on structural behavior of reinforced concrete beams. *ACI Structural Journal, 95*, 498-505.

Farrar, C. R., Duffey, T., Cornwell, P. J., & Doebling, S. W. (1999). *Excitation methods for bridge structures.* Paper presented at the Society for Experimental Mechanics, Inc, 17 th International Modal Analysis Conference.

Ferreira, L., Antunes, P., Domingues, F., Silva, P., & Andr é, P. (2012). Monitoring of sea bed level changes in nearshore regions using fiber optic sensors. *Measurement, 45(6)*, 1527-1533.

Fournier, B., & Berube, M. A. (2000). Alkali-aggregate reaction in concrete: a review of basic concepts and engineering implications. *Canadian Journal of Civil Engineering, 27*(2), 167-191.

Frieden, J., Cugnoni, J., Botsis, J., Gmür, T., & Ćorić, D. (2010). High-speed internal strain measurements in composite structures under dynamic load using embedded FBG sensors. *Composite Structures, 92*(8), 1905-1912.

Fujita, Y., Mitani, Y., & Hamamoto, Y. (2006). *A method for crack detection on a concrete structure*. Paper presented at the Pattern Recognition, 2006. ICPR 2006..

Garboczi, E., & Bentz, D. (1992). *Computer-based models of the microstructure and properties of cement-based materials.* Paper presented at the 9th International Cement Chemistry Congress, New Delhi, India.

Ghosh, A. (2003). *Advances in cement technology: chemistry, manufacture and testing*: Taylor & Francis.

Glišić, B., & Simon, N. (2000). Monitoring of concrete at very early age using stiff SOFO sensor. *Cement and Concrete Composites, 22*(2), 115-119.

Gloge, D. (1975). Propagation effects in optical fibers. *Microwave Theory and Techniques, IEEE Transactions on, 23*(1), 106-120.

Gu, H., Song, G., Dhonde, H., Mo, Y., & Yan, S. (2006). Concrete early-age strength monitoring using embedded piezoelectric transducers. *Smart materials and structures, 15*(6), 1837.

Gu, X., Chen, Z., & Ansari, F. (2000). Embedded fiber optic crack sensor for reinforced concrete structures. *ACI Structural Journal, 97*(3).

Guerrero, H., Zoido, J., Escudero, J., & Bernabeu, E. (1993). Characterization and sensor applications of polycarbonate optical fibers. *Fiber & Integrated Optics, 12*(3), 257-268.

Guo, S., & Albin, S. (2003). Transmission property and evanescent wave absorption of cladded multimode fiber tapers. *Optics express, 11*(3), 215-223.

Hanna, A. N. (2003). Aggregate tests for Portland cement concrete pavements: review

and recommendations. *NCHRP Research Results Digest*(281).

Housner, G. W., Bergman, L. A., Caughey, T., Chassiakos, A., Claus, R., Masri, S., Yao, J. (1997). Structural control: past, present, and future. *Journal of Engineering Mechanics, 123*(9), 897-971.

Jackson, J. D., & Fox, R. F. (1999). Classical electrodynamics. *American Journal of Physics, 67*, 841.

Jiang, C., Kuzyk, M. G., Ding, J. L., Johns, W. E., & Welker, D. J. (2002). Fabrication and mechanical behavior of dye-doped polymer optical fiber. *Journal of applied physics, 92*(1), 4-12.

Jiang, X., & Adeli, H. (2005). Dynamic wavelet neural network for nonlinear identification of highrise buildings. *Computer‐Aided Civil and Infrastructure Engineering, 20*(5), 316-330.

Jiurong, C. (1998). Polymeric Optical Fibers Materials [J]. *NEW CHEMICAL MATERIALS, 8*.

Kaino, T. (1985). Absorption losses of low loss plastic optical fibers. *Jpn. J. Appl. Phys. 1, 24*(12), 1661-1665.

Kang, L. H., Kim, D. K., & Han, J. H. (2007). Estimation of dynamic structural displacements using fiber Bragg grating strain sensors. *Journal of Sound and Vibration, 305*(3), 534-542.

Kiesel, S., Peters, K., Hassan, T., & Kowalsky, M. (2007). Behaviour of intrinsic polymer optical fiber sensor for large-strain applications. *Measurement Science and Technology, 18*(10), 3144.

Kim, B., & Weiss, W. J. (2003). Using acoustic emission to quantify damage in

restrained fiber-reinforced cement mortars. *Cement and Concrete Research, 33*(2), 207-214.

Kishi, T., & Maekawa, K. (1995). *Thermal and mechanical modelling of young concrete based on hydration process of multi-component cement minerals.* Paper presented at the RILEM PROCEEDINGS.

Komonen, J., & Penttala, V. (2003). Effects of high temperature on the pore structure and strength of plain and polypropylene fiber reinforced cement pastes. *Fire technology, 39*(1), 23-34.

Kuang, K., & Cantwell, W. (2003). The use of plastic optical fibers and shape memory alloys for damage assessment and damping control in composite materials. *Measurement Science and Technology, 14*(8), 1305.

Kuang, K., Cantwell, W., & Thomas, C. (2003). Crack detection and vertical deflection monitoring in concrete beams using plastic optical fiber sensors. *Measurement Science and Technology, 14*(2), 205-211.

Kuang, K., Quek, S., & Cantwell, W. (2004). Use of polymer-based sensors for monitoring the static and dynamic response of a cantilever composite beam. *Journal of materials science, 39*(11), 3839-3843.

Kuang, K., Quek, S., & Maalej, M. (2004). Assessment of an extrinsic polymer-based optical fiber sensor for structural health monitoring. *Measurement Science and Technology, 15*(10), 2133.

Kuang, K. S. C., Cantwell, W. J., & Scully, P. J. (2002). An evaluation of a novel plastic optical fiber sensor for axial strain and bend measurements. *Measurement Science and Technology, 13*(10), 1523.

Kuzyk, M., Paek, U., & Dirk, C. (1991). Guest‐host polymer fibers for nonlinear optics. *Applied physics letters, 59*(8), 902-904.

Kuzyk, M. G. (2006). *Polymer fiber optics: materials, physics, and applications* (Vol. 117): CRC.

Lai, C. W., Lo, Y. L., Yur, J. P., Liu, W. F., & Chuang, C. H. (2011). Application of Fabry-Pérot and fiber Bragg grating pressure sensors to simultaneous measurement of liquid level and specific gravity. *Measurement*.

Li, B., Chen, X., Ma, J., & He, Z. (2005). Detection of crack location and size in structures using wavelet finite element methods. *Journal of Sound and Vibration, 285*(4), 767-782.

Li, H., Huang, Y., Chen, W., Ma, M., Tao, D., & Ou, J. (2011). Estimation and Warning of Fatigue Damage of FRP Stay Cables Based on Acoustic Emission Techniques and Fractal Theory. *Computer‐Aided Civil and Infrastructure Engineering, 26*(7), 500-512.

Li, Q., Li, G., & Wang, G. (2003). Effect of the plastic coating on strain measurement of concrete by fiber optic sensor. *Measurement, 34*(3), 215-227.

Li, Q., Li, G., & Yuan, L. (2004). Calibration of embedded fiber optic sensor in concrete under biaxial compression. *Measurement, 35*(3), 303-310.

Lin, S. K., Huang, C. H., Chang, C. S., Yen, T., Wu, C. H., & Lin, Y. (2010). Simultaneous Measurement of Deformation and Temperature of High-Strength Concrete at very Early Age to Determine the Initial and the Finial Setting Time. *Journal of Marine Science and Technology, 18*(2), 284-289.

Ling, H. Y., Lau, K. T., & Cheng, L. (2004). Determination of dynamic strain profile

and delamination detection of composite structures using embedded multiplexed fiber-optic sensors. *Composite Structures, 66*(1), 317-326.

Linvill, D. E. (1990). Calculating chilling hours and chill units from daily maximum and minimum temperature observations. *HortScience, 25*(1), 14-16.

Liu, J. G., Schmidt-Hattenberger, C., & Borm, G. (2002). Dynamic strain measurement with a fiber Bragg grating sensor system. *Measurement, 32*(2), 151-161.

Loo, Y., Peterson, J., Swaddiwudhipong, S., & Tam, C. (1995). Application of the layering method on large concrete pours. *Magazine of Concrete Research, 47*(172), 209-217.

Lothenbach, B., Winnefeld, F., Alder, C., Wieland, E., & Lunk, P. (2007). Effect of temperature on the pore solution, microstructure and hydration products of Portland cement pastes. *Cement and Concrete Research, 37*(4), 483-491.

Love, J., Pask, C., & Winkler, C. (1979). Rays and modes on step-index multimode elliptical waveguides. *Microwaves, Optics and Acoustics, IEE Journal on, 3*(6), 231-238.

Love, J., & Winkler, C. (1978). Power attenuation in bent multimode step-index slab and fiber waveguides. *Electronics Letters, 14*, 32-34.

Love, J. D., & Winkler, C. (1977). Attenuation and tunnelling coefficients for leaky rays in multilayered optical waveguides. *JOSA, 67*(12), 1627-1633.

Love, J. D., & Winkler, C. (1978). Refracting leaky rays in graded-index fibers. *Applied optics, 17*(14), 2205-2208.

Love, J. D., & Winkler, C. (1978). A universal tunnelling coefficient for step-and graded-index multimode fibers. *Optical and Quantum Electronics, 10*(4),

341-351.

Lu, H., Swaddiwudhipong, S., & Wee, T. (2000). Evaluation of internal restrained strain in concrete members at early age. *ACI Materials Journal, 97*(5).

Maeck, J., Abdel Wahab, M., Peeters, B., De Roeck, G., De Visscher, J., De Wilde, W., Vantomme, J. (2000). Damage identification in reinforced concrete structures by dynamic stiffness determination. *Engineering structures, 22*(10), 1339-1349.

Mangold, M., & Springenschmid, R. (1994). Why are Temperature-Related Criteria so Undependahle to Predict Thermal Cracking at Early Ages. *Thermal Cracking in Concrete at Early Ages (editor R. Springenschmid), Chapman & Hall*.

Marcatili, E. (1977). Modal dispersion in optical fibers with arbitrary numerical aperture and profile dispersion. *Bell Syst. Tech. J, 56*, 49-63.

Merchant, D., Scully, P., & Schmitt, N. (1999). Chemical tapering of polymer optical fiber. *Sensors and Actuators A: Physical, 76*(1), 365-371.

Moaveni, B., He, X., Conte, J. P., & De Callafon, R. A. (2008). Damage identification of a composite beam using finite element model updating. *Computer‐Aided Civil and Infrastructure Engineering, 23*(5), 339-359.

Mueller, U. C., Baier, H., Zeh, T., Mueller, M. S., & Koch, A. W. (2010). Vibration and shape control in opto-mechanical systems using distributed fiber-optic bragg grating sensors. *Journal of Vibration and Control, 16*(4), 539-553.

Mufti, A. (2003). Integration of sensing in civil structures: development of the new discipline of civionics. *Structural Health Monitoring and Intelligent Infrastructure, 1*, 119-129.

Muralidharan, S., Ha, T. H., Bae, J. H., Ha, Y. C., Lee, H. G., & Kim, D. K. (2007). A

promising potential embeddable sensor for corrosion monitoring application in concrete structures. *Measurement, 40*(6), 600-606.

Murukeshan, V., Chan, P., Ong, L., & Seah, L. (2000). Cure monitoring of smart composites using fiber Bragg grating based embedded sensors. *Sensors and Actuators A: Physical, 79*(2), 153-161.

Nakamura, K., Husdi, I. R., & Ueha, S. (2005). *A distributed strain sensor with the memory effect based on the POF OTDR.* Paper presented at the Bruges, Belgium-Deadline Past.

Ndambi, J. M., Vantomme, J., & Harri, K. (2002). Damage assessment in reinforced concrete beams using eigen-frequencies and mode shape derivatives. *Engineering structures, 24*(4), 501-515.

Neville, A. M. (1995). *Properties of concrete*.

Neville, A. M., & Brooks, J. J. (1987). *Concrete technology*.

Newland, D. E. (1993). Harmonic wavelet analysis. *Proceedings of the Royal Society of London. Series A: Mathematical and Physical Sciences, 443*(1917), 203-225.

Ni, Y., Wong, K., & Xia, Y. (2011). Health checks through landmark bridges to sky-high structures. *Advances in Structural Engineering, 14*(1), 103-119.

Nishio, M., Mizutani, T., & Takeda, N. (2010). Structural shape reconstruction with consideration of the reliability of distributed strain data from a Brillouin-scattering-based optical fiber sensor. *Smart materials and structures, 19*(3), 035011.

Okabe, Y., Yashiro, S., Tsuji, R., Mizutani, T., & Takeda, N. (2002). Effect of thermal residual stress on the reflection spectrum from fiber Bragg grating sensors

embedded in CFRP laminates. *Composites Part A: Applied Science and Manufacturing, 33*(7), 991-999.

Park, H., Lee, H., Adeli, H., & Lee, I. (2006). A new approach for health monitoring of structures: terrestrial laser scanning. *Computer‐Aided Civil and Infrastructure Engineering, 22*(1), 19-30.

Pask, C., & Snyder, A. W. (1974). Illumination of multimode optical fibersleaky ray analysis. *Optical and Quantum Electronics, 6*(4), 297-304.

Peng, G. D., Chu, P., Xiong, Z., Whitbread, T. W., & Chaplin, R. P. (1996). Dye-doped step-index polymer optical fiber for broadband optical amplification. *Lightwave Technology, Journal of, 14*(10), 2215-2223.

Pollock, C. R. (1995). *Fundamentals of optoelectronics*: Irwin Chicago.

Price, W. H. (1951). *Factors influencing concrete strength.* Paper presented at the ACI Journal Proceedings.

Quinn, W., Angove, P., Buckley, J., Barrett, J., & Kelly, G. (2011). Design and performance analysis of an embedded wireless sensor for monitoring concrete curing and structural health. *Journal of Civil Structural Health Monitoring, 1*(1-2), 47-59.

Rastogi, P. K. (1997). *Optical Measurement Techniques and Applications*: Artech House.

Ravina, D., & Shalon, R. (1968). *Plastic shrinkage cracking.* Paper presented at the ACI Journal Proceedings.

Rawson, E. G., Herriott, D., & McKenna, J. (1970). Analysis of refractive index distributions in cylindrical, graded-index glass rods (GRIN rods) used as image

relays. *Applied optics, 9*(3), 753-759.

Remouche, M., Mokdad, R., Chakari, A., & Meyrueis, P. (2007). Intrinsic integrated optical temperature sensor based on waveguide bend loss. *Optics & Laser Technology, 39*(7), 1454-1460.

Ren, L., Song, G., Conditt, M., Noble, P. C., & Li, H. (2007). Fiber Bragg grating displacement sensor for movement measurement of tendons and ligaments. *Applied optics, 46*(28), 6867-6871.

Rubinsky, I. A. (1954). Heat of hydration in concrete. *Magazine of Concrete Research, 6*(17), 79-92.

Sato, M., Ishigure, T., & Koike, Y. (2000). Thermally stable high-bandwidth graded-index polymer optical fiber. *Journal of lightwave technology, 18*(7), 952.

Silva-López, M., Fender, A., MacPherson, W. N., Barton, J. S., Jones, J. D. C., Zhao, D., Bennion, I. (2005). Strain and temperature sensitivity of a single-mode polymer optical fiber. *Opt. Lett., 30*(23), 3129-3131.

Slowik, V., & Ju, J. (2011). Discrete modeling of plastic cement paste subjected to drying. *Cement and Concrete Composites, 33*(9), 925-935.

Slowik, V., Schlattner, E., & Klink, T. (2004). Experimental investigation into early age shrinkage of cement paste by using fiber Bragg gratings. *Cement and Concrete Composites, 26*(5), 473-479.

Snyder, A., & Love, J. (1976). Attenuation coefficient for rays in graded fibers with absorbing cladding. *Electronics Letters, 12*(10), 255-257.

Snyder, A., & Mitchell, D. (1974). Bending losses of multimode optical fibers. *Electronics Letters, 10*(1), 11-12.

Snyder, A. W. (1974). Leaky-ray theory of optical waveguides of circular cross section. *Applied Physics A: Materials Science & Processing*, *4*(4), 273-298.

Snyder, A. W., & Love, J. (1983). *Optical waveguide theory* (Vol. 190): Springer.

Sohn, H. G., Lim, Y. M., Yun, K. H., & Kim, G. H. (2005). Monitoring crack changes in concrete structures. *Computer‐Aided Civil and Infrastructure Engineering*, *20*(1), 52-61.

Song, G., Gu, H., Mo, Y., Hsu, T., & Dhonde, H. (2007). Concrete structural health monitoring using embedded piezoceramic transducers. *Smart Materials and Structures*, *16*(4), 959.

Springenschmid, R. (1995). *Thermal Cracking in Concrete at Early Ages: Proceedings of the International Symposium Held by RILEM... at the Technical University of Munich and Organized by RILEM Technical Committee 119 and the Institute of Building Materials of the Technical University of Munich, Germany... Munich, October 10-12, 1994*: E & FN Spon.

Springenschmid, R. (1998). *Prevention of Thermal Cracking in Concrete at Early Ages: State-of-the-art Report Prepared by RILEM Technical Committee 119, Avoidance of Thermal Cracking in Concrete at Early Ages*: E & FN Spon.

Sun, K., & Kapoor, R. (2008). *Optimum taper length for maximum fluorescence signal from an evanescent wave fiber optic biosensor*. Paper presented at the Proc. SPIE.

Sun, R., & Oyadiji, S. O. (2007). *Assessment of a Plastic Optic Fiber Sensor for the Measurement of Static and Dynamic Strains*.

Szczurowski, M. K., Martynkien, T., Statkiewicz-Barabach, G., Urbanczyk, W., Khan,

L., & Webb, D. J. (2010). Measurements of stress-optic coefficient in polymer optical fibers. *Optics letters, 35*(12), 2013-2015.

Takeda, N. (2002). Characterization of microscopic damage in composite laminates and real-time monitoring by embedded optical fiber sensors. *International Journal of Fatigue, 24*(2), 281-289.

Tam, C., Swaddiwudhipong, S., Mani, A., & Lee, S. (1993). Concreting of Thick Sections in the Tropics. *ACI SPECIAL PUBLICATIONS, 139*, 143-143.

Tan, Y., Meng, L., & Zhang, D. (2012). Strain Sensing Characteristic of Ultrasonic Excitation-Fiber Bragg Gratings Damage Detection Technique. *Measurement*.

Thomas, J.J., & Jenning, H.M. (2008). "The Science of Concrete", Retrieved 15 August 2008, from http://iti.northwestern.edu/cement/index.html.

Thurston, S., Priestley, M., & Cdoke, N. (1980). *Thermal analysis of thick concrete sections.* Paper presented at the ACI Journal Proceedings.

Tian, B., & Cohen, M. D. (2000). Does gypsum formation during sulfate attack on concrete lead to expansion? *Cement and Concrete Research, 30*(1), 117-123.

Ueba, Y., & Miyake, S. (1985). Plastic optical fibers: Google Patents.

Ulrich, R., Rashleigh, S., & Eickhoff, W. (1980). Bending-induced birefringence in single-mode fibers. *Optics letters, 5*(6), 273-275.

Umesha, P., Ravichandran, R., & Sivasubramanian, K. (2009). Crack detection and quantification in beams using wavelets. *Computer - Aided Civil and Infrastructure Engineering, 24*(8), 593-607.

Van Breugel, K. (1980). *Artificial cooling of hardening concrete*: Delft University.

Van Breugel, K. (1995). Numerical simulation of hydration and microstructural

development in hardening cement-based materials (I) theory. *Cement and Concrete Research, 25*(2), 319-331.

Voss, K. F., & Wanser, K. H. (1994). *Fiber sensors for monitoring structural strain and cracks.* Paper presented at the PROCEEDINGS-SPIE THE INTERNATIONAL SOCIETY FOR OPTICAL ENGINEERING.

Wan, K. T., & Leung, C. K. Y. (2007). Applications of a distributed fiber optic crack sensor for concrete structures. *Sensors and Actuators A: Physical, 135*(2), 458-464.

Wang, Y., Han, B., Bar-Cohen, A., & Cho, S. (2007). *Fiber Bragg grating sensor to characterize curing process-dependent mechanical properties of polymeric materials.* Paper presented at the Electronic Components and Technology Conference, 1045-1050.

Wilson, J. G., & Gupta, N. K. (2004). Equipment for the investigation of the accelerated curing of concrete using direct electrical conduction. *Measurement, 35*(3), 243-250.

Winkler, C., Love, J., & Ghatak, A. (1979). Loss calculations in bent multimode optical waveguides. *Optical and Quantum Electronics, 11*(2), 173-183.

Wolff, R., & Miesseler, H. J. (1992). *Monitoring of prestressed concrete structures with optical fiber sensors.* Paper presented at the PROCEEDINGS-SPIE THE INTERNATIONAL SOCIETY FOR OPTICAL ENGINEERING.

Wong, A. C. L., Childs, P. A., Berndt, R., Macken, T., Peng, G. D., & Gowripalan, N. (2007). Simultaneous measurement of shrinkage and temperature of reactive powder concrete at early-age using fiber Bragg grating sensors. *Cement and*

Concrete Composites, 29(6), 490-497.

Wu, Z., Xu, B., Hayashi, K., & Machida, A. (2006). Distributed optic fiber sensing for a full-scale PC girder strengthened with prestressed PBO sheets. *Engineering structures, 28*(7), 1049-1059.

Wu, Z., Xu, B., Takahashi, T., & Harada, T. (2008). Performance of a BOTDR optical fiber sensing technique for crack detection in concrete structures. *Structures and Infrastructure Engineering, 4*(4), 311-323.

Xiang, J., Zhong, Y., Chen, X., & He, Z. (2008). Crack detection in a shaft by combination of wavelet-based elements and genetic algorithm. *International Journal of Solids and Structures, 45*(17), 4782-4795.

Xie, F., Zhang, S., Li, Y., & Lee, S. B. (2002). Multiple in-fiber Bragg gratings sensor with a grating scale. *Measurement, 31*(2), 139-142.

Xiong, Z., Peng, G., Wu, B., & Chu, P. (1999). Highly tunable Bragg gratings in single-mode polymer optical fibers. *Photonics Technology Letters, IEEE, 11*(3), 352-354.

Xu, B., Chen, G., & Wu, Z. (2007). Parametric identification for a truss structure using axial strain. *Computer‐Aided Civil and Infrastructure Engineering, 22*(3), 210-222.

Yang, D., Yu, J., Tao, X., & Tam, H. (2004). Structural and mechanical properties of polymeric optical fiber. *Materials Science and Engineering: A, 364*(1), 256-259.

Yang, H., Lim, K., Harun, S., Dimyati, K., & Ahmad, H. (2010). Enhanced bundle fiber displacement sensor based on concave mirror. *Sensors and Actuators A: Physical, 162*(1), 8-12.

Zhang, H., & Wu, Z. (2008). Performance evaluation of BOTDR-based distributed fiber optic sensors for crack monitoring. *Structural Health Monitoring, 7*(2), 143-156.

Zhang, Z., Zhao, P., Lin, P., & Sun, F. (2006). Thermo-optic coefficients of polymers for optical waveguide applications. *Polymer, 47*(14), 4893-4896.

Zhao, Y., & Zhao, M. (2005). Novel force sensor based on a couple of fiber Bragg gratings. *Measurement, 38*(1), 30-33.

Ziemann, O., Daum, W., Bräuer, A., Schlick, J., & Frank, W. (2000). *Results of a German 6.000 hours accelerated Aging Test of PMMA POF and Consequences for the Practical Use of POF*. Paper presented at the Proceedings of the 9th International Conference on Plastic Optical Fibers, Boston.

Zinin, P., Manghnani, M., Wang, Y., & Livingston, R. (2000). Detection of cracks in concrete composites using acoustic microscopy. *NDT & E International, 33*(5), 283-287.

ZOIDO, H. G. G. V. G. J. (1998). Mechanical properties of polycarbonate optical fibers. *Fiber & Integrated Optics, 17*(3), 231-242.

Zou, X., Chao, A., Tian, Y., Wu, N., Zhang, H., Yu, T. Y., & Wang, X. (2012). An experimental study on the concrete hydration process using Fabry–Perot fiber optic temperature sensors. *Measurement*. 45(5), 1077-1082.

Zubia, J., & Arrue, J. (2001). Plastic optical fibers: An introduction to their technological processes and applications. *Optical Fiber Technology, 7*(2), 101-140.

Zubia, J., Arrue, J., & Mendioroz, A. (1997). Theoretical analysis of the torsion-induced optical effect in a plastic optical fiber. *Optical Fiber Technology, 3*(2), 162-167.

LIST OF PUBLICATIONS

Journal papers

1. Dong Luo, Zainah Ibrahim, Bin Xu, Zubaidah Ismail (2013) Optimization of the Geometries of Biconical Tapered Fiber Sensors for Early-age Curing Temperature Monitoring of Concrete Specimens, *Computer-Aided Civil and Infrastructure Engineering*, vol 28, Issue 7, 531-541.
2. Dong Luo, Zainah Ibrahim, Zubaidah Ismail, The use of tapered fiber sensor to study hydration process of cement paste, *IEEE Sensors Journal*, In press, 2013.
3. Dong Luo, Zainah Ibrahim, Zubaidah Ismail, Added advantages in using a fiber Bragg grating sensor in the determination of early age setting time for cement pastes, *Measurement*, In press, 2013.
4. Dong Luo, Zainah Ibrahim, Zubaidah Ismail, "Using a tapered optical fiber sensor to study the influence of specimen size, water/cement ratio and ambient temperature on the hydration process of mortar paste", Under reviewed by Measurement.

Conference papers

1. Dong Luo, Zainah Ibrahim, Zubaidah Ismail (2011) "Monitoring of curing temperature of early-age cement paste using biconical tapered fiber sensor", Advanced Materials Research, vol. 250-253, pp.3549-3553.
2. Dong Luo, Zainah Ibrahim, Zubaidah Ismail, "The study of early-age curing temperature of cement paste using fiber Bragg grating", 11th International Conference on Concrete Engineering and Technology (2012).